Optimizing Weld Quality in High Stacking Ratio Automotive Joints: Integrated Experimental Design and Machine Learning Benchmarking with Limited Datasets

by

Hasan Habib

A thesis

presented to the University of Waterloo

in fulfillment of the

thesis requirement for the degree of

Master of Applied Science

in

Mechanical and Mechatronics Engineering

Waterloo, Ontario, Canada, 2025

© Hasan Habib 2025

Author's Declaration

This thesis consists of material all of which I authored or co-authored: see Statement of Contributions included in the thesis. This is a true copy of the thesis, including any required final revisions, as accepted by my examiners.

I understand that my thesis may be made electronically available to the public.

Statement of Contribution

This thesis was solely written by the candidate, who also performed all laboratory work, experimental design, process optimization, welding, and mechanical and microstructural characterization, except where otherwise noted. Prof. Elliot Biro provided comprehensive supervision throughout the research process, including guidance on research conception and design, mentorship in experimental planning, critical input during data interpretation, and thorough review and revision of all manuscripts. The thesis comprises six chapters, with Chapter 4 based on a manuscript currently under review and the specific contributions to this work are outlined as follows:

H. Habib, M. Nooranfar, M. Shojaee, R. Bakhtiari, A. Aminzadeh, T. Belgasam, E. Biro. "Reevaluating RSW Acceptance Criteria: Strength Performance in Dissimilar High Stacking Ratio Joints with Inadequate Nugget Penetration" *Welding in the World (under review)*

The conception, experimental design, execution of experiments, data analysis, and writing of manuscript were carried out solely by the candidate. Dr. Mohammad Shojaee assisted in interpreting characterization results, including fractography, interrupted testing, and SEM analysis related to brazing and diffusion phenomena, and assisted in the interpretation of these results. Dr. Tarek Belgasam, as the industrial partner, provided feedback on experimental methodology and offered insights regarding the industrial application of the findings. Prof. Elliot Biro offered supervision encompassing all stages of the project, conceptual and methodological guidance, technical discussion, critical review, editorial input, facilitated access to laboratory resources, and ensured the highest standards of scientific integrity. Melika Nooranfar, Dr. Reza Bakhtiari, Dr. Ahmad Aminzadeh, contributed through collaborative discussions, data curation support, and minor editorial assistance during manuscript preparation.

Abstract

Ensuring crashworthiness in automotive body-in-white (BIW) structures requires reliable resistance spot welds meeting AWS D8.1 guidelines, which mandate minimum 20% nugget penetration into thin sheets. However, this conventional criterion based solely on nugget penetration is inadequate for high stacking ratio (HSR) joints increasingly used with advanced high-strength steels (AHSS). This research quantifies the relationship between nugget penetration and mechanical strength in dissimilar multi-sheet AHSS joints with thickness ratios ≥5:1 and develops machine learning (ML) based parameter optimization models to predict the process parameters for optimal weld joints.

Systematic experimentation investigated three-sheet lap joints with thicknesses ranging from 0.65 to 2.0 mm and tensile strengths varying from 280 to 2100 MPa. A comprehensive design of experiments approach combining Box-Behnken Design (BBD) and Latin Hypercube Sampling (LHS) was implemented to optimize six welding process parameters across 80 conditions. Mechanical testing, including tensile shear strength (TSS) and cross tension strength (CTS), alongside microstructural characterization, revealed that joints without visible nugget penetration into the thin top sheet could achieve high mechanical strengths compared to fully penetrated joints. Interrupted welding experiments confirmed that bonding between sheets with high joint strength and no nugget penetration was due to either diffusion bonding or localized brazing. SEM and EDS analysis distinguished two distinct fusion interfaces: complete fusion zones with full nugget penetration and brazed interfaces, each exhibiting unique diffusion mechanisms.

To extend these experimental insights, six supervised machine learning algorithms were developed and trained to predict nugget dimensions using process parameters and engineered features based on physical process relationships. Gradient boosting provided the highest predictive accuracy with R^2 values of 0.948 for maximum nugget width and 0.903 for nugget penetration, reducing prediction errors to 13% compared to 30% from Minitab statistical tool. Shapley additive explanation (SHAP) analysis identified welding current as the dominant process parameter, while interactions among current, weld time per pulse and electrode force proved critical for joint formation. Model-guided inverse prediction enabled dual-objective parameter optimization with experimental validation confirming predicted outcomes within target tolerances.

The findings demonstrated that conventional acceptance criteria based solely on nugget penetration were inadequate for evaluating joint quality in complex dissimilar multi-sheet RSW assemblies and highlighted the need of quantitatively assessing interfacial bonding mechanisms. The validated machine learning framework provided accurate, interpretable parameter optimization, and offered a scalable pathway for broader industrial applications.

Acknowledgements

First and foremost, I am profoundly grateful to my supervisor, Prof. Elliot Biro for unwavering support and trust, insightful guidance, and constructive feedback he has given me throughout the last two years of my master's study.

I gratefully acknowledge the financial and technical support provided by Honda Research and Development USA, which made this research possible, especially thankful to Dr. Tarek Belgasam for his role as our industrial partner and for sharing practical perspectives that helped contextualize my findings.

I am also grateful to my colleagues and friends in the CAMJ research group especially Dr. Dileep Ramchandran, Dr. Olakunle Betiku, Syed, Faique Al Hussain, Sydney Okoroafor, Jiung Kim, Dr. Reza Bakhtiari, Dr. Ali Afzal, Taha Waqar, Aditya Yalapati, Neel Agarwal, Dr. Ahmad Amainzadeh, Dr. Shima Akbarian, Melika Nooranfar for their companionship, helpful discussions, and encouragement throughout this journey. I am grateful to Dr. Mohammad Shojaee for his collaboration, especially in experimental work, data analysis, and insightful conversations that strengthened this thesis.

Finally, I would like to thank all those whose contributions, directly or indirectly, have aided me in the successful completion of this research.

Dedication

To my beloved parents and amazingly intelligent and caring sisters for sharing my dreams, standing by me through every challenge and keeping faith in me, your unwavering support lifted me beyond my highest hopes.

Table of Contents

Author's Declaration ii

Statement of Contribution iii

Abstract iv

Acknowledgements vi

Dedication vii

List of Figures xii

List of Tables xvii

List of Abbreviations xviii

1. Introduction 1

1.1 Background 1

1.2 Objectives 1

1.3 Thesis Outline 2

2. Literature Review 4

2.1 Overview 4

2.2 Advanced High Strength Steels (AHSS) 4

2.2.1 Generational Advancements in AHSS 6

2.2.2 Interstitial Free (IF) Steel 8

2.2.3 Dual Phase (DP) Steel 9

2.2.4 Hot Stamped Steel 10

2.3 Surface Coating of AHSS 13

2.3.1 Zinc (Zn)-Based Coatings 13

2.3.1.1 Hot-Dip 13

2.3.1.2 Galvannealed (HDGA or GA) coating 13

2.3.1.3 Electrogalvanized (EG) coating 14
2.3.2 Aluminum-Silicon (Al-Si) Coating 14
2.4 Resistance Spot Welding (RSW) 15
2.4.1 Current Range and Weldability Lobe 16
2.4.2 Principle and Process Parameters of RSW 17
2.4.3 Dynamic Resistance (DR) 18
2.4.4 Welding Schedules in RSW 21
2.4.5 Characterization Techniques of RSW Weldability 22
2.5 RSW of Complex Joint 28
2.5.1 Challenges in Dissimilar Welding 28
2.5.2 High Stacking Ratio (HSR) Joints and its Challenges 29
2.6 Modeling of Resistance Spot Welding 35
2.6.1 Physics Based RSW Modeling 36
2.6.2 Data-Driven Modelling in RSW 38
2.7 Summary and Research Gaps 46
3. Methodology 47
3.1 Materials 47
3.2 Resistance Spot Welding (RSW) 48
3.3 Design of Experiments (DOE) 50
3.4 Characterisation 51
3.5 Data Driven Supervised Machine Learning Methodology 53
3.5.1 Data Acquisition and Feature Engineering 53
3.5.2 Data Preprocessing 53
3.5.3 Model Selection and Implementation 53
3.5.4 Validation, Hyperparameter Tuning, and Performance Metrics 54

3.5.5 Inverse Prediction and Experimental Validation 54
3.5.6 Computational Implementation and Reproducibility 55
4. Re-evaluating RSW Acceptance Criteria: Strength Performance in Dissimilar High Stacking Ratio Joints with Inadequate Nugget Penetration 56
4.1 Overview 56
4.2 Effect of RSW process parameters on nugget growth 56
4.3 As-welded microstructures 60
4.4 Interrupted Welds 64
4.5 Mechanical Strength Analysis 67
4.6 Failure Behaviour 69
4.7 Summary 72
5. Experimental Validation of Minitab and Machine Learning Models Inverse Predictions for RSW Weld Quality 73
5.1 Normality and Outlier Assessment of Weld Nugget Measurements 73
5.2 Feature Correlation Analysis for Resistance Spot Welding Parameters 75
5.3 Comparative Performance Evaluation of Regression Models for Nugget Width Prediction 77
5.4 Comparative Performance Evaluation of Regression Models for Nugget Penetration Prediction 79
5.5 Model Prediction Accuracy and Residual Analysis for Maximum Nugget Width 80
5.6 Model Prediction Accuracy and Residual Analysis for Nugget Penetration 82
5.7 SHAP Feature Importance in Nugget Width and Penetration Prediction 84
5.8 Inverse Modeling Accuracy and Experimental Validation 87
5.9 Summary 89
6. Conclusion and Future Recommendations 91
6.1 Conclusion 91

6.2 Future Recommendations 93

References 95

List of Figures

Figure 2.1. (a) Global greenhouse gases (GHG) emissions breakdown in 2024, with transportation contributing 37% from passenger vehicles [20], and (b) CO_2 emission targets for light-duty vehicles across regions, showing the U.S. requires the steepest reduction (4.7% annually) to meet its 2025 goal [21] 5
Figure 2.2. Strength–ductility map of conventional HSS and various generations of AHSS, showing the progression from 1st to 3rd generation steels and their respective mechanical property ranges for automotive applications [29] 7
Figure 2.3. a) Low-magnification optical image of IF steel highlighting equiaxed ferrite grains. (b) High-magnification optical image of IF steel showing titanium carbonitride precipitates along grain boundaries and within grains, which scavenge carbon (C) and Nitrogen (N) from he structure to prevent them from acting as interstitial alloying agents in iron (FE) lattice, thereby suppressing interstitial effects such as yield point elongation and strain aging [40]..... 8
Figure 2.4. (a) Thermal cycle showing intercritical annealing between Ac_1 and Ac_3, followed by quenching to form a ferrite–martensite microstructure [46], (b) Schematic illustrating soft ferrite (light) and hard martensite (dark) phases [47] (c) Optical micrograph of actual DP steel showing a ferritic matrix with dispersed martensitic islands (etched to reveal contrast) [46]..... 9
Figure 2.5. Increase in hot-stamped steel usage in Volvo XC90 body-in-white, from 7% in the 2003 model to 38% in the 2014 model, highlighting the growing reliance on ultra-high-strength steels for improved safety and weight reduction [51].....11
Figure 2.6. (a) Scanning electron microscopic (SEM) image showing a fully martensitic structure (indicated by "M") obtained through conventional direct hot forming. (b) Schematic representation of a ferrite–martensite dual-phase microstructure, characteristic of tailor-tempered steel [47] 11
Figure 2.7. Process flow of (a) direct hot stamping with austenization before forming and quenching, and (b) indirect hot stamping with cold pre-forming before heating for greater shape complexity [53]..... 12
Figure 2.8. SEM micrographs of an Al-Si coated steel showing intermetallic layer formation. The coating consists of Al, Al_5Fe_2Si, and $Al_2Fe_3Si_3$ phases atop a ferrite–pearlite substrate [61]..... 15
Figure 2.9. Schematic of the resistance spot welding (RSW) process showing five stages [67] . 16
Figure 2.10. (a) Relationship between weld current and nugget diameter, showing the transition from undersized to acceptable nuggets and expulsion at high currents, and (b) Weld lobe diagram

indicating the acceptable process window defined by current and weld time to ensure proper nugget formation without expulsion [47] 17
Figure 2.11. (a) Schematic of RSW, including contact and bulk resistances across the welding joint [75], and (b) Typical welding schedule showing RSW process stages [76] 18
Figure 2.12. Resistance evolution during spot welding showing key stages: surface breakdown, softening, melting, nugget growth, and expulsion [80, 81] 20
Figure 2.13. Comparison of welding schedules for (a) single-pulse and (b) double-pulse (PWHT) resistance spot welding, showing current, force, and timing parameters [2] 22
Figure 2.14. Cross-sectional image of a resistance spot weld showing the fusion zone (FZ), heat-affected zone (HAZ), base metal (BM), void formation, electrode indentation depth, solidification direction, and notch at the nugget–base metal interface [28] 23
Figure 2.15. (a) schematic of the temperature profile with iron-carbon diagram to showcase phase transformations [89] , and (b) optical and SEM images showing corresponding microstructures of fusion zone (FZ), coarse-grained HAZ (CGHAZ), fine-grained HAZ (FGHAZ), intercritical HAZ (ICHAZ), and subcritical HAZ (SCHAZ) [75] 24
Figure 2.16. Standard specimen geometries for mechanical testing of RSW joints: (a) tensile-shear (TS) test and (b) cross-tension (CT) test, both with centrally located weld nuggets [68] 25
Figure 2.17. Typical load displacement curve during mechanical test [28] 26
Figure 2.18. Fracture modes in RSW joints (a) Full Interfacial Fracture (Mode 7), (b) Partial Interfacial Fracture (Mode 5), and (c) Pullout Fracture (Mode 1) showing differences in crack path and weld integrity [70, 95, 96] 27
Figure 2.19. Cross-section of RSW joint showing (a) and (b) no nugget growth into thin-thick interface sheet in HSR joints [75] 29
Figure 2.20. Schematic of resistance spot welding in a dissimilar high stacking ratio joint, illustrating current flow, force application, and nugget formation. 30
Figure 2.21. Multistage welding sequence for joining HSR [74] 31
Figure 2.22. (a) 3T RSW configuration with upper and lower electrodes dimensions [86], and (b) showing three different shaped electrodes [87] 32
Figure 2.23. (a, b) Schematic diagrams of tensile-shear loading and force components on a 3T spot weld; (c) cross-tension loading configuration; (d) fracture features in a 3T dissimilar RSW joint showing crack paths and fusion zone [89] 33

Figure 2.24. (a) Schematic and (b) cross-section of weld-bonded Mg alloy/ASS three-sheet joint showing nugget formation, adhesive layer, and porosity at the interface [17] 34
Figure 2.25. Effect of DP600 bottom sheet thickness on (a) nugget size and (b) penetration in 0.6-mm/1.8-mm SAE1004 and DP600 3-sheet RSW joints [118]..... 35
Figure 2.26. Cross-sectional micrograph and corresponding finite element temperature profile of a three-sheet dissimilar steel RSW joint (JAC 270/JSC 980/JSC 590), illustrating nugget formation and peak temperature distribution [71] 37
Figure 2.27. Showing (a) ANN model architecture, and (b) ANFIS model architecture [104].... 40
Figure 2.28. (a) Deep neural network architecture for nugget diameter prediction using 15 input features [107]; (b) images of RSW electrodes used in experiments [44] 41
Figure 2.29. Basic ML pipeline [110] 44
Figure 3.1. Engineering stress-strain curves of the three base materials investigated in this study along the rolling direction (RD). SEM images showing (a) low carbon steel exhibiting ferritic microstructure (b) Fine martensite laths suggesting high strength steel, and (c) dense structure characteristics of ferrite and martensite. 48
Figure 3.2. Schematics of (a) HSR 3-sheet RSW joint showing nugget penetration and geometric parameters across thin–thick and thick–thick interfaces, and (b) multi-pulse RSW schedule used in this study. 50
Figure 3.3. Schematic representation of mechanical test configurations for evaluating weld strength in three-sheet stack-ups: (a) TSS with load applied in shear direction, and (b) CTS designed to apply normal direction. 52
Figure 3.4. ML model benchmarking process flowchart 55
Figure 4.1. Cross-sections of weld nuggets under varying RSW conditions. Each condition involved changes in current, force, weld time, hold time, pulses, and cooling time. Nugget growth progressively increased from (a) to (d) with higher thermal input, with optimal morphology observed in (c). White dashed lines indicate fusion zone boundaries 61
Figure 4.2. a) Optical macrograph of the welded cross-section of weld condition NP with nugget growth into top thin sheet - showing FZ, HAZ, and BM. Optical macrograph and corresponding microstructural analysis of the weld nugget region. (b–e) SEM micrographs at 1000× magnification highlighting the microstructural evolution in the HAZ of the top, middle, and bottom sheets, respectively 62

Figure 4.3. Microhardness profile measured from the top sheet through the middle and bottom sheets along the weld cross-section. The inset shows the approximate hardness measurement path across the nugget and HAZ for each sheet..... 63
Figure 4.4. Cross-sections of interrupted welds comparing weld nugget formation using multipulse schedules for NNP (a, c, e, g – without nugget growth into thin sheet) and NP (b, d, f, h – with nugget growth into thin sheet). Corresponding pulses weld schedule are shown to the left of each row. Nugget penetration into the top sheet is observed in NP, demonstrating the effect of pulse configuration on weld development in three-sheet stack-ups..... 65
Figure 4.5. Showing maximum nugget width and nugget height as a function of weld time for NNP and NP weld conditions 66
Figure 4.6. Mechanical performance evaluation of four weld conditions (a) TSS load displacement curves, (b) CTT load displacement curves, and (c) bar chart summarizing the peak loads of TSS and CTS. The red dashed line indicates the minimum load threshold..... 67
Figure 4.7. Fracture cross-sections of (a, c) condition NNP without nugget penetration, displaying partial bonding in the top sheet. (b,d) NP exhibiting nugget penetration into the top sheet, showing continuous partial fusion into top thin sheet. Red dashed boxes highlight regions along the faying interface selected for further investigation of potential diffusion bonding, brazing or incomplete fusion. Force directions (F) are indicated with blue arrows for both loading configurations 70
Figure 4.8. EDS line scan and elemental mapping of the joint interface at regions highlighted earlier by red boxes. (a-c) correspond to a region indicating solid state diffusion bonding, characterized by a uniform elemental distribution and absence of discrete intermetallic layers. The smoother profiles in (f) suggest stronger metallurgical continuity across the interface. (d-f) represent a region showing evidence of localized brazing, where a concentrated Al peak and sharp elemental gradients indicate limited interdiffusion and the presence of a thin interfacial or intermetallic layer 71
Figure 5.1. Summary of data quality for maximum nugget width and nugget penetration: (a, b) probability plots confirm near-normality, while (c, d) outlier plots reveal only a few atypical measurements across the dataset..... 74
Figure 5.2. Correlation heatmap illustrating the relationships among process parameters and engineered features. Strong positive and negative correlations highlight key interactions and potential redundancies within the welding parameter set..... 76

Figure 5.3. Comparison of Ridge Regression and Gradient Boosting models for maximum nugget width prediction: (a, b) Actual vs. predicted plots; (c, d) corresponding residual distributions... 81
Figure 5.4. Comparison of Ridge Regression and Gradient Boosting models for nugget penetration prediction: (a, b) Actual vs. predicted plots; (c, d) corresponding residual distributions. 83
Figure 5.5. SHAP summary plots are shown for both Ridge Regression (a, c) and Gradient Boosting (b, d), highlighting differences in feature importance and model interpretability for maximum nugget width and nugget penetration respectively 85
Figure 5.6. Comparison of nugget cross-sections predicted by Gradient Boosting model (a, c, e) and Minitab statistical analysis (b, d, f) 88

List of Tables

Table 3.1. Chemical composition (wt.%) and carbon equivalent (Ceq) of the investigated materials. 47
Table 3.2. Mechanical properties, including 0.2% offset yield strength (YS), ultimate tensile strength (UTS), (measured using the 0.2% offset method), total elongation (TE), and uniform elongation (UE) of investigated materials. 47
Table 3.3. Range of input process parameters investigated 3T HSR RSW schedules investigated. 51
Table 3.4. Weld schedule used for mechanical and interrupted testing 52
Table 3.5. Optimized hyperparameters of all ML models 54
Table 4.1. Summary of ANOVA results for the influence of process parameters on diametric growth in RSW joints. The model includes linear, quadratic (square), and two-way interaction terms..... 57
Table 5.1. Performance metrics of various machine learning models for predicting maximum nugget width, showing R^2, RMSE, MAE, MAPE, and MBD for each method 78
Table 5.2. Performance metrics of various machine learning models for nugget penetration, showing R^2, RMSE, MAE, MAPE, and MBD for each method 80
Table 5.3. Comparison of machine learning and Minitab inverse prediction results for maximum nugget width and nugget penetration, including measured values with 95% confidence intervals and corresponding percentage errors 89

List of Abbreviations

AHSS	Advanced High-Strength Steels
AI	Artificial Intelligence
ANN	Artificial Neural Network
ANOVA	Analysis of Variance
AWS	American Welding Society
BH	Bake Hardening (Steel)
BIW	Body-in-White
BM	Base Metal
CGHAZ	Coarse-Grained Heat-Affected Zone
CNN	Convolutional Neural Network
CTS	Cross-Tension Strength
DNN	Deep Neural Network
DOE	Design of Experiments
DP	Dual Phase (Steel)
DR	Dynamic Resistance
FEM	Finite Element Modeling
FGHAZ	Fine-Grained Heat-Affected Zone
FZ	Fusion Zone
GA	Galvannealed
GI	Galvanized (Hot-Dip Galvanized)
HAZ	Heat-Affected Zone
HSLA	High Strength Low Alloy
HSR	High Stacking Ratio
ICHAZ	Intercritical Heat-Affected Zone
IMC	Intermetallic Compound

MAE	Mean Absolute Error
MAPE	Mean Absolute Percentage Error
MBD	Mean Bias Deviation
ML	Machine Learning
MPWS	Multi-Pulse Welding Schedule
PF	Pullout Fracture
PO	Pullout Fracture
RF	Random Forest
RMSE	Root Mean Square Error
RSM	Response Surface Methodology
RSW	Resistance Spot Welding
SVR	Support Vector Regression
TSS	Tensile-Shear Strength
UHSS	Ultra High-Strength Steel

1. Introduction

1.1 Background

The drive to produce lighter and more fuel-efficient vehicles has led auto manufacturers to use advanced high-strength steels (AHSS) in the body in white (BIW) of modern automobiles [1, 2]. These customised steels help reduce vehicle weight without sacrificing strength and safety, supporting both environmental goals and crash protection [3]. As a result, AHSS has become a key material in automotive design. Resistance spot welding (RSW) [4, 5] is the primary joining method for these advanced steels in vehicle BIW due to process robustness and automation, but it faces difficulties when used for complex dissimilar joints especially when a thin low carbon sheet is attached with multiple thick sheets of AHSS with thickness ratio of 5:1 or more in three sheet joint (3T) and four sheet joint (4T) configurations, this type of joint is also known high stacking ratio (HSR) joints, which are increasingly common in latest automotives [6–8]. One of the most important issues associated with these joints is the limited penetration of the weld nugget into the thin sheet. According to AWS D8.1 [9] guidelines, a minimum of 20% nugget penetration into the thin sheet is required to ensure acceptable weld quality and joint reliability in configurations where a thin sheet is attached to thicker sheets. Despite the importance of this issue, few studies [7, 10–12] have provided a detailed roadmap for improving the nugget growth using different systematic technique including electrode design modification or process changes like multi step welding schedules. However, the role of fixed magnitude multipulse welding schedule on nugget growth in HSR joints remains unexplored, as does the combined influence of all process parameters when carefully optimized through design of experiments (DOE). At the same time, although machine learning (ML) [13–17] offers promising possibilities for predicting weld quality, most models depend on large datasets that are rarely available for experimental HSR welds. Therefore, it is important to analyze whether current supervised learning models can maintain accuracy and avoid bias when trained on the limited, real-world datasets typical in this field.

1.2 Objectives

This thesis aims to better understand the role of process parameters on weld nugget growth in HSR joints, examine the effects of brazing and diffusion on welded joint strength when visible nugget penetration does not occur int thin sheet, and develop ML modeling techniques that can predict

optimal process parameters from small experimental dataset, with experimental validation of these predictions. The specific objectives of this work are:

1. Analyze weld nugget morphology and penetration in HSR joints using a carefully designed DOE.
2. Investigate how brazing and diffusion contribute to joint strength when nugget penetration is limited in HSR joints.
3. Develop a modeling technique to predict the welding response of HSR welds accounting for typical RSW parameters.
4. Establish an inverse modeling approach that propose optimal welding conditions for desired nugget size and validate its accuracy against traditional Minitab statistical method and experimental results.

1.3 Thesis Outline

The thesis has been organized into six chapters as follows:

Chapter 1: Introduction - Introduces the background, objectives, and organizations of this thesis.

Chapter 2: Literature Review - Provides an overview of necessary background found in past research on advanced high-strength steels (AHSS), resistance spot welding (RSW), high stacking ratio (HSR) joints, supervisor machine learning (ML) models for RSW weld quality prediction and highlights the specific research gaps that this thesis aims to address.

Chapter 3: Methodology - Explains how the research was planned and conducted. This includes: a description of the materials, welding procedure, statistical methods, and details on how machine learning models were built and validated.

Chapter 4: Reevaluating RSW Acceptance Criteria: Strength Performance in Dissimilar High Stacking Ratio Joints with Inadequate Nugget Penetration – Examines the mechanical performance and failure characteristics of dissimilar HSR joints when nugget does not fully penetrate, investigating the contribution of brazing and diffusion mechanisms to joint strength and proposing revised weld acceptance criteria.

Chapter 5: Experimental Validation of Minitab and Machine Learning Models Inverse Predictions for RSW Weld Quality - Models the welding response of RSW testing using ML techniques,

determines the optimal modeling approach through comparative statistical analysis with traditional Minitab methods, and validates the selected model against experimental results to demonstrate predictive accuracy for weld quality assessment.

Chapter 6: Conclusion and Future Recommendations - Summarizes key research findings/contributions, discusses implications for RSW acceptance criteria, and identifies future research gaps to enhance understanding of HSR dissimilar joint welding and ML applications in materials joining operations.

2. Literature Review

2.1 Overview

The demand from regulators to increase fuel economy and reduce CO_2 emissions, along with better crashworthiness, have driven the automotive industry to pursue lightweight vehicle designs without compromising safety performance. These goals have made advanced high-strength steels (AHSS) central to vehicle body-in-white (BIW) structures. The mechanical advantages of AHSS are clear due to their superior strength-to-weight ratio, enhanced formability and improved energy absorption characteristics compared to conventional steels. However, AHSS present challenges in welding due to their complex microstructure, coating, and thermal characteristics. Resistance spot welding (RSW) is a robust joining method used in automotive construction. The RSW process is controlled by dynamic resistance (DR) and interface characteristics, especially in dissimilar and high-stacking ratio (HSR) joints, which has a strong influence on weld nugget growth. Understanding these interactions is important for to maximize joint performance and reliability. This chapter summarizes important advances in AHSS grades, coatings, fundamentals of the RSW process, weld failure mechanisms, and data-driven methods to improve weld quality, which is increasingly used in the construction of advanced automotive assemblies.

2.2 Advanced High Strength Steels (AHSS)

The automotive sector is increasingly required to reduce carbon emissions and environmental impact of the vehicles they produce amid escalating global climate concern. In 2024, nearly one-third of global greenhouse gas emissions came from transportation, with passenger automobiles and light-duty trucks contributing the most to these emissions as shown in the Figure 2.1(a) [18]. As global CO_2 emissions neared 37 billion tons, the U.S. Environmental Protection Agency (EPA) [19] increased its regulations by issuing a ruling that established an average CO_2 emission limit on light-duty vehicles at 149 g/mile for 2025 and a subsequent reduction of in coming year as shown in Figure 2.1(b) [19]. These evolving regulations compel automotive manufacturers to innovate customized and optimized materials that meet rigorous environmental targets, vehicle safety requirements, and reduced overall vehicle weight in BIW construction.

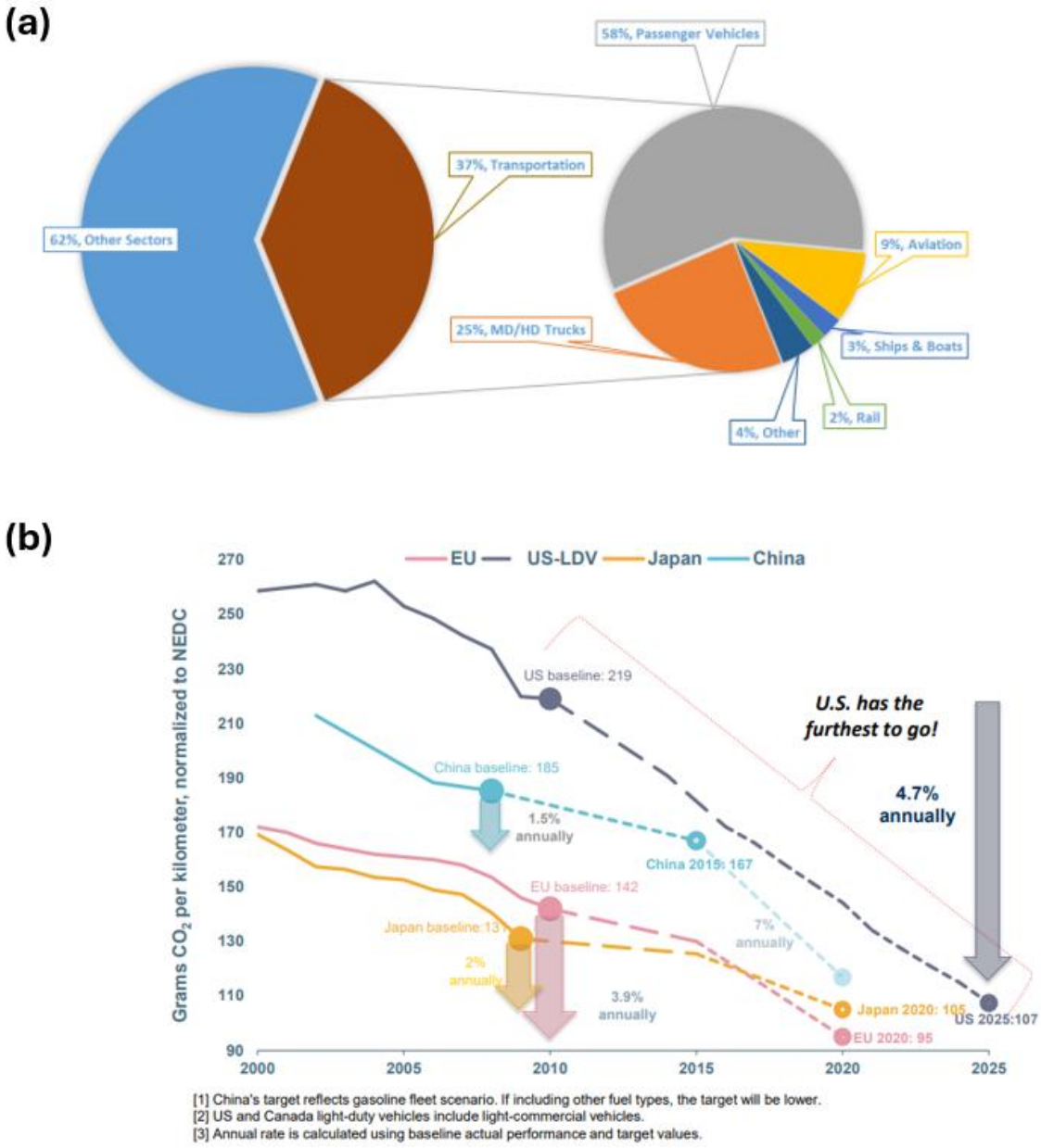


Figure 2.1. (a) Global greenhouse gases (GHG) emissions breakdown in 2024, with transportation contributing 37% from passenger vehicles [20]*, and (b) CO_2 emission targets for light-duty vehicles across regions, showing the U.S. requires the steepest reduction (4.7% annually) to meet its 2025 goal* [21]

Traditionally, conventional high-strength steels including Interstitial Free (IF), Bake Hardening (BH), and High Strength Low Alloy (HSLA) have met BIW structural requirements however, their deficiencies in formability and crash performance have proven insufficient for growing demands

of lightweight, high-safety vehicle design [22]. In response, AHSS offers a versatile class of materials with tunable mechanical properties tailored for specific application. AHSS are generally classified into three generations as shown in the Figure 2.2 and each generation offers distinct combinations of strength, ductility, and formability, enabling advantages such as reduced vehicle weight, enhanced crash energy absorption, improved fuel efficiency, and broad applicability across automotive components [23]. Approximately, newly developing vehicles are based on 50% AHSS, with some joints offered reduction is weight up to 40% and overall vehicle weight reduction of up to 10% compared to conventional steels [21, 24].

2.2.1 Generational Advancements in AHSS

The first generation of AHSS (1G-AHSS) comprises dual-phase (DP), transformation-induced plasticity (TRIP) and martensitic (MART) steels, each offering balanced strength and ductility through engineered microstructure and thermomechanical processing [25, 26]. DP steels consist of a soft ferritic matrix and discrete martensitic islands, offering superior tensile strength through strain hardening and high work-hardening rates with moderate elongation, while TRIP steels take advantage of retained austenite (RA) which transforms to martensite under strain to improve work hardening, energy absorption, and elongation [27]. MART steels consist predominantly martensite and provide ultra-high strength (up to 2000 MPa) with limited ductility making them useful for reinforcing key BIW structural areas such as the passenger compartment [27, 28]. While 1G-AHSS deliver a high strength-to-ductility ratio and have achieved widespread adoption in automotive manufacturing, their use is constrained by the higher costs associated with complex thermomechanical processing as well as forming challenges arising from springback and work hardening characteristics [3, 28].

To overcome the strength-ductility limitations of first-generation AHSS the second generation (2G-AHSS) introduced steels with fully austenitic microstructure specifically, twinning-induced plasticity (TWIP) steels and austenitic stainless (AS) steels [3]. TWIP steels rely on deformation twinning as the primary mechanism of plasticity, which provides excellent ductility (exceeding 50% elongation) while maintaining high tensile strength. AS steels also provide good ductility and additional superior corrosion resistance [3, 24]. Despite the benefits of 2G-AHSS, their limited applications are primarily due to the expensive alloys, complex forming behavior, and challenges especially in welding, including undesirable phase transformations and residual stresses [28].

Therefore, 2G-AHSS are limited to niche application of a cost benefit for formability and corrosion resistance [3, 28].

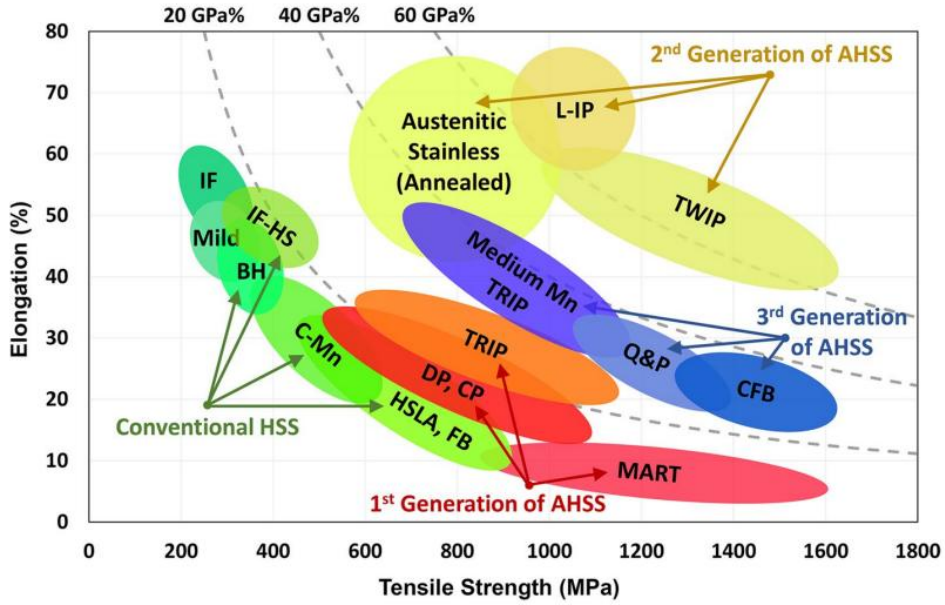


Figure 2.2. Strength–ductility map of conventional HSS and various generations of AHSS, showing the progression from 1st to 3rd generation steels and their respective mechanical property ranges for automotive applications [29]

The third generation of AHSS (3G-AHSS) is largely in development and research phase however some commercial grades have started becoming part of BIW, this generation bridges the gap between first two generations, offering superior strength-ductility properties compared to 1G-AHSS while avoiding the high cost of 2G-AHSS [30, 31]. This generation of AHSS contains four major types: TRIP-assisted bainitic ferrite (TBF), carbide-free bainitic (CFB), quenched-and-partitioned (Q&P), and medium-manganese (Med-Mn) steels [31–33]. These grades consist of multiphase microstructures that consist of ferrite, bainite, martensite, and retained austenite. TBF and CFB steels use the same bainitic ferrite matrix with retained austenite for increased energy absorption capacity. Q&P steels consist of a martensitic matrix with retained austenite and can lead to tensile strengths above 1000 MPa and elongations up to 20% [32–34]. Med-Mn steels (3-12 wt% Mn) exploit austenite formation through intercritical annealing to achieve similar strength-ductility combinations [35]. The adoption of 3G-AHSS can further reduce the vehicle weight by integrating thinner gauge in crucial structural parts of vehicle BIW to improve the crashworthiness of passenger compartment. Since this study utilized conventional steel (ultra low carbon IF), and

1G-AHSS (hot stamped coated steel and DP steel), thus the following section presents comprehensive description of these materials, highlighting their microstructural features, mechanical properties, and significance in the vehicle BIW.

2.2.2 Interstitial Free (IF) Steel

Interstitial-Free (IF) steel is an ultra-low carbon steel typically contain 20-50 ppm of carbon and 10-50 ppm of nitrogen, manufactured using vacuum degassing to removes dissolved gases, i.e., carbon monoxide (CO), hydrogen (H), and nitrogen (N), from liquid steel [9]. Microalloying elements, such as titanium (Ti) and niobium (Ni) are added which react with C and N to create stable carbides and nitrides, resulting in a uniform ferritic microstructure with precipitates at grain boundaries and within grains as shown in Figure 2.3(b) [36, 37]. This microstructure illustrated in Figure 2.3(a) imparts high ductility with low yield point elongation, and an excellent surface quality, qualities ideal for deep-drawing operations [3]. Although IF steels are lower in strength compared to other automotive steel grades, they offer exceptionally high elongation and superior formability which facilitate the forming of complex BIW components such as hoods, pillar skins, and floor pans that demand superior formability and surface finish [38, 39]. Consequently, IF steels are widely regarded as optimal materials for deep-drawn automotive parts, provided that stringent formability requirements can be satisfied [36].

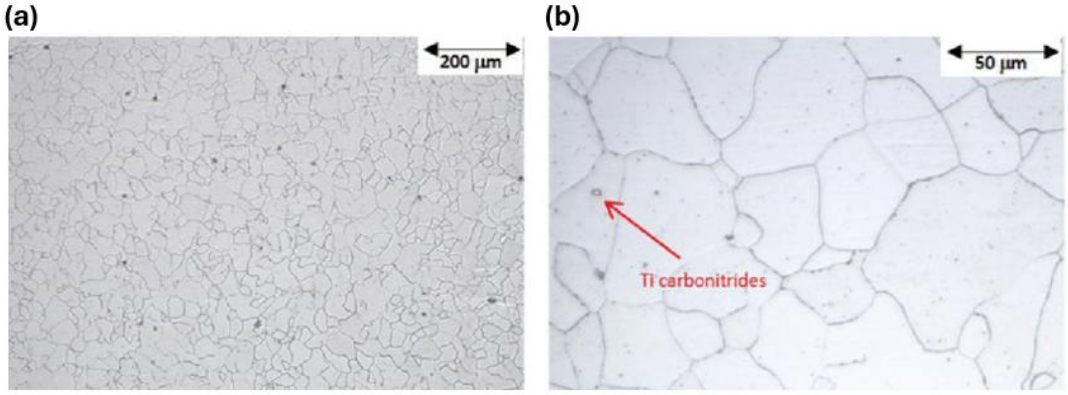


Figure 2.3. a) Low-magnification optical image of IF steel highlighting equiaxed ferrite grains. (b) High-magnification optical image of IF steel showing titanium carbonitride precipitates along grain boundaries and within grains, which scavenge carbon (C) and Nitrogen (N) from he structure to prevent them from acting as interstitial alloying agents in iron (FE) lattice, thereby suppressing interstitial effects such as yield point elongation and strain aging [40]

2.2.3 Dual Phase (DP) Steel

DP steels are produced through hot-rolling or cold-rolling followed by intercritical annealing where the steel is heated into two-phase region ($\alpha + \gamma$) between Ac_1 and Ac_3 and held for a short time to allow small region of austenite to form into the ferrite matrix, which when rapidly quenched, transforms to martensite resulting in microstructure consisting of soft ferrite formed during annealing and martensite transformed from austenite during quenching as shown in Figure 2.4(a) [23, 41, 42]. Controlled heating, holding, and cooling rate are important process parameters to get desired fraction and distribution of martensite. The hard martensite islands as shown in Figure 2.4(b-c) in a ductile ferrite matrix provide a low yield to tensile strength ratio, high levels of uniform elongation, and a high initial work-hardening rate, properties ideal for automotive forming operations [43]. Depending on the alloy composition and processing conditions, small amounts of bainite or RA may also present. Alloying elements i.e., manganese, chromium, molybdenum improves strength and hardenability [43, 44, 45]. Owing to these characteristics, DP steels are well-suited for BIW components that require both formability and strength, including reinforcements, beams, and crash-relevant structures [3].

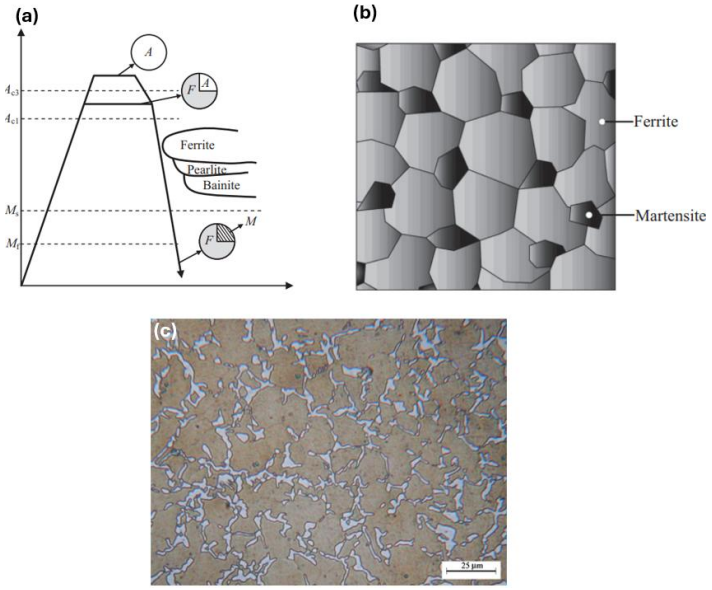


Figure 2.4. (a) Thermal cycle showing intercritical annealing between Ac_1 and Ac_3, followed by quenching to form a ferrite–martensite microstructure [46]*, (b) Schematic illustrating soft ferrite (light) and hard martensite (dark) phases* [47] *(c) Optical micrograph of actual DP steel showing a ferritic matrix with dispersed martensitic islands (etched to reveal contrast)* [46]

2.2.4 Hot Stamped Steel

Press hardening or hot-stamping steel was first developed in Sweden at Plannja Hard Tech (later became SSAB Hardtech, then Gestamp HardTech) remained proprietary until the key patents expired in the late-1990s [48, 49]. Following the expiration of these patents, hot-formed steels have become standard for BIW structures for side impact beams, A/B pillar, roof rails, and bumper reinforcements, with global production rising rapidly to over 100 million parts by 2007 [50]. An example of a comparison between model 2003 and 2014 of Volvo XC90 is shown in Figure 2.5 where the proportion of hot stamped steel increased from 7% to 38% respectively.

The hot stamping process involves heating boron steel blanks to an austenization temperature (880-950°C) to convert initial ferritic-pearlitic microstructure into austenite to improve formability at high temperatures. The heated austenitic blank is transferred to water-cooled forming dies where forming and quenching occurs simultaneously, transforming austenite into fully martensitic microstructure as shown in Figure 2.6(a-b). This process enables the manufacturing of ultra-high strength parts (usually exceeding tensile strength of 1500-2000 MPa) with complex geometries that cannot be achieved by cold stamping of high-strength steels, with no springback in these parts due to stress relief at elevated temperatures. Recent developments include multi-phase and tailor-tempered variants which provide locally adjusted ductility for better crashworthiness [50, 51]. Industrial production of such steel is typically achieved through two method, direct and indirect hot forming.

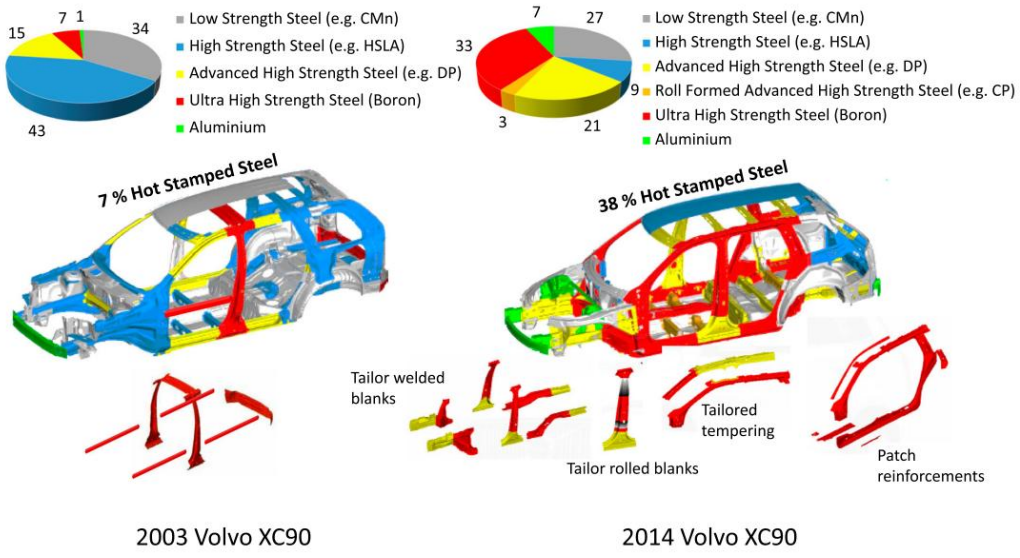


Figure 2.5. Increase in hot-stamped steel usage in Volvo XC90 body-in-white, from 7% in the 2003 model to 38% in the 2014 model, highlighting the growing reliance on ultra-high-strength steels for improved safety and weight reduction [51]

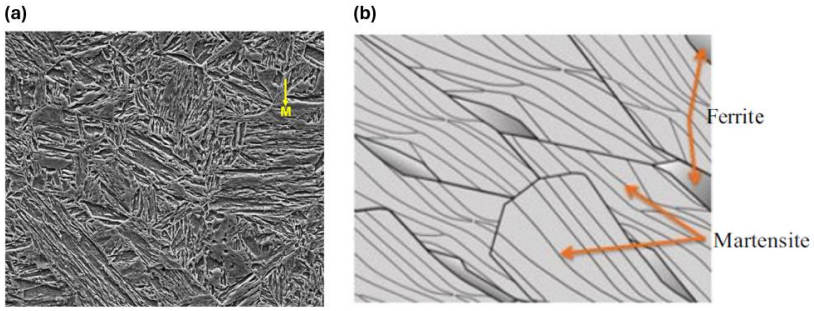


Figure 2.6. (a) Scanning electron microscopic (SEM) image showing a fully martensitic structure (indicated by "M") obtained through conventional direct hot forming. (b) Schematic representation of a ferrite–martensite dual-phase microstructure, characteristic of tailor-tempered steel [47]

2.2.4.1 Direct Hot-forming

Direct hot-forming (or direct press-hardening) begins with cutting steel blanks to shape and heated them in a furnace as shown in Figure 2.7(a), at temperatures between 880-950 °C for several minutes to obtain a fully austenitic microstructure that is suitable for high ductility and formability. After austenization, steel blanks are quickly transferred to water-cooled dies where they simultaneous formed and quenched under high pressure [51, 52]. This rapid cooling to

temperatures between 150-200 °C causes the austenite to transform to hard martensite, imparting final part with high strength and dimensional accuracy. The total time from forming to quenching is usually occurs within minutes, making this method suitable for bulk production of high-performance automotive structural parts [50].

2.2.4.2 Indirect Hot-Forming

The indirect hot-forming process, also known as the two-stage or pre-form plus quench method, begins with cold forming the steel sheet into a near-final shape at room temperature, enabling the production of larger and more complex parts compared to the direct hot forming method because the cold pre-forming step allows for better material flow control, reduces the risk of component distortion, and extends forming limits [50]. After forming, the part is then heated in furnace to austenitizing temperatures (generally 880-950°C), transforming the microstructure to austenite and providing the ductility needed for final shaping. The preheated part is quickly loaded into a water-cooled die and undergoes final forming while simultaneously quenching to create a martensitic dominated microstructure for high strength [50]. A major benefit of this process is its compatibility with traditional zinc-based coating materials. However indirect method is complicated because of additional costs due to the need of separate tooling and the forming process [53]. The process schematic is shown in Figure 2.7(b), overall indirect hot forming is well suited for the manufacturing BIW components with complex geometries and better corrosion resistance, balancing the trade-off between manufacturability, coating, and part performance [49, 50].

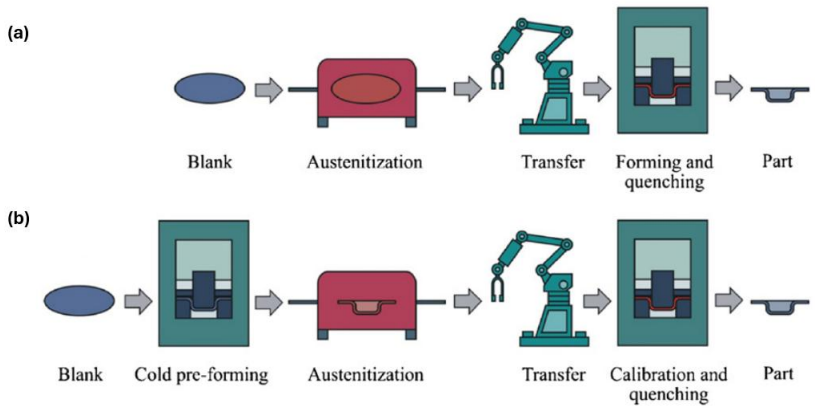


Figure 2.7. Process flow of (a) direct hot stamping with austenization before forming and quenching, and (b) indirect hot stamping with cold pre-forming before heating for greater shape complexity [53]

2.3 Surface Coating of AHSS

To alleviate corrosion susceptibility [54] of advanced high-strength steels (AHSS) during forming and service, protective coatings are used extensively. The predominant protective coatings in the automotive industry are based on zinc (Zn) and aluminum (Al) based [53, 55]. These coatings provide better service life, lower maintenance, and assistance in joining and of parts.

2.3.1 Zinc (Zn)-Based Coatings

Zn offers two means of protection for steel: first, as a physical barrier to air and moisture, and second through cathodic protection, since Zn is more electrochemically active than iron (Fe), it corrodes preferentially to protect exposed steel at cut edges or scratches. Zn-coated AHSS offer improved lubrication during press-forming and long-term corrosion protection without the need for waxes or environmentally harmful post-treatment [54, 56]. The following section discusses common zinc-based coating techniques.

2.3.1.1 Hot-Dip Galvanized (HDGI or GI) coating

In this process, steel sheets or coils are submerged in a bath of molten Zn, at approximately 450 °C. To optimize adhesion and coating quality, the steel is preheated to near the temperature of the Zn bath. A small addition of aluminum (0.005–0.020 wt.%) is generally included in the Zn bath to improve surface brightness, reduce the formation of Zn dross, and facilitate the formation of a thin Fe_2Al_5 intermetallic layer at the steel coating interface. The coated steel is removed from the Zn bath and excess Zn is removed using air knives to produce the desired coating thickness. The final coating consists of a pure Zn outer layer, offering excellent sacrificial protection and cost-effective general corrosion resistance [54, 57].

2.3.1.2 Galvannealed (HDGA or GA) coating

After the application of Zn coating, the galvanized steel may undergo an additional annealing step at 450–600 °C, promoting iron to diffuse into the Zn coating and form Zn–Fe alloy with 8–12% iron on average [57]. GA coatings offer better weldability, higher electrical resistance, and better surface hardness, although the additional annealing process is an added cost to traditional galvanized coatings [54, 57].

2.3.1.3 Electrogalvanized (EG) coating

EG coatings are applied by passing steel through an electrolytic bath filled where Zn ions are deposited on the surface of the steel by electrical current at room temperature. This process allows yields uniform and thin coating with enhanced surface appearance. One major benefit is that the mechanical and physical properties of the underlying substrate remain largely intact due to low processing temperature [58, 59].

2.3.2 Aluminum-Silicon (Al-Si) Coating

Hot-dipped aluminized coatings are predominantly used in modern automotive applications involving hot stamped steel such boron steel (22MnB5) [57] due to their superior high-temperature oxidation resistance and compatibility with hot-stamping [49]. The coating is generally composed of 87% Al, 10% Silicon (Si), and 3% Fe and is applied by immersing the preheated steel sheet into molten Al at approximately 650–675 °C. Si is important to prevent the formation of brittle intermetallic phases of Fe-Al, and to promote the formation of silicate-rich layers that yield a robust multilayer microstructure [53]. During hot-stamping process Al–Si coating partially melts and undergoes extensive interdiffusion: Fe from substrate diffuses outward while aluminium diffuses inward, resulting in the sequential formation of intermetallic phases such as Al_8Fe_2Si, Al_5Fe_2, and AlFe as shown in the Figure 2.8 [53]. These intermetallic significantly influence the mechanical integrity and oxidation resistance of the coating during heating and subsequent quenching. Following hot stamping, the surface develops a thin film of aluminium oxide (Al_2O_3) that serves as a barrier to further oxidation and environmental degradation [60]. This makes Al–Si coatings especially suitable for components in critical safety zones, such as B-pillars and door reinforcements, where high strength and long-term thermal stability are paramount [23, 28].

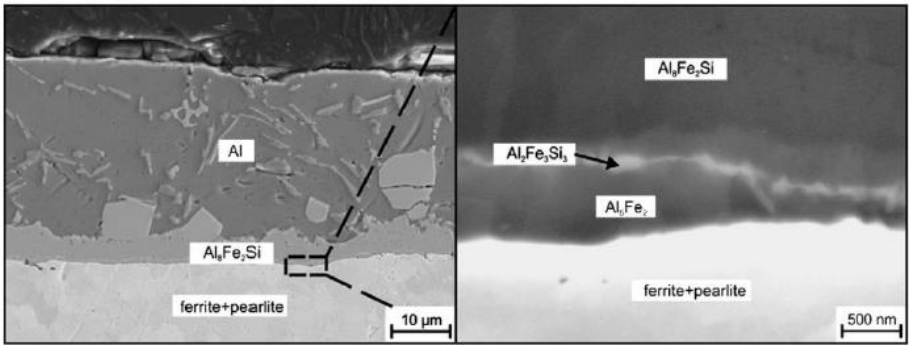


Figure 2.8. SEM micrographs of an Al-Si coated steel showing intermetallic layer formation. The coating consists of Al, Al_5Fe_2Si, and $Al_2Fe_3Si_3$ phases atop a ferrite–pearlite substrate [61]

2.4 Resistance Spot Welding (RSW)

Resistance Spot Welding (RSW) is a highly used joining process in vehicle BIW manufacturing due to its high efficiency, automation ability, relatively low-cost, and mass production capability. An average automobile body has approximately 3,000 to 6,000 spot welds making RSW a vital role in modern vehicle assembly [62, 63]. RSW involves usually 5 coordinated steps as shown in Figure 2.9, of which most are now automated in practice [47, 64].

The RSW process begins with material coupons placed between two water-cooled copper alloy electrodes, usually made from Cu-Cr-Zr alloys [4]. The electrodes perform dual functions: they apply clamping force and conduct welding current [28]. The welding cycle starts with the squeeze time, during which the system delays (50–100 ms) to reach full electrode force before current flows. Next, in weld time (typically 100–500 ms), a high current pass through the sheets and generate intense localized heat at the faying interfaces due to high electrical resistance there. This heat melts contact surfaces, forming a molten weld nugget [23, 28]. Following the weld time the electrodes continue to apply pressure during the hold time (200-600ms) to provide enough time for the solidification of the molten nugget. This phase is essential for preventing crack formation and minimizing voids in the solidified weld nugget. After solidification, the electrodes are retracted. The cooling system of electrodes helps remove heat from the weld, reduces thermal degradation, wear, and preserves electrode tip geometry for repeated weld quality [62, 65]. The typical weld schedule along with post welding is shown in Figure 2.11(b). The interaction of these and other RSW process parameters creates a complex optimization challenge, as the control of

each parameter directly influences weld quality. To address this, modern RSW systems employ sophisticated adaptive timing controls to optimize these phases during the process [66].

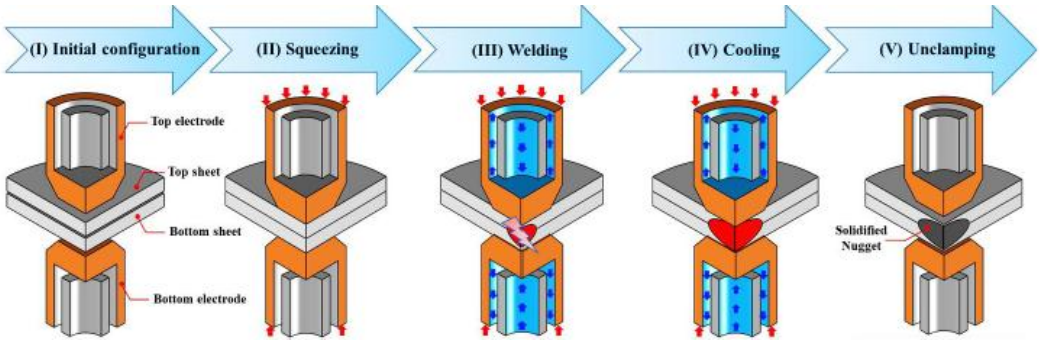


Figure 2.9. Schematic of the resistance spot welding (RSW) process showing five stages [67]

2.4.1 Current Range and Weldability Lobe

The diameter of the weld nugget which is related to but distinct from the weld button is an important quality measure in RSW since as it determines joint mechanical strength and long-term performance. Shojaee *et al.* [68] and Zhao *et al.* [69] reported a strong direct correlation between nugget diameter and joint strength properties, consistent with numerous other studies in the literature. The American Welding Society (AWS) D8.1M [70] provides a guideline to achieve acceptable welds in automotive applications by the minimum acceptable nugget diameter of $d_{min} = 4\sqrt{t}$, where t is sheet thickness in mm, but the minimum size can vary depending on design requirements. Whereas the upper limit is usually defined by expulsion due to maximum current. These limits define the range of weldability current and weldability lobe as shown in Figure 2.10(a-b) [47]. The current range curve is developed through experiments, while the lobe curve is produced through multiple current range curves with varying weld times. The current range and lobe curves show ranges of weld current/time that will produce acceptable welds in production, as well as provide a means of quality control through monitoring of these weld parameters. A wide weldability lobe is preferred in manufacturing because it covers a broader processing window and greater tolerance for process parameter variation [71]. Defects like expulsion, when molten metal is pushed out of the faying interfaces are usually caused by high welding current, long weld time, and low electrode force [72, 73] , now a days expulsion can be predicted through the use of online weld quality monitoring [72]. Conversely, insufficient heat input results in either incomplete fusion or neck-sized nuggets both of which compromised weld integrity [74].

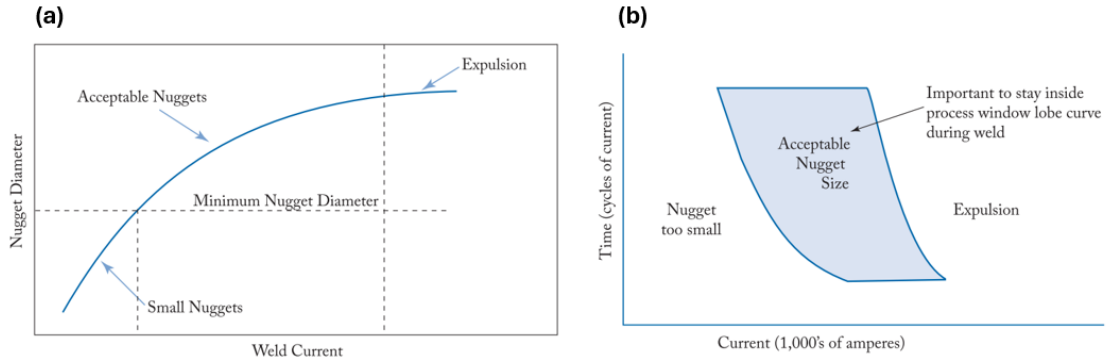


Figure 2.10. (a) Relationship between weld current and nugget diameter, showing the transition from undersized to acceptable nuggets and expulsion at high currents, and (b) Weld lobe diagram indicating the acceptable process window defined by current and weld time to ensure proper nugget formation without expulsion [47]

2.4.2 Principle and Process Parameters of RSW

The principle of RSW process is governed by Joule heating, as shown in Equation 1. As current flows through the electrical resistances through the overlapping contact area of two or more metal sheets, causes localized heat at the faying interfaces. This localized heating generates sufficient thermal energy (Joule heating) to melt the material at the faying interface, creating molten nugget that fuses overlapping metal sheets under electrode pressure, resulting in a strong metallurgical bond upon solidification.

$$Q = \int_0^t R(t) \cdot I^2(t)\, dt \tag{1}$$

Where Q is the total heat generated, $I(t)$ is the time-dependent current, $R(t)$ is the total electrical resistance of joint, and V is the applied voltage across the sheets. When evaluating RSW, total electrical resistance is a major determinant of heat generation and consequently weld quality. Total electrical resistance R_{total} is sum of bulk and contact resistance. For two sheet welding as illustrated in Figure 2.11(a) R_1 and R_7 are the bulk resistances of the top and bottom electrodes, R_2 is contact resistances between top electrode and the top sheet where as R_6 is between bottom electrode and bottom sheet. R_3 and R_5 are considered as bulk resistances of materials and R_4 is the contact resistance between two sheets. Mathematically, R_{total} can be summarized as shown in Equation 2:

$$R_{total} = R_1 + R_2 + R_3 + R_4 + R_5 + R_6 + R_7 \tag{2}$$

R4 is particularly important because it defines where most heat is generated during RSW. High contact resistance leads to greater heat concentration at the joint interface and favors nugget formation, while low contact resistance causes insufficient heating, potentially yielding undersized or weak weld nuggets. Factors such as surface cleanliness, material properties, material thickness and the electrode force all play an important role in the magnitude and distribution of these resistances and directly influence the joint quality [11].

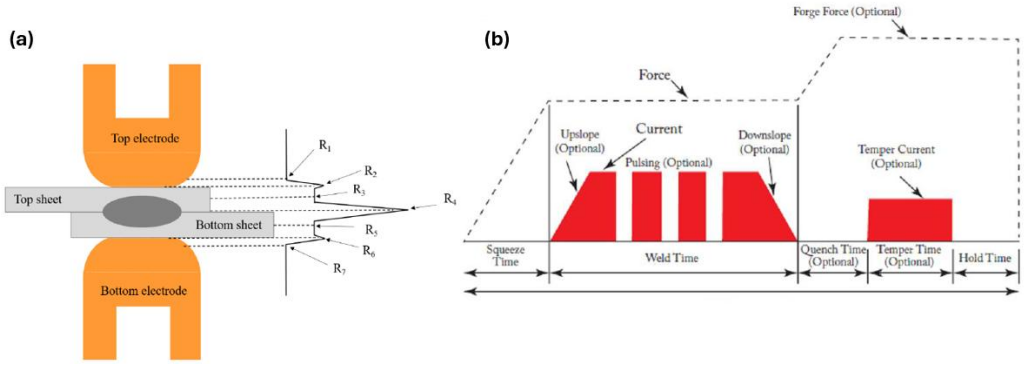


Figure 2.11. (a) Schematic of RSW, including contact and bulk resistances across the welding joint [75]*, and (b) Typical welding schedule showing RSW process stages* [76]

2.4.3 Dynamic Resistance (DR)

The electrical resistance during RSW does not remain constant but varies throughout the weld process. This variable behavior is referred to as dynamic resistance (DR), and is caused by metallurgical, thermal, and geometric modifications which occur due to temperature, current and pressure during RSW [77, 78]. The concept of DR monitoring was pioneered by Hess and Ringer in 1938. They observed that during RSW of polished stainless steel, sheet-to-sheet DR initially increased to a maximum value and then decreased to a lower value because of the initiation and growth of a molten weld nugget. Subsequently, in 1951, Roberts noted the breakdown of contact resistance with the passage of a single cycle of high magnitude current on stainless steel and low carbon steel samples, establishing a foundation for DR to be used as a quality control method [66, 79]. The typical DR curve as shown in Figure 2.12 can be developed by plotting instantaneous voltage to current ratio over time and it serves as a powerful diagnostic tool to monitor weld quality [79], identify key phase transitions, and detect anomalies such as expulsion events.

In 1980 Dickinson *et al.* [80] advanced this concept by proposed six stage DR curve as illustrated in Figure 2.12. At the start of the weld cycle, electric contact is made between the copper electrodes and the workpieces. Surface contamination and oxides provide an overall high resistance. As soon as current is applied, intense localized heating occurs at the areas of high resistance usually faying surfaces, causes the surface contaminants to break down and resulting in sharp resistance drop. This initial transition marks the shift from insulated to conductive contact, enabling current to pass more directly between the metal surfaces [80]. Following the surface breakdown and contact stabilization, electrical contact is still controlled by micro-asperities and surface roughness. As current continues to flow, the asperities become softened and collapse under the pressure of the electrodes. The result increases the actual surface area, which reduces resistance. However, with the increase in the temperature the bulk resistivity of the material increases due to the positive temperature coefficient of the metals. The overall resistance during this phase reflects the competition between these two mechanisms. Initially decreasing to reach a minimum point (the α-trough), beyond which the rise in resistivity due to temperature dominates [80].

In a subsequent phase, the heat continues its progression further into the sheet material while simultaneously raising the temperature of the bulk metal. Since bulk resistivity continues to rise with temperature, total resistance increases steadily. This continual increase indicates more uniform heating and the approach for melting point at the interface [80].

Melting initiates at the sheet-to-sheet interface once the temperature at the faying interface reaches the melting point of the base material. The formation of a molten weld nugget leads to significant changes in electrical behavior. Although the bulk material continues to heat, the molten metal creates a higher conductive path, leading to a peak in resistance (β point). Investigations conducted by Zhao *et al.* [80] have revealed that the β-peak is single most important characteristics for expressing resistance signals in quality evaluation. At this point, the resistance reaches its highest value because melting has initiated but the molten cross-section area is still small. As the molten region expands and electrical conduction becomes dominated by the lower-resistance liquid metal, the resistance begins to decrease again [81].

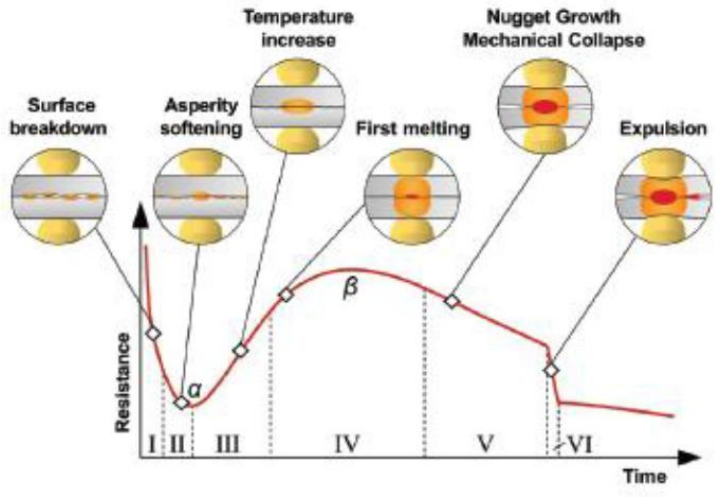


Figure 2.12. Resistance evolution during spot welding showing key stages: surface breakdown, softening, melting, nugget growth, and expulsion [80, 81]

Following the β peak, the nugget continues to grow in volume, and the molten zone continues to extend substantially across the faying interface. Simultaneously, the material surrounding the molten zone undergoes softening, and the molten region collapses under the electrode force, this phenomenon reduces the effective thickness of the sheet and decreases the length of the current path thereby further decreasing resistance. If heat input is excessive the volume of the molten pool may grow beyond the holding capacity of the surrounding solidified fusion boundary to contain it. Under electrode pressure, this excess liquid metal is forced out of the faying interface, resulting in molten metal ejection, or expulsion [72, 73] as explained previously. Expulsion is observed as a quick and sharp drop in resistance during stage VI of the welding curve as shown in the resistance curve Figure 2.12 and is typically undesirable, as it compromises weld quality, increases variability, and causes damage to the electrodes and sheets.

Recent investigations have proposed promising solutions to accurately detect and control expulsion, thereby improving weld quality. Valaee-Tale *et al.* [72] designed an analytical representation of expulsion using force and moment balance to predict the onset of expulsion as a function nugget size and electrode force. Xia *et al.* [82] implemented a multi-sensor monitoring system that included DR, electrode force, and displacement signals, supported by high-speed imagery to observe the severity of expulsion. Furthermore, Chen *et al.* [73] proposed expulsion detection method by integrating peak-to-peak amplitude and kurtosis index of the electrode force

signal using wavelet decomposition and a neural net analysis; the technique significantly improved defect identification in RSW compared to using an individual index alone. Together these studies demonstrate that the advance process monitoring and integration of machine learning (ML) on DR can effectively control and improve the weld quality and reduced defect rates.

2.4.4 Welding Schedules in RSW

RSW schedules define the process parameters such as squeeze time, current, interpulse cool time, hold time, and electrode force as shown in Figure 2.11(b). These parameters control nugget growth, and process reliability [83]. Single-pulse welding schedules (SPWS) as shown in Figure 2.13(a), employ a single current pulse throughout the weld time during RSW process, typically for short duration of 100-500 ms and are effective for simpler joints i.e., welding thin gauge mild-steel or low-strength steels [47]. However, SPWS presents significant challenges when applied to similar joints of AHSS i.e., rapid nugget growth due to their higher electrical resistivity form alloying emblements like manganese and Si, which concentrates heat generation and accelerates melting compared to mild steels. This rapid nugget growth results in narrow weldability lobes.

Multi-pulse welding schedules (MPWS) as shown in Figure 2.13(b), effectively address these limitations, by dividing welding current into two or more pulses with short cooling intervals of 20-100 ms. These intervals facilitate partial dissipation of heat and thereby extending the current range and improve process control during RSW [83, 84]. MPWS offer flexibility to optimize pulse shape, timing, and cooling based on sheet thickness, coating type, material grade, and some other factors. Studies indicate that weld joints made with MPWS improve strength over joints made using SPWS [84]. In addition to strength performance, MPWS effectively removes liquid metal embrittlement (LME) in zinc-coated AHSS by controlled removal during first pulse. Effectively optimized MPWS can decrease LME cracking up to 30% [83]. For complex stack-ups (3T or 4T), MPWS make sure that the nugget can grow in all interfaces especially in HSR joints [85], where SPWS presents challenges when applied to HSR joints i.e., narrow weldability lobes due to different electro-thermo-mechanical properties of materials. The inability of SPWS to tailor the thermal cycle in-situ can lead to expulsion due to over heating. Conversely, if parameters are adjusted to avoid expulsion, the nugget may not grow in between thin-thick interface, producing weak joints. These practices align with industry standards such as AWS D8.9 [86] and the AHSS Application Guidelines [22].

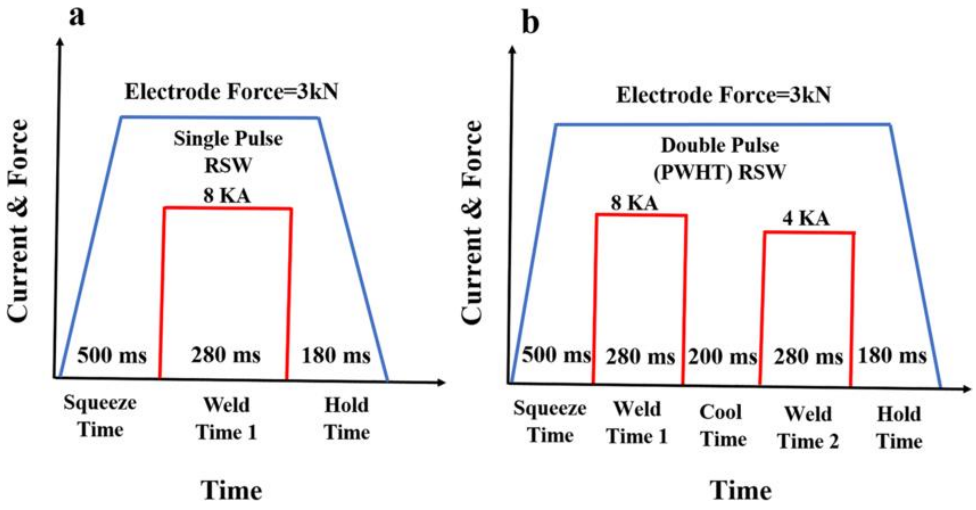


Figure 2.13. Comparison of welding schedules for (a) single-pulse and (b) double-pulse (PWHT) resistance spot welding, showing current, force, and timing parameters [2]

2.4.5 Characterization Techniques of RSW Weldability

Analyzing welded joint quality based on physical characteristics, microstructure changes, strength assessment, and failure mechanisms is crucial as it provides comprehensive information about the complicated interactions between welding parameters, material characteristics, and joint performance [28]. This multi-faceted approach enables researchers to create predictive models [69], optimize welding practices, and obtain reliable joint performance in critical applications.

2.4.5.1 Physical Attributes

The quality of RSW welds is usually assessed by cross-sections that show nugget shape, size, penetration, surface indentation, cracks, microstructure, and notch areas, as shown in Figure 2.14. Nugget shape is typically elliptical in 2 sheet similar material; the nugget is the main bond between sheets. Nugget diameter is generally 75% - 90% of the electrode diameter and depends on the size of the electrode and welding processes [87] and the size is dependant on weld current, electrode force and weld time. Excessive current can degrade electrodes and exceed thermal limits. Surface indentation caused by the pressure of the electrode and heat, is typically 10% - 20% of the sheet thickness [88]. Surface indentation greatly affects fatigue life by redistributing stress. Higher indentation can cause stress concentrations, which is particularly dependent on electrode shape, force, current, and weld time [4]. Shrinkage voids and porosities are common in fusion zones (FZ). Porosity is typically caused by trapped gases included from surface contaminants, rapid cooling

or a combination of both, while shrinkage voids can be caused by solidification shrinkage [4]. Voids can be particularly important in AHSS because they can initiate interfacal failure leading to reduced weld strength. Cracks can be developed from thermal stress under rapid cooling, which is affected by welding parameters such as hold time and the chemical composition of base metal and weld nugget [4]. The nugget mainly consists of martensitic columnar microstructure, which solidifies from the center outward as a consequence of the high cooling rates inherent to the RSW process [28]. Furthermore, Notch depth and shape are also very important in determining how the joint will fail.

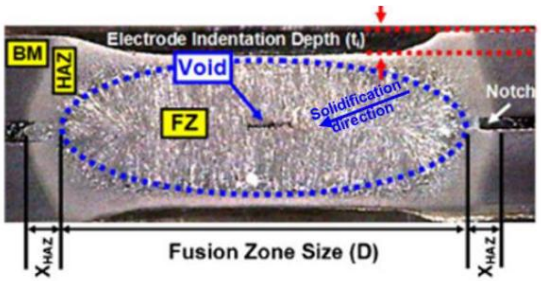


Figure 2.14. Cross-sectional image of a resistance spot weld showing the fusion zone (FZ), heat-affected zone (HAZ), base metal (BM), void formation, electrode indentation depth, solidification direction, and notch at the nugget–base metal interface [28]

2.4.5.2 Microstructural Transformation

The Figure 2.15 shows peak local temperature experienced during the welding cycle and corresponding microstructural evolution during RSW process [75, 89]. The FZ achieves nearly uniform peak temperature throughout its molten region and temperature then decrease outward from the fusion boundary through the HAZ into the unaffected BM. From the FZ to the BM each region undergoes to distinct microstructural transformation based on local peak temperatures and cooling rates [89]. The FZ experience temperature above liquidus, causing it to melt entirely and then cool quickly (10^3–10^5 °C/s) to form the predominant martensite microstructure. Adjacent to the FZ lies the coarse-grained heat-affected zone (CGHAZ), which is heated above the upper critical temperature Ac_3 but remains below melting significant grain growth and martensite upon cooling. Progressing outward, the fine-grained heat-affected zone (FGHAZ) was subjected to temperature above Ac_3 but below grain-growth temperature (~1100°C), which promotes recrystallization and the development of fine martensitic grains [75]. Beyond this region is the

intercritical heat-affected zone (ICHAZ) with peak temperature ranging between Ac_1 and Ac_3 experiences partial transformation to austenite and upon cooling this leads to mixture of tempered martensite (TM), RA, and some ferrite. Finally, the subcritical heat-affected zone (SCHAZ) underwent tempering, resulting in TM and some ferrite. These distinct microstructural zones are result of the different temperature distribution and rapid thermal cycles throughout the RSW process, which affect mechanical performance across the weld. Unlike traditional 2-sheet welds, the 3T and 4T stack-ups are more complex due to variations in heat flow, material thickness, and constituent alloys. Such complexities often produce asymmetric heat flow, uneven temperature distributions, and non uniformity of microstructural zone and increased complications in achieving nugget growth across all interfaces [90, 91].

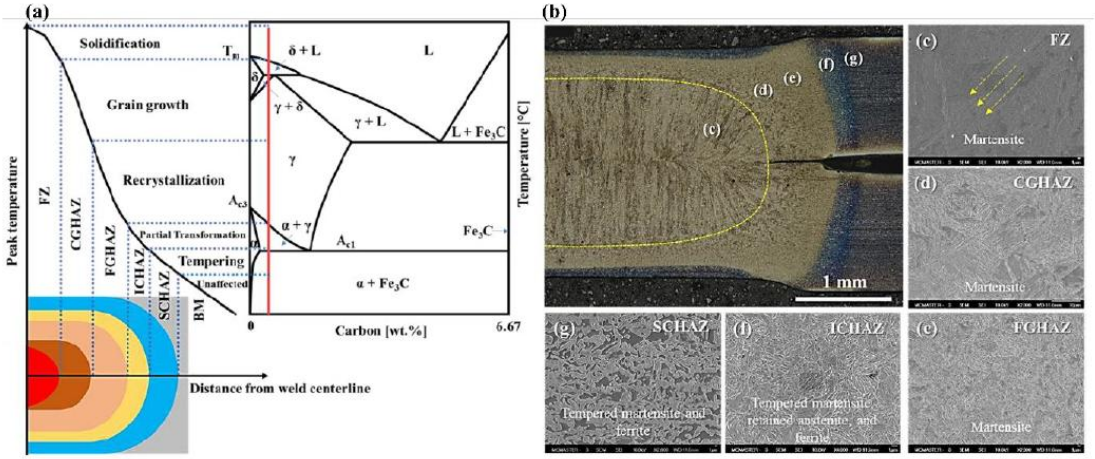


Figure 2.15. (a) schematic of the temperature profile with iron-carbon diagram to showcase phase transformations [89] *, and (b) optical and SEM images showing corresponding microstructures of fusion zone (FZ), coarse-grained HAZ (CGHAZ), fine-grained HAZ (FGHAZ), intercritical HAZ (ICHAZ), and subcritical HAZ (SCHAZ)* [75]

2.4.5.3 Strength Analysis

RSW welded joints strength evaluation provide assurance of minimum load-carrying capacities for BIW structures where joint performance is critical under service and crash impact [68]. Tensile-shear strength (TSS) and the cross-tension strength (CTS) test are among few ways to experimentally replicate different loading environments, and the schematic is shown in the Figure 2.16(a-b). The coupons sizes are stated in AWS D8.9 [92].

The TSS test applies load in parallel with the sheet interface in a lap-shear coupon as shown in Figure 2.16(a) reflecting the typical service loading condition while providing a direct measure of nugget strength and the overall weld quality. This method effectively measures the joint performance under in-plane forces typically encountered in vehicle BIW. While the CTS test applies tensile loading perpendicular to the sheet interface to mimic stresses during impact crash scenarios, or other dynamic loading conditions. The test characterizes the weld's resistance to through-thickness loading and provides information on the toughness and structural integrity of the joint [1, 93].

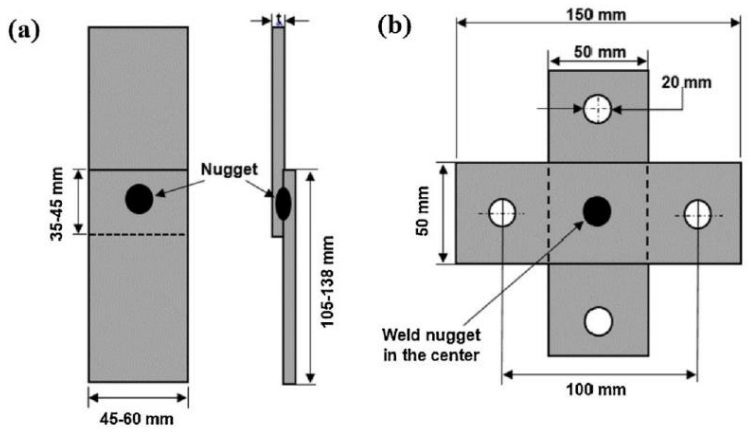


Figure 2.16. Standard specimen geometries for mechanical testing of RSW joints: (a) tensile-shear (TS) test and (b) cross-tension (CT) test, both with centrally located weld nuggets [68]

Studies have shown that weld nugget size is critical for strength and joint integrity [68, 94]. Larger nuggets improve shear resistance under TSS loads as a larger bonded area offers more resistance to shear stresses, while toughness and ductility of the weld microstructure influence the CTS performance, as harder more brittle microstructure (martensite) typically reduce the energy absorption and make the weld prone to brittle fracture [1, 93]. The measured data from TSS and CTS experiments can be used to make load displacement curve as a standard metrics for assessing the strength i.e., peak load (P_{max}), absorbed energy (W_{max}) and displacement before failure (L_{max}) and ductility of spot welds as shown in the Figure 2.17 [28]. Assessing energy absorption until the P_{max} is generally thought to be more precise for assessing weld strength. After P_{max}, the weld nugget is no longer the dole contributor to the load resistance and the joints often exhibit rotation, bending, or slipping at the grips. All of these post peak deformations artificially inflates the

apparent displacement without actually reflecting more weld fracture energy which can distort the measurement, and not represent weld's real energy absorption [68].

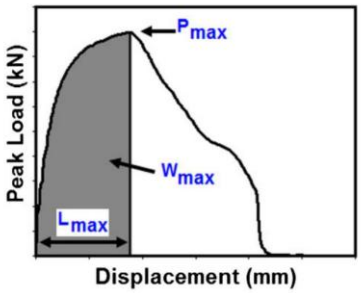


Figure 2.17. Typical load displacement curve during mechanical test [28]

2.4.5.4 Failure Analysis

As part of the analysis of fracture behaviour, it is important to consider the fracture type, crack propagation paths, failure locations, and the final appearance of the separated joint surfaces as fracture modes in RSW are critical for evaluating joint integrity. As per AWS D8.1 [70] guidelines, there are total 8 different types of fracture modes, but literature mainly centers on three more common failure modes: full interfacial fracture (FIF), partial interfacial fracture (PIF), and pullout fracture (PF) as shown in the Figure 2.18(a-c).

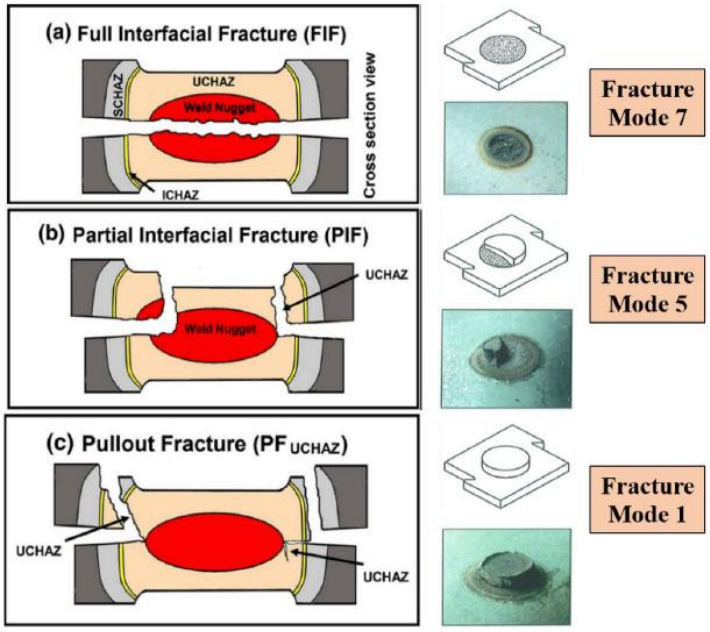


Figure 2.18. Fracture modes in RSW joints (a) Full Interfacial Fracture (Mode 7), (b) Partial Interfacial Fracture (Mode 5), and (c) Pullout Fracture (Mode 1) showing differences in crack path and weld integrity [70, 95, 96]

FIF (Mode 7) involves a brittle fracture that propagates directly across the weld nugget plane; FIF are most often associated with undersized nugget diameters, with the presence of welding defects such as porosity or shrinkage voids, or due to the presence of a brittle martensitic microstructure in the fusion zone [94]. Due to its brittle failure behaviour, this is typically an undesirable failure mode automotive failure prediction as it absorbs least impact energy. Sun *et al.* [95] reported that the welded joint of DP800 and TRIP800 failed in the same fashion because of below minimum nugget width requirement. PIF (Mode 5), begins by propagating across the nugget interface but deflects through sheet thickness direction once local tensile stresses exceed interface shear due to variations in microstructure [96]. Pouranvari and Ranjbarnoodeh [97] reported that DP600 welded joint significantly influenced by expulsion and high electrode indentation which shifted the failure location from BM to FZ/HAZ boundary due to stress concentration at the edge of weld nugget.

PF (Mode1) is most desirable failure as crack occurs through the nugget circumference and the weld button remains attached to one sheet, providing the significant plastic deformation, high peak load and absorbed energy [95]. The PF mode signifies the importance of adequate nugget size and appreciates the larger nugget size. Recent studies confirms that increasing FZ toughness or

hardness can shift failure modes from FIF to PF, while higher presence of martensite can reverse the transition [95]. In another study of evaluating DP780 weld join showed that an increase in nugget diameter from 3.4 mm to 6.6 mm led to CT failures changing from IF to PF proportionally increased load capacity [98]. These studies highlight that failure mode in combination with weld nugget size and microstructure determines whether the joint fails as FIF with little absorbed energy (FIF), or semi-ductility failure (PIF), or in the desirable ductile PF mode. Thus, control of heat input and post-weld hardness is an important factor in creating reliable automotive structures.

2.5 RSW of Complex Joint

Complex stack-ups are usually defined as more than two sheets with similar/dissimilar materials and equal/unequal thickness of the sheets [99]. The joining of two similar sheets through RSW is well established and optimized, however, joining three sheets that were equal thickness is more difficult than two similar ones, because it introduces an extra interface, and insufficient growth may occur due to the extra interface. In a three sheet joint made of uncoated low carbon steel, the critical thickness would be 1.5 mm or low, at which the nugget diameter at the geometrical center and the sheet-sheet interface will be approximately equal [28]. On the other hand, the nugget formation location shifts from geometrical center to sheet-sheet interface when the sheet thickness is more than 1.5 mm [28]. Dissimilar welding involves the joining of sheets with different chemical, physical, or mechanical properties and can be in a two-sheet (2T), three-sheet (3T), or even four-sheet (4T) joints [100, 101]. In modern vehicle designs, critical structural components such as pillars, floor reinforcement, and battery enclosure, are made of dissimilar sheets of varying grades and thicknesses of AHSS, as they offer efficient assembly of lightweight with tailored mechanical properties to help meet stringent safety and durability requirements [6].

2.5.1 Challenges in Dissimilar Welding

Dissimilar materials can introduce technical challenges in spot welding due to the differences in electrical resistivity, thermal conductivity, and chemical reactivity of the materials. The challenges can cause asymmetrical heat dissipation leading to inconsistent or incomplete nugget formation as shown in Figure 2.19(b) and increased risk of lack of fusion at thin-thick interface in 3T and 4T joint [6, 102–104]. The differences in thermal expansion coefficients can produce residual stresses and, current shunting and electrode wear can complicate process control. Surface defects and galvanic corrosion underscore the need of specialized process control and quality assurance when

welding dissimilar welding. The joining can be even difficult when a thin low carbon sheet is attached with multiple thick sheets of AHSS with thickness ratio of 5:1 or more in 3T and 4T configurations, this type of joint is also known high stacking ratio (HSR) joints as shown in Figure 2.20, which are increasingly common in advanced automotives [10, 105]. Per AWS D8.1 [70] minimum 20% nugget penetration is important in dissimilar joints to satisfy the for joint integrity.

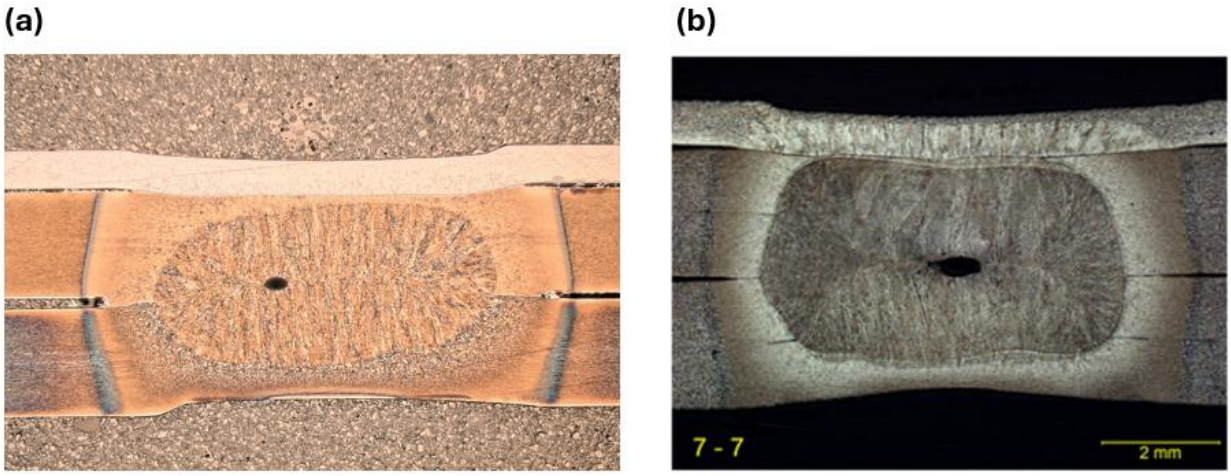


Figure 2.19. Cross-section of RSW joint showing (a) and (b) no nugget growth into thin-thick interface sheet in HSR joints [75]

2.5.2 High Stacking Ratio (HSR) Joints and its Challenges

Among asymmetric heat distribution, narrow weldability lobe, and interface nugget formation difficulties, the most critical challenge is to achieve nugget growth in thin-thick sheets interface in 3T or 4T joints as shown in Figure 19(b), as this interface experiences the most thermal imbalance due to contact resistance variations, thermal mass differences and electrode heat sink effects [106], [107]. For instance, Eizadi and Marash [7] reported that the thin top sheet's proximity to water-cooled electrodes accelerates heat dissipation, reducing the heat available for nugget formation at the thin-thick interface in 4T low carbon joints. Similarly, Lu *et al.* [6] studied the RSW of 3T dissimilar steel joints with both experimental work and finite element modeling (FEM). They reported that rapid heat loss to the electrodes limited nugget development at the thin-thick interface, resulting in asymmetric nuggets with greater penetration into the bottom thick sheet than the top thin sheet. Their validated model underscored the importance of optimized process control like the usage of multi-pulse or multi-stage welding schedules achieve better nugget growth in 3T

dissimilar AHSS joints. Currently, literature suggests three methods to improve the nugget growth in thin-thick interface; (1) process optimization or using advanced multi pulse technique, (2) modification in the weld consumables such as electrodes design, and (3) usage of adhesives between thin-thick interface to increase heat generation [108] all of which are comprehensively evaluated in coming section.

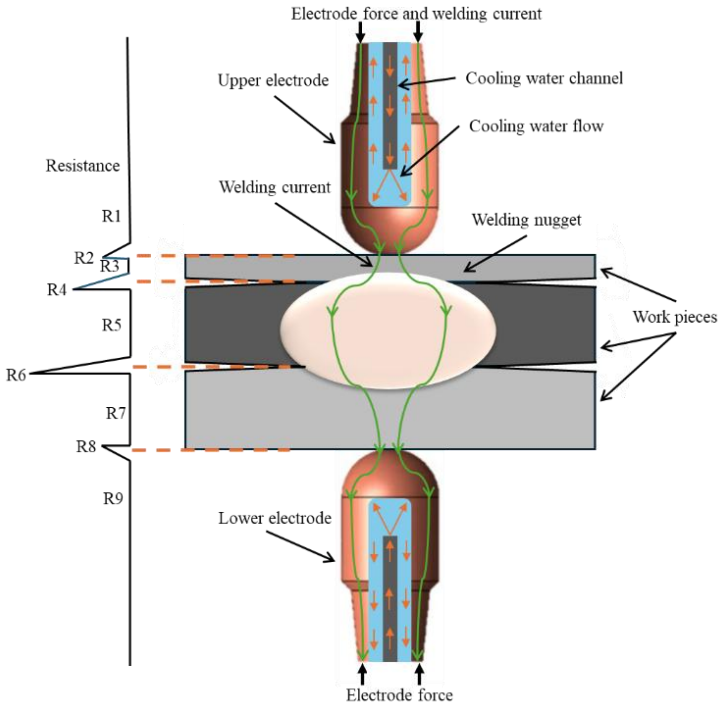


Figure 2.20. Schematic of resistance spot welding in a dissimilar high stacking ratio joint, illustrating current flow, force application, and nugget formation.

2.5.2.1 Process Optimization

As described earlier, MSWS can effectively address the weldability issues of AHSS and are particularly promising to tackle the heat balance difficulties of HSR joints. Gould *et al.* [10] reported that a two-stage welding schedule as shown in Figure 2.21 achieved 40% penetration into the thin sheet compared to the single stage conventional schedules. In first stage, a high welding current (10-12 kA) combined with low electrode force (2-3 kN) promoted heat generation at the thin-thick interface. In second stage, a lower current (8-9 kA) and higher electrode force (4-5 kN) facilitated complete fusion at both interfaces while minimizing expulsion. This dynamic approach effectively addresses the thermal imbalance in HSR dissimilar joints by adjusting the

force and current during weld cycle. Similarly, Ikeda *et al.* [109] found that implementing two stage control strategy resulted in 20% larger nugget diameter in all interfaces and cross tension strength improvement of 15-30%. The first phase applied high electrode force with lower current to stabilise contact and preheat the interfaces, followed by a second phase of low force and high current to concentrate heat generation. This strategy also reduced interfacial defects, mitigated expulsion, and minimized phosphorus segregation, thereby improving nugget toughness. In a study about nugget growth on 3T zinc-coated steel spot welds, Harlin *et al.* [8] found that electrode force is key in determining where the heat is generated and where the weld nugget forms. Importantly, they found that as electrode force increases, the weld nugget forms within the middle sheet, rather than at the interfaces. In addition to force and current schedule modification, usage of adhesive layer has also influence nugget growth in dissimilar 3T HSR joint.

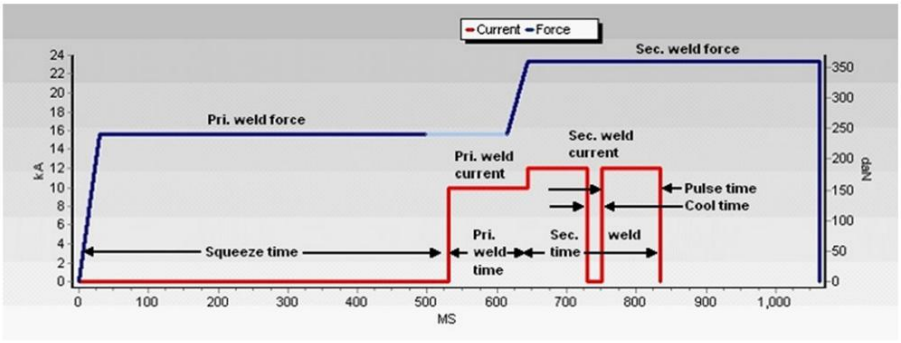


Figure 2.21. Multistage welding sequence for joining HSR [74]

2.5.2.2 Modification in Weld Consumables

Beyond process optimization, recent studies have highlighted the importance of electrode design to facilitate better welding and mechanical performance for HSR joints. Kim *et al.* [110] stated that the hollow conical shaped electrode as illustrated in Figure 2.22(a) increased the weldability range of the three-sheet RSW joints and improved mechanical performance. The conical shaped electrode reduced risks for expulsion as molten metal flows into conically electrode and expanded the weld lobe for the thin sheet HSR joint than using a regular domed electrode. The hollow electrode redistributes the current density, allowing for increased heat input, which drives the weldability between all sheets and resulted in in larger nugget diameters and higher shear strength. Coon *et al.* [111] studied RSW of a hot-dip galvanized DP600 steel joint where 0.8 mm thin sheet joined with two thicker 1.9 mm sheets. They examined how different shapes of electrodes (as

shown in Figure 2.22(b)) influence HSR joint weldability and endurance. Among all doomed shape electrode made welding more stable and faster because it had a higher current density from a smaller face diameter. Also, pulsed current did not change the acceptable current range for this joint.

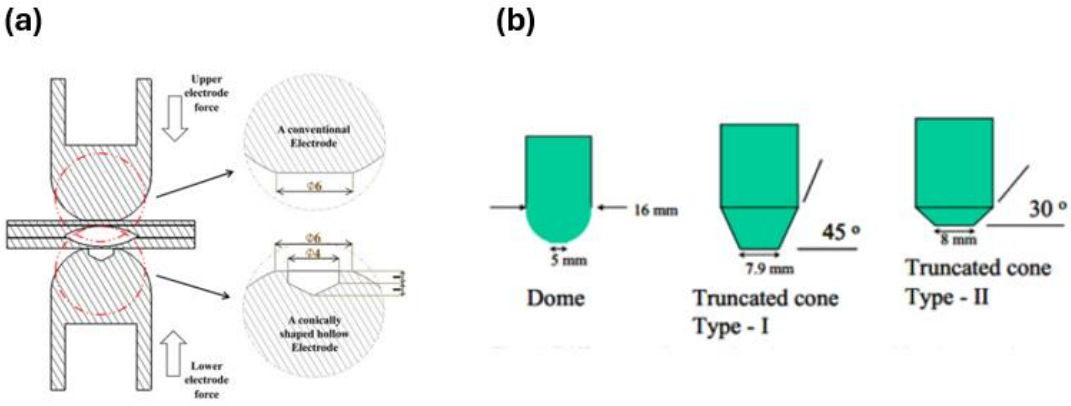


Figure 2.22. (a) 3T RSW configuration with upper and lower electrodes dimensions [86], *and (b) showing three different shaped electrodes* [87]

2.5.2.3 Mechanical Performance and Failure Modes

The mechanical behavior of multi-sheet resistance spot welds is not controlled by process parameters alone; joint geometry and the choice of materials are equally critical. Lei *et al.* [112] demonstrated that increasing electrode indentation depth in 3T DP600 RSW joints can significantly extends fatigue life under both TSS and CTS. Similarly, Ren *et al.* [113] examined the influence of chemical composition on the failure characteristics of three-sheet RSW joints made from dissimilar high-strength steels (B1500HS and B250P1) under TSS and CTS tests as shown in Figure 2.23(a-b). Joints that fail in pullout (PO) mode as shown in Figure 23(c) exhibit higher ultimate load and energy absorption than those failing in interfacial mode, and overall, joints absorb more energy in cross-tension than in shear due to additional structural deformation. In a related study, Wei *et al.* [114] Investigated joints made with different sequences of TRIP, DP, and TWIP steel sheets and observed the formation of asymmetric nuggets due to difference in the thermal conductivity and melting points. Tensile shear tests revealed that failure usually began at the smallest nugget interfaces (e.g., TRIP-DP, TWIP-DP) and indicated that mechanical performance (failure load, displacement, and energy) continued to improve as nugget diameter increased. Among all combinations, TRIP-TWIP-DP order yielded the best overall weld quality,

due to a favorable balance between heat generation and dissipation as well as the metallurgical compatibility of the materials. In addition to experimental investigations, finite element modeling approaches have been used to gain deeper insight into heat flow and nugget formation in three-sheet dissimilar joints.

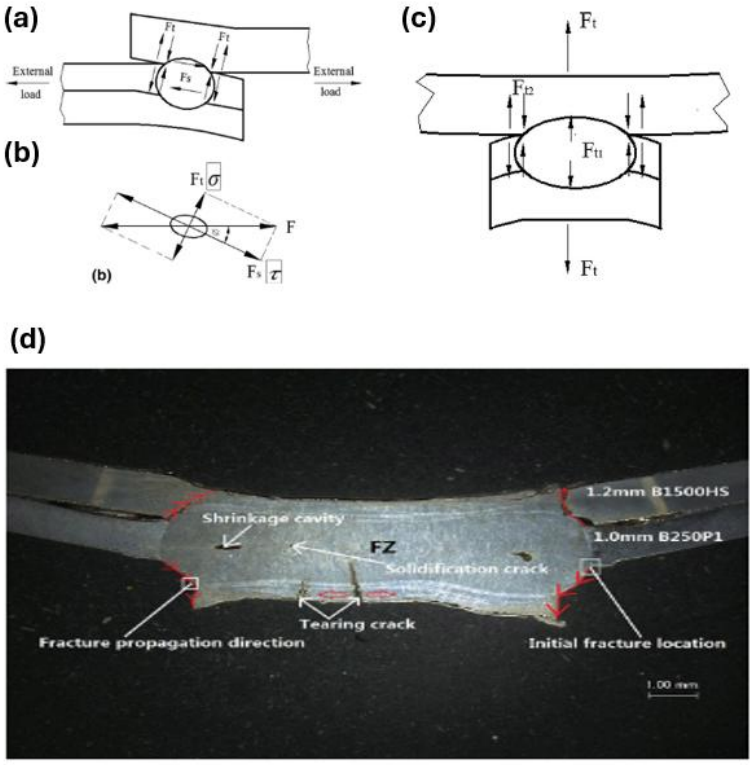


Figure 2.23. (a, b) Schematic diagrams of tensile-shear loading and force components on a 3T spot weld; (c) cross-tension loading configuration; (d) fracture features in a 3T dissimilar RSW joint showing crack paths and fusion zone [89]

2.5.2.4 Adhesives and Alternative Bonding Mechanisms

Due to technical barriers in achieving the nugget growth in thin-thick interface in HSR joints, there has been a growing focus on the use of interlayers as it provides extra resistance to current and generate more heat. Yu [90] used a 0.22 mm-thick PT3000 (a CrNi alloy) cover sheet between the electrode and the thin low-carbon steel of 0.7 mm-thick GA-coated with 2 mm-thick GI-coated DP980, and 1.6 mm-thick CP1180 steel sheets. Using the cover sheet made the joints stronger against tensile shear and made the nuggets go deeper into the thin sheet. The thin sheet facilitated the generation of more heat and lost less heat, which led to this improvement. Similarly, Zhao *et*

al. [115] found that applying an adhesive between the faying surfaces promoted earlier and larger nugget formation compared to conventional RSW. Manladan *et al.* [17] explored three sheet joints comprising magnesium alloy and austenitic stainless steel (AISI316L) using RSW in configuration Mg-AISI316L-AISI316L. By adding adhesive in Mg-AlSI316 interface and optimizing RSW weld parameters, dual bonding was achieved: a conventional metallurgical welding between AISI316L layers, and a brazing at Mg-AISI316L interface as illustrated in Figure 2.24(a-b). The resulting joints outperformed traditional RSW joints in peak load and energy absorption. Also, the failure mode changed from interfacial failure at the Mg nugget/upper AS interface with adhesive tearing, to partial interfacial failure also involving adhesive tearing. Further insights into solid-state bonding emerged from a separate investigation by Nielsen *et al.* [116] on spot welding thin low-carbon steel sheet to two thicker AHSS sheets using factorial experimentation and statistical modeling. Fusion occurred between the AHSS layers, while thin low-carbon AHSS interface showed solid-state bonding. Despite the lack of continuous nugget formation across all interfaces, the welded joints exhibited acceptable strength and ductile-assisted PO failures. The finding suggested that under certain conditions, solid-state bonding alone may be sufficient.

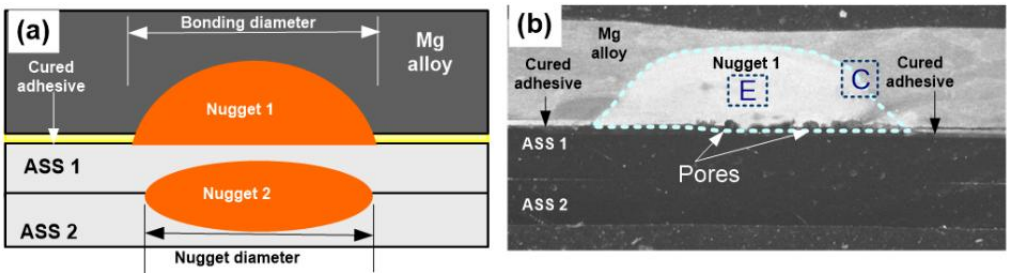


Figure 2.24. (a) Schematic and (b) cross-section of weld-bonded Mg alloy/ASS three-sheet joint showing nugget formation, adhesive layer, and porosity at the interface [17]

2.5.2.5 Modeling and Simulation of Nugget Growth

Simulation offers deeper understanding of physical processes i.e., RSW of different types of joints by analyzing how heat generation interacts with materials and assists in nugget growth. However, because simulation is based on idealized assumptions, it can not fully capture the complexities of the real world, making experimental validation essential. Despite the advantages, there is little research on numerical simulation of dissimilar 3T joints. Ma *et al*. [117] used their own developed finite element (FE) software JWRIAN, to make weld lobes for joint made of 0.7-mm 270C, 1.4-mm 590Y, and 1.8-mm 590Y. But their analyses didn't go into detail about nugget formation and

how welding parameters affect the size of nuggets at each faying interface. Nielsen *et al.* [116] simulated the process of forming nuggets in dissimilar 3T joints with variety of process parameters and their interactions but the nugget did not grew completely in to thin-thick interface and did not meet the minimum 20% penetration requirement, which is often needed for strong and reliable joints. In order to clarify how various combinations of steel grades and sheet thicknesses affect nugget diameter in both interfaces and penetration at the thin-thick interface during RSW of 3T HSR joint, Shen *et al.* [118] carried out an extensive numerical investigation using thermal-electrical-mechanical coupled FE. They reported that nugget formation begins at the interface between the 1.8-mm SAE1004 and 1.4-mm DP600 sheets and further the results showed that the stacking sequence and sheet thickness ratios have a significant impact on the size and penetration of the weld nugget. Notably, the critical thickness ratio between the top and bottom sheets should be roughly 1:3 to achieve the minimum acceptable nugget diameter and guarantee at least 20% penetration into the thin sheet, as shown in Figure 2.25. These findings offer crucial direction for multi-sheet joint design to maximize structural performance and weld quality.

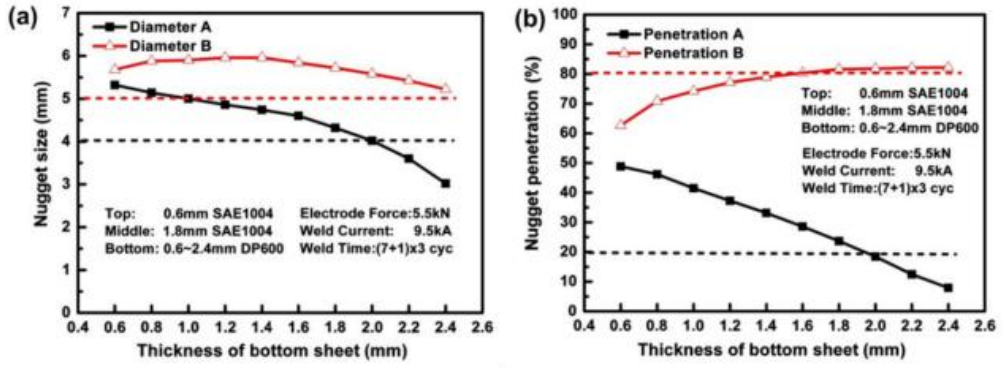


Figure 2.25. Effect of DP600 bottom sheet thickness on (a) nugget size and (b) penetration in 0.6-mm/1.8-mm SAE1004 and DP600 3-sheet RSW joints [118]

2.6 Modeling of Resistance Spot Welding

The assessment of spot-welded joint quality in industrial settings has traditionally relied on offline techniques such as destructive testing (peel, TSS, and CTS) to confirm nugget growth across all interfaces [119]. However, these methods can only be applied to a limited number of samples and are associated with several significant drawbacks, including the risk of overlooking hidden or intermittent flaws, considerable time and resource demands, and a lack of real-time quality

feedback during production. Consequently, production lines often use statistical sampling along with an operator's experience which increases the risk of undetected weld defects. Even with automated welding equipment, only a fraction of welds can be routinely checked, and manual production remains dominant [119]. Due to these restrictions, there is a growing focus on simulation models and data-driven methods that use the increased availability of process data (current, voltage, electrode force, resistance curves) as well as developments in machine learning (ML) and artificial intelligence (AI). These technologies promise to make weld quality assurance much better by allowing for continuous, real-time prediction, monitoring, and control of weld outcomes. This will make it less necessary to use damaging procedures and physical labour. When it comes to complicated, multisheet, different material joints, where process variability and fault mechanisms proliferate, the requirement for smart, adaptable, and strong prediction systems becomes even more urgent [120–122].

2.6.1 Physics Based RSW Modeling

The first 1D model of RSW was developed in the 1961 by Greenwood, which focused on temperature distribution, and thereafter 2D and 2D axisymmetric models were initially developed for thermal analysis and later for mechanical coupling, all these models were finite difference models. The introduction of the use of finite element models (FEM) in 1980 by H.A. Nied marked a transformational step [123]. Since then, physics-based and FEM became essential for investigating the coupled electrical, thermal, and mechanical phenomena that govern nugget formation, residual stresses, and distortion in RSW. These mechanistic models complement empirical approaches by providing predictive precision and enabling virtual prototyping and optimization. In early work, Moshayedi & Sattari-Far [124] developed a 2D coupled FE model and concluded that increasing the welding current from 6 kA to 10 kA or weld time from 10 ms to 40 ms to elevated tensile residual stresses by 50% at the nugget edge, which is significant for predicting fatigue and crack initiation. Pandya *et al.* [125] linked micro-mechanical property mapping with FE analysis to achieve high-fidelity predictions of fracture location and mode in DP600 joints.

The integrating of advanced commercial simulation software has played a key role in advancing and optimizing RSW process to enhance robustness and adaptability. Lu *et al.* [6] used ABAQUS

to developed a 3D coupled thermos-electro-mechanical FE model to simulate and predict nugget growth in 3T dissimilar joint. The model showed that increasing the weld current significantly enhanced nugget diameter and penetration at both interfaces but heat loss on the thin sheet side limits full penetration as illustrated in Figure 2.26.

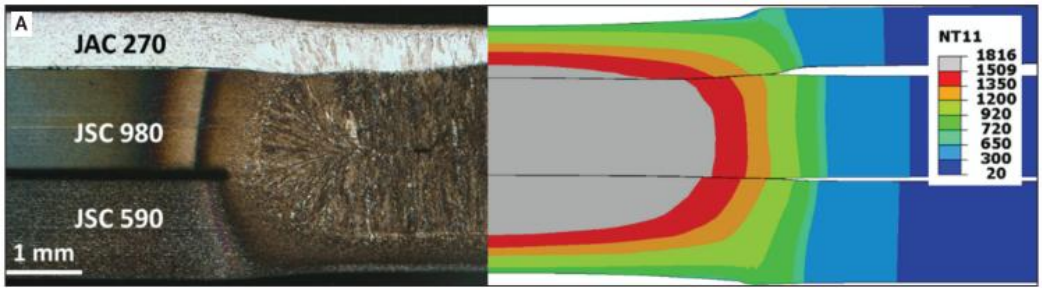


Figure 2.26. Cross-sectional micrograph and corresponding finite element temperature profile of a three-sheet dissimilar steel RSW joint (JAC 270/JSC 980/JSC 590), illustrating nugget formation and peak temperature distribution [71]

Nielson *et al.* [126] developed a 3D electro-thermo-mechanical model for RSW using SORPAS for prediction of nugget growth and mechanical test. Their model was able to accurately reproduce the weld nugget formation and expulsion threshold, and results were validated against experiments. Similarly, Löveborn [123] reported a strong similarity between the simulated data and experimental data using SORPAS. The differences did lead to adjustments in the values for the material properties to a point of optimized accuracy. Andersson and Melander [127] used SORPAS to predict the weld quality of ultra-high strength steels RSW joints. They reported mean absolute errors (MAE) of 0.68 mm in nugget size and 1.10 kA in expulsion limits across materials ranging from 280 MPa to 1500 MPa. In a study of uncoated DP steel, Ernst *et al*. [128] used Simufact Welding to model RSW 2T joint for better temperature predictions in welding. They also adjusted parameters such as coupling ratio and electro-thermal contact surfaces, and validated the model based on measured heat-affected zone and molten zone radii. Similarly, Venkatakrishnan [129] applied the COMSOL Multiphysics software to build electro-thermal models of RSW, with an emphasis on predicting temperature distributions that occur during the welding process. In this study, they incorporated interface resistance through the application of an equivalent thin layer concept, which allowed for faster simulation speeds without sacrificing accuracy. This work

demonstrated that COMSOL is suitable for simulating resistance spot welding and analyzing the effects of various process parameters on the temperature of steel sheets.

Although commercially available FEM software has made significant advances, but some limitations remain. FEM modeling approaches are computationally intensive with time and cost rising sharply as model complexity increases which makes it unreasonable to consider for large-scale production. The complexity of RSW arises from several factors, including the need for accurate material data input, calibration requirements, the use of advanced coated materials, HSR joints, and the challenge of capturing phase transformations and moving boundary conditions. These challenges have driven the adoption of data-driven methods (e.g., ML) that can provide accurate predictions in much shorter time and often with lower computational cost. However, it is important to note that, ML techniques do not yet fully replace physics base models for understanding fundamental mechanisms rather they serve surrogates tools for prediction and control. In more advanced hybrid framework, the integration of both FEM and ML models is being explored to enhance the understanding and prediction of complex welding phenomena [130].

2.6.2 Data-Driven Modelling in RSW

Initial attempts to forecast RSW results predominantly utilized, regression analysis, and empirical models, thereby creating the introductory quantitative frameworks for understanding the impact of process parameters on joint performance. These methodologies are fundamental, offering interpretable relationships that inform optimization and practical application, frequently acting as benchmarks for more sophisticated models. Although FEM provides insight into the physics of RSW, statistical and regression-based approaches provide more readily available methods for practitioners to optimize parameters for quality assurance. For example Ariyanto *et al.* [131] used Taguchi and analysis of variance (ANOVA) based modeling to determine welding current as the dominant factor for joint strength and nugget diameter in dissimilar mild steel/stainless steel resistance spot welds, where 75.08% of the variation in nugget diameter could be attributed to welding current and 12.35% was influenced by surface roughness. Ternane *et al.* [132] applied regression modeling and factorial design to 304L stainless/galvanized lap joints, confirming welding current as the key contributor to tensile-shear strength. Yu [78] proposed a regression-based adaptive resistance spot welding control scheme to effectively mitigate shunting effects by measuring dynamic resistance, the study showed improvements in nugget diameter and joint

strength. In another study, focusing on welding Ti alloy, Zhao *et al.* [133] developed a hybrid multi-objective optimization method that combined regression analysis and an entropy weight method and created an overall quality index based on process parameters and real time power signals, and verifying that welding current was the most influential factor for weld quality and energy efficiency. Although regression-based methods are interpretable and often sufficient for quality assurance, their predictive capacity is insufficient for high dimensional datasets and for non-linear data. High-dimensional datasets contain many features or variables, often exceeding the number of observations, which poses challenges for traditional regression approaches.

2.6.2.1 Machine Learning Integrated Models

Early hybrid approaches that bridged empirical and mechanistic methods such as fuzzy logic, interpretable AI, and hybrid artificial neural network (ANN) based regression models offered dynamic and transparent weld quality prediction without the drawbacks of purely physical models. For example, Hussein *et al.* [134] trained a fuzzy login controller (FLC) that was able to accurately predict nugget diameters and maximum shear strength as well as reliably predict possible weld defects (expulsion) prior to processing using their FLC model with high reliability, which eliminated the need for trial-and-test. The least squares assisted rule extraction from facts version 5 (LSRF5) method was created by Kitano *et al.* [134] and used neural networks and least squares regression to produce explicit empirical equations that relate welding parameters to nugget diameter. The model was trained on 117 experimental conditions and achieved a mean absolute percentage error (MAPE) of 2.98% on eight unseen data cases, showed strong generalization even with the limited data.

Thorough validation of models is important to demonstrate the validity and applicability of such predictive models. A variety of metrics i.e., coefficients of determination (R^2), root mean square error (RMSE), mean absolute error (MAE), MAPE, and mean bias deviation (MBD), are used for comprehensive performance assessment. Where each metric provides unique insights: R^2 indicates the variance explained and model fit; RMSE and MAE indicate the scale and nature of prediction error; MAPE allows for comparisons across scales; and MBD shows systematic over-or under-prediction, respectively. For example, Johnson *et al.* [134] examined RSW of DP780 steel and using ANN and adaptive neuro-fuzzy inference system (ANFIS) models as shown in Figure

2.27(a-b) to predict all primary weld quality metrics (nugget diameter, TSS, and dynamic resistance), achieving prediction accuracies of 99.36% and 99.98% for key weld quality metrics. ANN is a neural network model for pattern recognition, while ANFIS combines neural networks with fuzzy logic for both learning and interpretability. They also integrated multi-objective genetic algorithm with regression model, highlighting that the current was the most important variable contributing to weld quality, followed by electrode force and welding time. Using a multi-output least-squares support vector regression (MLSSVR) model optimized using chaos game algorithms (CGA), He *et al.* [135] focused on lithium battery pack RSW. Their proposed model demonstrated its usefulness for strict battery manufacturing quality requirements by accurately predicting nugget diameters and tensile shear loads with average relative errors below 4%, outperforming conventional methods for small, nonlinear, high-dimensional datasets.

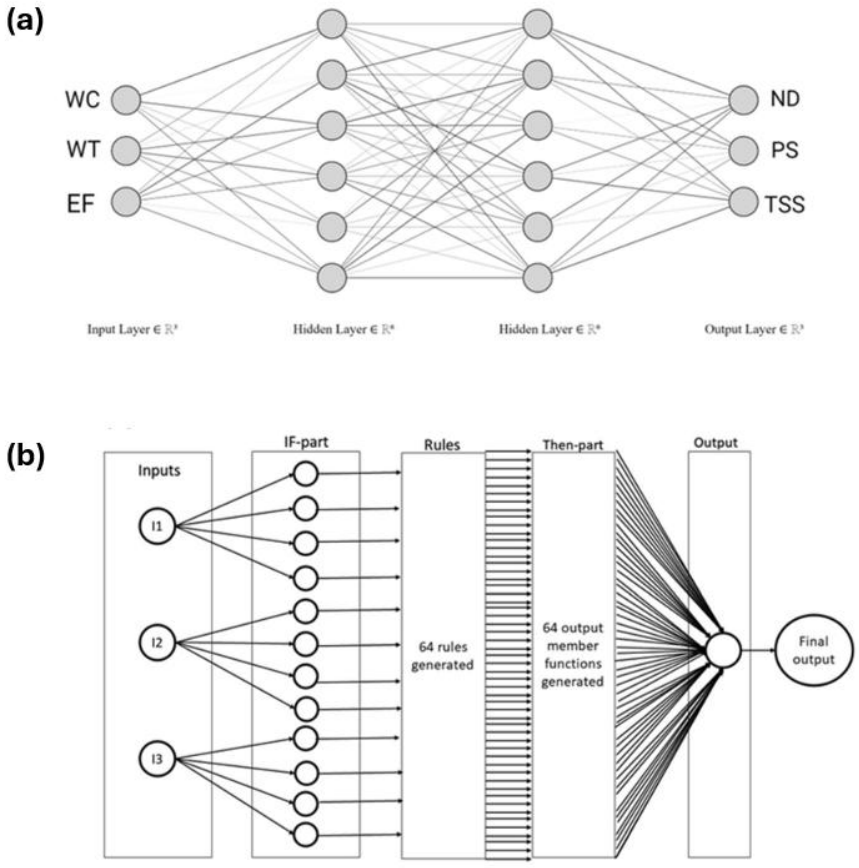


Figure 2.27. Showing (a) ANN model architecture, and (b) ANFIS model architecture [104]

Building upon these foundational studies, newer and more sophisticated data driven models have revolutionized RSW, enabling real time quality prediction, robust generalization to unexplored circumstances, and high-dimensional sensor data integration, leading to enhanced intelligent process control and adaptive manufacturing. In particular, Sim & Kim [136] created a hybrid nugget diameter prediction model for RSW that combines a physical model with a spline-based ML model trained and tested on 109 datasets from an automotive OEM. The model successfully identified anomalies and generalized well to new process conditions, surpassing conventional ML performance in noisy and limited data scenarios. Although designed for offline use, the model's contribution is to improve intelligent process control and weld quality assessment in data-constrained manufacturing. Yue *et al.* [137] advanced this by creating a multi-fidelity deep neural network (DNN) architecture is shown in Figure 2.28(a) by integrating FE simulation data with experimental fine-tuning. This improved accuracy by more than 30% and gave a mean absolute error (MAE) of 0.13 mm for predicting nugget diameter. Notably, their inclusion of base material properties as model inputs enabled generalization to different steel grades and joints. Panza *et al.* [65] used a neural network classifier for weld quality prediction under electrode wear, an example of new and used electrodes is shown in Figure 2.28(b), with 90% accurate classification and enabling real time identification of compliant and non-compliant welds using electrode displacement and force signals. Lee *et al.* [138] added real-time electrode misalignment detection for robotic RSW, and with support vector machine (SVM) and probabilistic neural network (PNN) classifiers on voltage/current features, they got more than 95% accuracy.

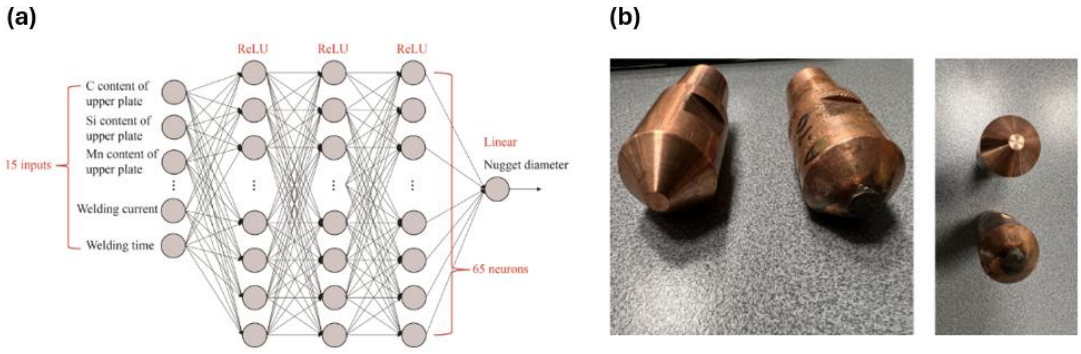


Figure 2.28. (a) Deep neural network architecture for nugget diameter prediction using 15 input features [107]; *(b) images of RSW electrodes used in experiments* [44]

The integration of physically constructed features based on domain knowledge has significantly progressed ML applications in welding and joining. Features such as energy density and heat input per unit force performed well compared to data-driven interactions. Physics-informed machine learning (PIML) frameworks, which combine domain expertise with computational power, resulting in models that exhibit better predictive accuracy, interpretability and robustness even with limited data. For instance, PHOENIX [130] frameworks outperformed in prediction accuracy (up to 98%) and generalization capabilities with small data set when integrated physical principles in the input. Studies have reported accuracy improvements up to 30% when physical relationships are correctly incorporated with process parameters. Similarly, Xia *et al.* [15] developed PINN for predicting RSW expulsion severity, resulted in 60% improved prediction compared to conventional ML models. However, data scarcity, computational time constraints in production environment, integration with existing quality control, and limited transferability of ML models across different welding and joining processes represent core challenges to their broader adoption.

2.6.2.2 Outlier Detection, Cross Validation and Hypermeter Tuning

When working with small or non-normal datasets, identifying and addressing outliers is important as they can introduce bias and compromise the reliability of the results. Researchers use a variety of statistical methods to find outliers and these include Grubbs' test, interquartile range (IQR) analysis, robust statistical measures, and exploratory data analysis (EDA). For instance, Mazher *et al.* [16] used IQR and robust statistical methods to remove outliers while, Xing *et al*. [79] combined Z-scores with minimum and maximum value exclusion. Similarly, Kang *et al*. [74] used visual robust techniques for detecting outliers.

Cross-validation and grid or random search has become foundational in ML, providing quick and effective framework for both model evaluation and hyperparameter optimization. K-fold cross-validation techniques, particularly with five- or ten-fold provides reliable performance estimates, help mitigates overfitting and provide high confidence in model generalization. However, when dealing with extremely small datasets ($n<100$), Leave-one-out cross-validation (LOOCV) may be preferable despite its higher computational cost, as it maximizes the use of available training data [139]. Combining grid search with cross-validation provides a thorough exploration of a hyperparameter spaces, resulting in better performance. These approaches have become

standardized through Python libraries such as scikit-learn, for ML applications for their reproducibility, interpretability and computational feasibility. Recent studies indicate these practices. Mazher *et al.* [16] integrated scikit-learn cross-validation and GridSearchCV library and reported R^2 of 0.94 and 0.89 for ANN and random forest models respectively. He *et al.* [135] utilized a chaos game optimization (CGO) algorithm to fine-tune hyperparameters of a multi-output least-squares support vector regression (MLSSVR) model. The implementation of CGO was to perform search across parameter space to find an optimal prediction model. The resulting model achieved RMSE of 0.024 for predicting nugget diameter, all with average relative error less than 4% indicating excellent generalization performance. While new optimized methods i.e., random search and Bayesian optimization are gaining credibility for their robustness and efficiency in high dimensional space, traditional grid search with cross-validation is still the gold standard for ML model development.

2.6.2.3 Benchmarking of ML Models

Benchmarking multiple ML algorithms is essential in RSW modeling to avoid bias and ensure robust, generalizable predictions. For instance, Chuenmee *et al.*[140] compared five ML models, including a feedforward ANN, CNN, long short-term memory (LSTM) network, random forest, and XGBoost with unseen test data for validation and achieved 97.1% accuracy with XGBoost. Similarly, Mezher *et al*. benchmarked 10 ML models including random forest, SVM, ANN, and linear models to predict both shear force and nugget diameter of 2T RSW welded joints. Hu et al. compared standard backpropagation neural network with advanced meta-heuristic optimization method, such as Sine-SSA while, Zhao et al. evaluated decision trees, RF, XGBoost. with grid search/CV.

In a large-scale industrial application, Zhou *et al.* [141] used feature-engineered ML to predict quality across two automotive production lines, using data from 27 welding machines and thousands of welds (roughly one station had 5,839 labelled operations). They used time-based factors i.e., electrode wear, dress cycles, and program order, and made more than 160 features for comprehensive evaluation. Using 12 ML pipelines (basic ML pipeline is shown in Figure 2.29) combining various feature sets with linear regression, multilayer perceptron, and SVR, the models enabled real-time prediction of weld quality indicators (Q-Value) before operation, thus supporting

generalization to unexplored process conditions and joints. Their approach also facilitated model interpretability, linking engineering domain knowledge with ML insights.

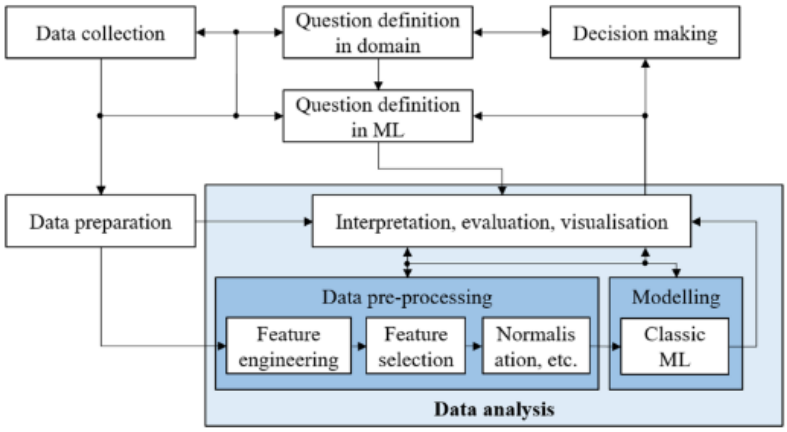


Figure 2.29. Basic ML pipeline [110]

Similarly, Gavidel *et al.* [142] conducted a comprehensive comparison of algorithms including DNN, ANN, support vector machines (SVM), and random forest (RF) for predicting nugget width in RSW. With 330 dataset the MAE was 0.041 mm, 0.065 mm, 0.067 mm, and 0.074 mm for DNN, ANN, RF and SVM models respectively. To reinforce the statistical supremacy of DNN they used pairwise t-tests. DR curves and an enhanced generative adversarial network (GAN) with a variational autoencoder (VAE) and channel attention were combined in a novel defect diagnosis method by Geng *et al.* [143] to address the lack of labelled RSW defect data. This approach reconstructs and augments key defect samples namely burn-through, under-welding, and splash by focusing on DR curve segments most indicative of defect characteristics, while excluding non-informative early-stage data and applying Savitzky-Golay filtering for signal smoothing. A compact convolutional neural network (CNN) is trained for multi-class defect classification using the generated data and real samples (approximately 145 for each defect type). Even with small, unbalanced datasets and high process variability, this GAN-enhanced CNN model demonstrated strong generalization in identifying rare defects and achieved a diagnostic accuracy of 98.4% on test data, significantly outperforming traditional methods. This allowed for dependable real-time process monitoring and quick online quality prediction.

2.6.2.4 Inverse Prediction and Experimental Validation

Inverse prediction refers to determining input process parameters to achieve desired output. It accelerates process development, reduces costs, enables multi objective optimization and support quality assurance. to market a product, reduces costs, satisfies multi-objective optimization, and supports quality assurance.

Statistical tools like Minitab have been widely used for inverse prediction using Response Surface Methodology (RSM), factorial design, and desirability function optimization [144, 145]. Researchers use Minitab to create regression models that link process parameters to desired properties and then invert these models to find optimal input settings. For instance, Rawal *et al.* [144] utilized Minitab's RSM and desirability to maximize tensile strength and maximize nugget diameter in RSW of low-carbon steel. Their predicted results closely matched experimental findings. Similarly, Çelik and Gürbüz [146] utilized Minitab's to develop a factorial design of experiments with 7 process parameters including sheet thickness and reported high predictive accuracy for both nugget diameter and tensile strength for RSW joints. Despite the acknowledged successes, there are inherent limitations of Minitab based statistical models. They rely on the assumptions of simple linear, or polynomial relations. These models do not adequately reflect complex, nonlinear effects and the interactions among input variables. They begin to lose accuracy when dealing with many variables, noisy data, or complicated process dependencies. Additionally, Minitab's framework lacks the flexibility needed for adaptive or real-time optimization in advanced manufacturing environments.

Comparative studies show that ML models usually offer greater accuracy than traditional statistical methods. These models are better at capturing nonlinear, high-dimensional, and complex relationships between inputs and outputs. Maculotti *et al.* [147] found that ML models like Gaussian Process Regression and neural networks predicted welding outcomes more accurately than statistical methods. Similarly, Aktepe *et al.* [148] used a reverse neural network to predict optimal welding parameters for brass wire welding. Their approach significantly reduced defect rates and operational costs after experimental validation.

Hybrid methods that combine both statistical design and ML models offer better results. For example, Meng *et al.* [149] combined Gaussian Process Regression and SVR within a traditional RSM framework that improved prediction and optimization of the ultrasonic metal welding

process. While experimental validation is paramount for both statistical and ML approaches, for 2T similar material joints the literature has shown that both types of models tend to predict outcomes of the process within 10% of those achieved experimentally. While ML offers advantages in nonlinear/high-dimensional scenarios, physics-based methods remain valuable when sufficient data is unavailable, or model interpretability is critical.

2.7 Summary and Research Gaps

Despite significant progress in RSW of dissimilar HSR joints, several important research challenges remain. Most existing studies have focused on nugget formation and growth under the influence of a limited number of process parameters, often using conventional SPWS or MPWS with up to three pulses of varying current magnitude. However, there has been no systematic investigation into nugget development using fixed-current MPWS with up to five pulses and six process parameters, through extensive design of experiments (DOE). The mechanisms underlying progressive nugget growth during MPWS are still not well understood, as experimental studies using interrupted testing to track nugget development at each stage are largely absent. These gaps are especially critical because MPWS could potentially enhance joint performance and address challenges such as inadequate nugget growth at the thin-thick interface in HSR joints. There is also a lack of comprehensive studies on the mechanical strength, crack propagation, and failure modes of hybrid bonding joints, especially those that combine partial fusion with brazing or solid-state diffusion at thin-thick interfaces in HSR configurations.

In the field of data-driven modeling, most research relies on large datasets, augmented data, or numerical simulations to predict RSW quality. There is a clear lack of studies predicting weld characteristics in HSR joints such as maximum nugget diameter and penetration into the top sheet using truly limited experimental datasets. Moreover, systematic comparisons of different supervised ML regression models including decision trees, random forest, support vector regression, and gradient boosting model for not only increasing the R^2 model variability but also predicting weld quality for HSR joints have not been reported. The versatile model aims to demonstrate that reliable predictive results can be achieved using limited data, supporting robust analysis of weld quality in advanced, realistic manufacturing scenarios.

3. Methodology

3.1 Materials

The present work investigated three-sheet RSW joints composed of DDQ270 (0.65 mm), PHS2000 (2.00 mm), and 1G-1180 (2.00 mm), arranged in that order. DDQ270 and 1G-1180 were hot-dip galvannealed (GA) steels with a coating weight of 45 g/m² on each side. PHS2000 was supplied in the hot stamped condition and coated with an AlSi layer having a total coating weight of 150 g/m². The chemical composition of the base materials (BM) may be found in Table 3.1. To compare the hardenability of the materials, the Yurioka's carbon equivalent (Ceq) [150] was calculated for each steel. The mechanical properties of each steel were measured according to ASTM E8 [151] and the resulting values are summarized in Table 3.2. All mechanical properties are presented as mean with tolerances representing the standard deviation calculated from five independent tensile tests per material.

Table 3.1. Chemical composition (wt.%) and carbon equivalent (Ceq) of the investigated materials.

Material	C	Mn	Si	Cr	Nb+Mo+Ti	Ceq
DDQ270	0.00	0.13	0.00	0.00	0.04	0.04
PHS2000	0.30	0.54	0.60	0.40	0.26	0.61
1G-1180	0.10	2.59	0.40	0.00	0.14	0.61

Table 3.2. Mechanical properties, including 0.2% offset yield strength (YS), ultimate tensile strength (UTS), (measured using the 0.2% offset method), total elongation (TE), and uniform elongation (UE) of investigated materials.

Material	YS (MPa)	UTS (MPa)	TE (%)	UE (%)
DDQ270	142.1 $\pm$ 11.1	282.8 $\pm$ 5.1	31.1 $\pm$ 0.6	20.76 $\pm$ 1.1
PHS2000	1292.5 $\pm$ 54.7	2004.1 $\pm$ 65.1	6.7 $\pm$ 0.3	11.4 $\pm$ 0.1
1G-1180	831.1 $\pm$ 29.1	1215.5 $\pm$ 21.5	8.5 $\pm$ 0.4	5.9 $\pm$ 0.2

Representative engineering stress strain curves for each material are illustrated in Figure 3.1(a). The PHS2000 exhibited ultimate tensile strength (UTS) exceeding 2000 MPa with limited elongation, 1G-1180 demonstrated UTS of 1250 MPa and DDQ270 recorded the lowest UTS

(280 MPa) but highest elongation among the tested materials. Scanning electron microscope (SEM) images of the as-received base materials are shown in Figure 3.1(b-d) where DDQ270 displays large, equiaxed ferrite grains. PHS2000 reveals a highly dense, martensitic microstructure, and 1G-1180 shows a fine, mixed microstructure of martensite and ferrite.

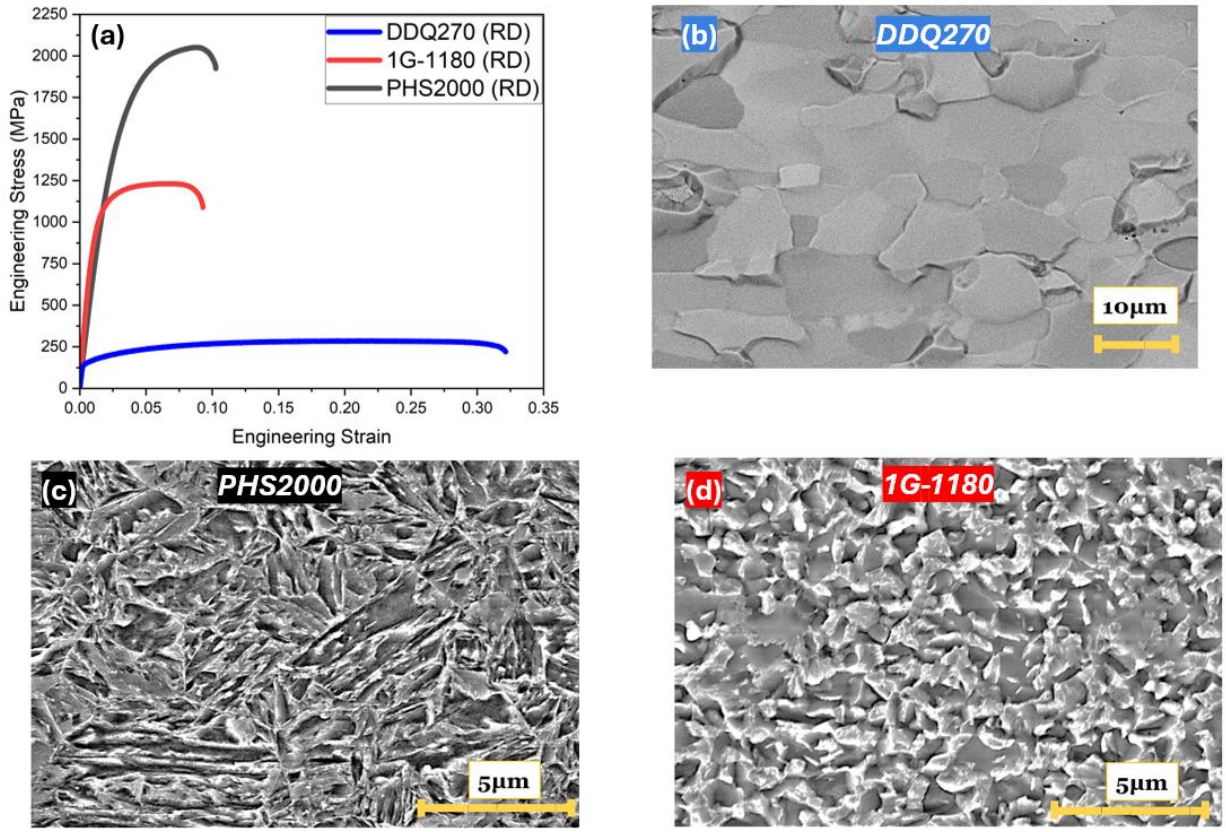


Figure 3.1. Engineering stress-strain curves of the three base materials investigated in this study along the rolling direction (RD). SEM images showing (a) low carbon steel exhibiting ferritic microstructure (b) Fine martensite laths suggesting high strength steel, and (c) dense structure characteristics of ferrite and martensite.

3.2 Resistance Spot Welding (RSW)

The weld coupons were made in thin-thick-thick configuration, with DDQ270 contacting the positive (upper) electrode and 1G-1180 contacting the negative (lower) electrode. Welding was done using a C-type welding gun equipped on a robotic welding system controlled by a Bosch Rexroth MFDC power source. Welding was performed on three different coupon sizes: 25 × 25 mm for microstructural analysis, 150 × 50 mm for cross-tension strength (CTS) testing, and 138 ×

50 mm for tensile-shear strength (TSS) testing as per AWS D8.9 [152]. Both the upper and lower shanks were fitted with a Cr-Cu class 2 dome type 6 mm face diameter Resistance Welder Manufacturers Association (RWMA) electrode. Both electrodes were water-cooled with a nominal flow rate of 6 L/min. The surface of each weld coupon was cleaned using methanol before welding to minimize contamination on the coupon surfaces.

Six key process parameters were selected to study their effects on nugget growth at both interfaces. These parameters were established through preliminary experimental trails. The expulsion threshold was determined to be 10.1 kA with an electrode force of 2.1 kN, so the maximum current (I_{max}) was set at 100 A lower than the expulsion limit. Minimum weld current was determined to be 7 kA, at which no fusion or bonding occurred between the top sheet and the remaining two sheets. It is acknowledged that this definition of minimum weld current is less than the $4\sqrt{t}$ criterion specified in AWS D8.9, which is widely applied for two sheet RSW. However, this approach was adopted because it provides a clear baseline for studying nugget initiation in three sheet joints, which present unique challenges not fully addressed by traditional two sheet standards. Three repetitions were made at each current level to determine repeatability for establishing the current lobe.

Figure 3.2(a) illustrates the configuration of the HSR dissimilar 3-sheet RSW joint used in this study. The schematic highlights nugget penetration into the top sheet and geometric parameters including weld nugget height and interface widths at both the thin–thick and thick–thick regions. The required minimum nugget diameter was calculated using the $4\sqrt{t}$ expression by AWS D8.9 [152], where t is the thickness of the thinnest sheet at the specific interface. The minimum nugget size required for thin-thick interface was 3.22 mm, and for thick-thick interface was 5.65 mm.

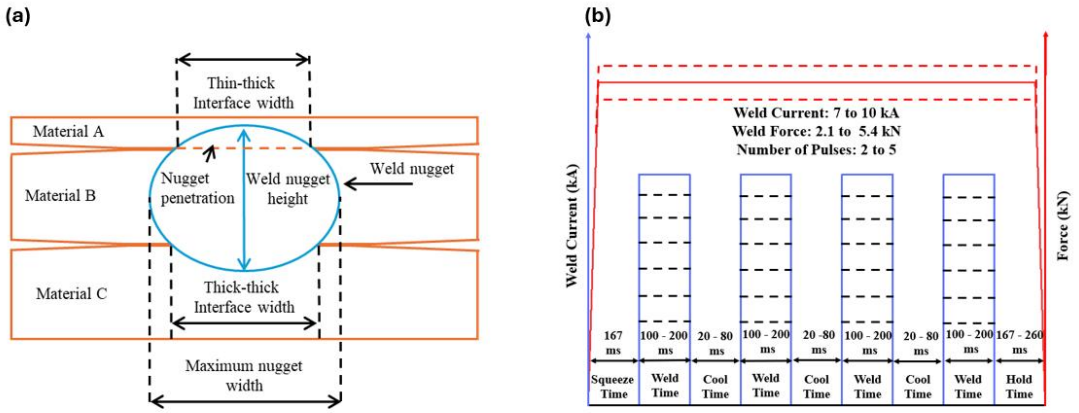


Figure 3.2. Schematics of (a) HSR 3-sheet RSW joint showing nugget penetration and geometric parameters across thin–thick and thick–thick interfaces, and (b) multi-pulse RSW schedule used in this study.

3.3 Design of Experiments (DOE)

To ensure comprehensive and efficient exploration of the RSW process window particularly for dissimilar three-sheet configurations with a high HSR, a hybrid design strategy was employed that combined latin hypercube sampling (LHS) and box-behnken design (BBD). This integrated approach yielded a total of 80 experimental runs, enabling broad and balanced coverage of the multidimensional parameter space. The chosen parameters and their experimental ranges are shown in Table 3.3. and a corresponding schematic of the weld schedule illustrating all parameters is shown in Figure 3.2(b). The rationale for combining LHS and BBD was to capitalize on the strengths of both methods while mitigating their limitations. LHS offers a well-dispersed sampling across the chosen range of each input parameter, which enhances global representation; however, it can sometimes overlook important interactions among variables. In contrast, BBD is more efficient at capturing quadratic and interaction effects with fewer runs than a full factorial design, but it avoids testing combinations at the extreme high and low ends of the parameter ranges, potentially limiting exploration of boundary conditions. Integrating of LHS and BBD resulted in a robust design capable of capturing both broad parameter variability and key interaction effects. Statistical analysis of variance (ANOVA) was used to determine the influence of selected input parameters on the nugget growth at a 95 % confidence level. Parameters with p-values below 0.05 were deemed statistically significant.

Table 3.3. Range of input process parameters investigated 3T HSR RSW schedules investigated.

Factor Name	Lower Limit	Upper Limit
Current (kA)	7	10
Force (kN)	2.1	5.4
Hold Time (ms)	167	260
Weld Time (ms)	100	200
Cool Time (ms)	20	80
Number of Pulses	2	5

3.4 Characterisation

Following the RSW process, the welded samples of 25x25mm were sectioned through the center using SiC cutting disc on Struers abrasive saw. The one-half part of welded joints was then hot mounted in conductive epoxy resin for microstructural observations. Mounted samples were ground and polished following standard metallographic procedures to a final finish using 1 μm diamond suspension. Polished samples were then etched with a 2% nital solution (2% nitric acid and 98% ethanol) for approximately 4-7 s to reveal the microstructure.

Microstructural examination of all 80 welded samples was conducted using optical microscopy (OM), while a subset of samples was selected for analysis by SEM. Microhardness maps were measured from three selected welds using a Clemex CMT automated Vickers hardness tester using a 200 g load and a 10-second dwell time. The profile pattern made approximately 30 indentations from the base material into the heat-affected zone (HAZ) of the middle sheet, followed by an additional 60 indentations diagonally from the top sheet's HAZ to the bottom sheet's HAZ. To avoid interference between strain fields of adjacent indentations was greater than three times the indent size, conforming to ASTM E384-22 [153] .

To study nugget development during the welding cycle, interrupted weld tests were performed for two distinct conditions; the no-nugget-penetration (NNP) condition, where there was no nugget growth into the top thin sheet, and the nugget-penetrating (NP) condition, which exhibited nugget growth into the top sheet. Each condition had four interrupt stages, where the welding process was stopped immediately after each pulse. The corresponding weld schedules are summarized in Table 3.4.

Table 3.4. Weld schedule used for mechanical and interrupted testing

DOE Condition	Nugget Growth Status	Force (kN)	Current (kA)	Weld Time (ms)	Cooling Time (ms)	Number of Pulses
(NNP)	Without nugget growth into top thin sheet	2.1	8.14	200	72	4
(NP)	With nugget growth into top thin sheet	4.5	8.65	200	75	4

Weld were mechanically tested to determine their tensile shear strength (TSS) and cross-tension strength (CTS) methodology modified from AWS D8.9 [152]. The geometries used are shown in Figure 3.3. Five repeats were done for each condition. Tests were performed using a 100 kN capacity MTS Landmark universal testing machine, using a crosshead speed of 10 mm/min. To minimize sample rotation, shims were used for TSS testing. All error bars and tolerances from the strength data represent the 95% confidence interval of the data. After initial testing was completed, interrupted testing was at to 90% of joint peak load to observe the failure propagation path in the welds.

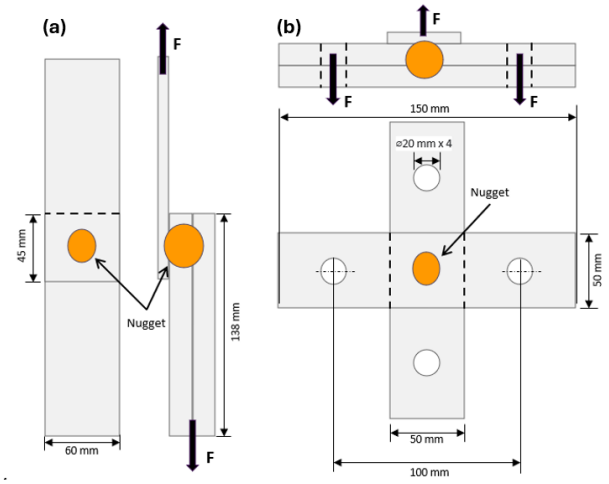


Figure 3.3. Schematic representation of mechanical test configurations for evaluating weld strength in three-sheet stack-ups: (a) TSS with load applied in shear direction, and (b) CTS designed to apply normal direction.

3.5 Data Driven Supervised Machine Learning Methodology

3.5.1 Data Acquisition and Feature Engineering

A dataset comprising 80 experimental runs was used following the systematic DOE framework discussed in section 3.3. Each run included six process parameters as input features: welding current, electrode force, hold time, weld time, cooling time, and number of pulses. The primary response variables were maximum nugget diameter and nugget penetration into thin sheet. In addition to the primary process parameters, several constructed features were also derived from fundamental physical relationships.

3.5.2 Data Preprocessing

To assess data normality and identify potential outliers in the measured dataset, the data was plotted on Anderson-Darling probability plots and subjected to Grubbs' test using Minitab Statistical Software v21.1.0. Identified outliers were removed from the data set, ensuring data integrity for subsequent modeling. All the input features were normalized using Z-score normalization formula as shown in Equation 3.

$$z = \frac{x - \mu}{\sigma} \tag{3}$$

Where x is the original value, μ is the sample mean, and σ is the standard deviation. This normalization step ensures every feature has a uniform scale (mean = 0, standard deviation = 1), improving algorithm convergence speed and avoiding situations in which features with greater numerical range dominate the learning process.

3.5.3 Model Selection and Implementation

Six ML based regression algorithms were used for modelling and performance comparison. These included linear models (ridge, and lasso regression), tree-based model (decision tree), ensemble methods (random forest and gradient boosting), and kernel methods (SVR). This evaluation framework is based on standard benchmarking practice in ML, where comparing multiple algorithms is necessary to find the most effective model. The diverse algorithmic representation ensures robust model selection and mitigates any bias towards single model, which is in line with best practices for predictive modelling [149, 154, 155].

3.5.4 Validation, Hyperparameter Tuning, and Performance Metrics

To ensure a representative distribution of the target variables, the data was randomly divided into training (80%) and test (20%) sets. The training set was subjected to five-fold cross-validation for robust hyperparameter tuning, with grid search being used to choose the best model parameters. As shown in Table 3.5, hyperparameter ranges were set based on established best practices for each algorithm. The comprehensive evaluation of model accuracy was assessed using five metrics: the coefficient of determination (R^2), root mean squared error (RMSE), mean absolute error (MAE), mean absolute percentage error (MAPE), and mean bias deviation (MBD).

Table 3.5. Optimized hyperparameters of all ML models

Model Name	Hyperparameter	Function	Values
Ridge Regression	alpha	Controls the strength of regularization	[0.01, 0.1, 1, 10, 100]
Lasso Regression	alpha	Controls sparsity and regularization strength	[0.01, 0.1, 1, 10, 100]
Decision Tree	max_depth	Limits how deep the tree can grow	[2, 4, 6, 8, 10, 14, 20]
Random Forest	n_estimators	Controls stability and accuracy	[100, 200]
	max_depth	Reduce overfitting and underfitting	[3, 5, 7, 10]
SVR	C	Provides penalty parameters for errors	[0.1, 1, 10]
	epsilon	Margin of tolerance toward errors	[0.01, 0.1, 0.5]
Gradient Boosting	n_estimators	Controls model capacity and reduce variance	[100, 200]
	learning_rate	Determines the contribution of each tree to overall model	[0.01, 0.1]
	max_depth	Controls model complexity and capacity to interactions and non-linearities	[3, 5, 7]

3.5.5 Inverse Prediction and Experimental Validation

After determining the best prediction ML model, an inverse prediction process was then implemented to find optimal combinations of process parameters aimed dual prediction of maximum nugget diameter and nugget growth into the thin sheet. Grid search and optimization algorithm search through the model's input space was performed to generate parameter sets that were predicted to achieve the desired response. For comparative validation, a corresponding set of

optimal process parameters was also identified using Minitab statistical tool, targeting the same output criteria. Each recommended condition from both approaches was experimentally tested in triplicate to ensure statistical reliability. The experimental findings were systematically compared with their respective ML model and Minitab to quantitatively evaluate the practical validity and predictive reliability of the modeling framework.

3.5.6 Computational Implementation and Reproducibility

All data pre-processing and cleaning was done in Minitab statistical software. The actual modeling and analysis of ML models was completed in Google Colab, as it provided more computational power than local machine. The entire ML modeling workflows were documented in Google Colab within organized and well-commented Python scripts. A flowchart as shown in Figure3.4 summarizes the complete pipeline from data acquisition to interpretability analysis.

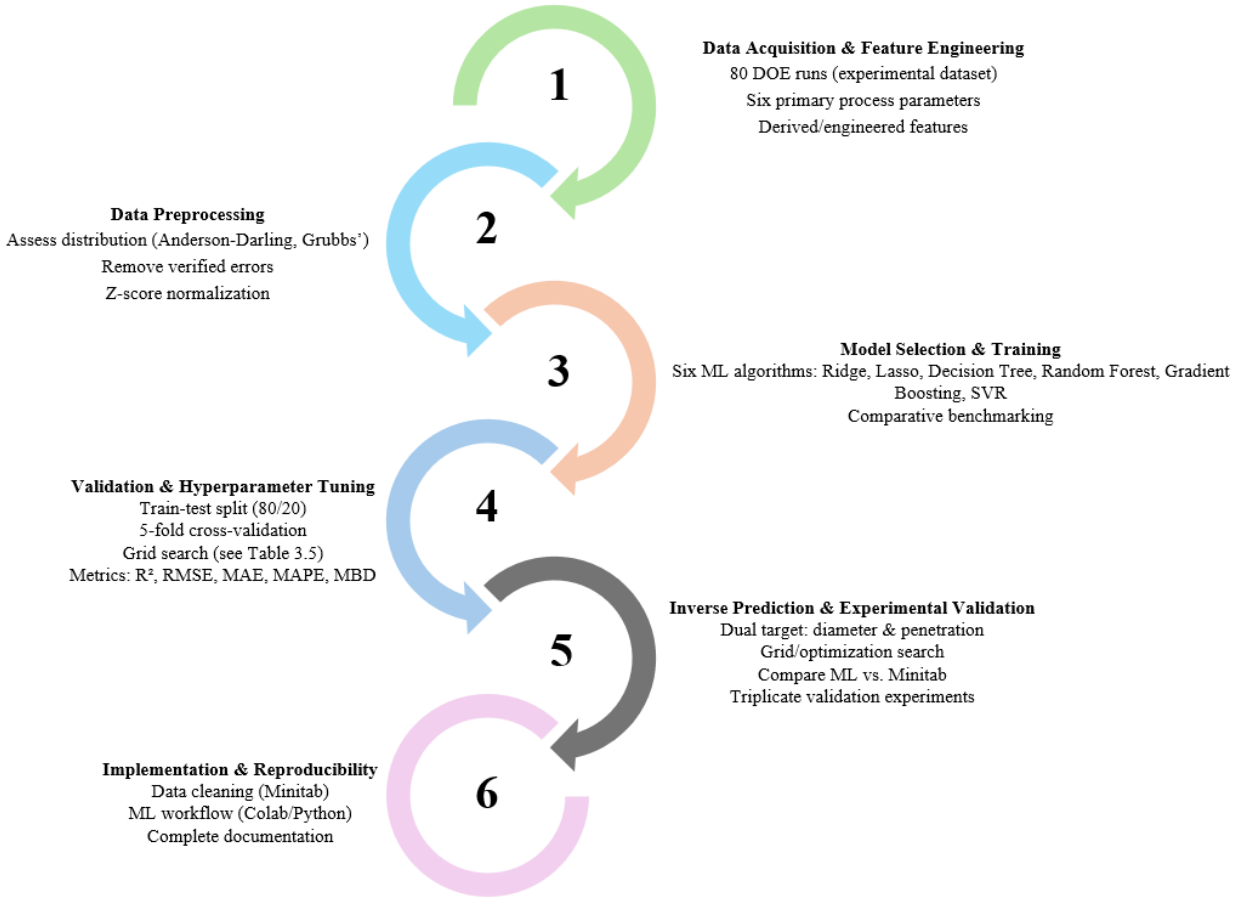


Figure 3.4. ML model benchmarking process flowchart

4. Re-evaluating RSW Acceptance Criteria: Strength Performance in Dissimilar High Stacking Ratio Joints with Inadequate Nugget Penetration

4.1 Overview

This chapter assesses the effectiveness of AWS D8.1 nugget penetration guidelines in HSR joints made of AHSS. The ANOVA analyses explore how six process parameters influence nugget growth across 80 distinct welding conditions, supported by cross-sectional and interrupted weld studies. Through TSS and CTS welded joints with and without visible penetration into thin sheet are then evaluated, SEM analyses on mechanically tested samples highlights additional bonding mechanisms, including solid-state diffusion and localized brazing, that contribute to joint strength.

4.2 Effect of RSW process parameters on nugget growth

Weld nugget penetration into the top sheet was measured for all welds in the design matrix to serve as the primary response variable. The data was then analyzed using an ANOVA methodology to identify the process parameters that most significantly influencing nugget growth. The model incorporated linear, quadratic, and two-way interaction terms, capturing both main effects and interactions among variables. The overall model had statistical significance, having an F-value of 3.67 and $p < 0.001$, see Table 4.1. In Table 4.1, DF denotes degrees of freedom, Adj SS represents the adjusted sum of squares, and Adj MS refers to the adjusted mean square, calculated as Adj SS divided by DF. The significance magnitude showed that weld time ($F = 10.61$) and hold time ($F = 10.84$) had a larger impact on nugget penetration, followed by current ($F = 8.93$). The significance of hold time did not mean that nugget growth continued, but it still had an overall effect on nugget quality through solidification. The applied electrode force during hold time influences how the semi-solid nugget solidifies under pressure to prevent void formation and maintain mechanical properties. Cooling time was not a statistically significant main effect ($p = 0.214$), but several of the significant interaction terms (force × cooling time, for example, and weld time × cooling time) included cooling time, suggesting a conditional effect of cooling time on nugget growth, depending on other parameter combinations [1, 156]. The model achieved an R-squared value of 62.93%, representing a moderate, but meaningful, explanation of variability in nugget penetration behavior across the DOE dataset. Notably, there was no statistically significant lack of fit ($p = 0.770$), indicating that the model adequately reflected the dominant trends in the data.

Table 4.1. Summary of ANOVA results for the influence of process parameters on diametric growth in RSW joints. The model includes linear, quadratic (square), and two-way interaction terms.

Model Summary					
S	R-sq				
0.10889	62.93%				
Analysis of Variance					
Source	DF	Adj SS	Adj MS	F-Value	P-Value
Model	25	1.087	0.043	3.670	0.001
Linear	8	0.271	0.034	2.860	0.010
Current	1	0.106	0.106	8.930	0.004
Force (kN)	1	0.070	0.070	5.900	0.019
Hold Time (ms)	1	0.129	0.129	10.840	0.002
Weld Time (ms)	1	0.126	0.126	10.610	0.002
Cool Time (ms)	1	0.019	0.019	1.580	0.214
Pulses	3	0.168	0.056	4.710	0.005
Square	1	0.139	0.139	11.690	0.001
Current*Current	1	0.139	0.139	11.690	0.001
2-Way Interaction	16	0.658	0.041	3.470	0.001
Current*Force (kN)	1	0.250	0.250	21.060	0.001
Current*Pulses	3	0.172	0.057	4.840	0.005
Force (kN)*Cool Time (ms)	1	0.135	0.135	11.390	0.001
Force (kN)*Pulses	3	0.117	0.039	3.290	0.028
Hold Time (ms)*Weld Time (ms)	1	0.113	0.113	9.540	0.003
Hold Time (ms)*Pulses	3	0.128	0.043	3.590	0.019
Weld Time (ms)*Cool Time (ms)	1	0.048	0.048	4.060	0.049
Weld Time (ms)*Pulses	3	0.116	0.039	3.260	0.029
Error	54	0.640	0.012		
Lack-of-Fit	48	0.544	0.011	0.717	0.770
Pure Error	6	0.096	0.016		
Total	79	1.727			

The welding current was identified a crucial factor in joining HSR joints, because it directly governed heat generation by the Joule heating relationship (Eq. 1). In HSR joints, the current is critical in overcoming the thermal resistance and providing sufficient heat to melt the thin-thick layer. Furthermore, the presence of a statistically significant second order term (current × current)

indicated a nonlinear relationship with nugget; that is, beyond a certain point, further increases in current did not proportionally increase nugget penetration, and resulted negatively, such expulsion, voids, and excess electrode indentation, all of which are bad for weld quality and integrity of the nugget [52, 160, 161]. Conversely, insufficient current resulted in inadequate heat generation, leading to incomplete fusion, particularly at the upper interface. These observations were consistent with the findings of Nielsen et al. [116], who found current had the greatest influence on nugget diameter and penetration in three-sheet AHSS joined together, and Pouranvari *et al.* [157] identified current as the primary control parameter for heat generation and weld nugget morphology.

The ANOVA results also confirmed that electrode force was statistically significant ($p = 0.019$), highlighting the dual role in facilitating effective heat dissipation and maintaining proper alignment of the welded materials during the process. Higher force improved sheet-sheet and sheet to electrode contact, thereby reducing locally generated heat. However, for HSR joints, adequate electrode force was important to provide consistent contact and to eliminate air gaps at the interfacial regions, which would otherwise hinder nugget penetration into the top sheet. Low force increased contact resistance at the faying interface, resulting in an accumulation of heat and faster nugget growth, while also increasing the chance of expulsion, surface arcing, and the formation of defects. Conversely, higher force reduced heating at the interface and creating conditions that constrained nugget growth in response to the compelled pressure exerted through the force [10]. The interaction of current and force was also highly significant ($F = 21.06$, $p < 0$). For instance, low force and high current, increased local heating due to high contact resistance, enabling deeper penetration into the top sheet but at the cost of process stability. Conversely, high force and low current reduced the concentration of heat in the nugget zone therefore slowing nugget formation, potentially leading to welds that were too small [113].

Weld time, governing the duration of current application, was significant both as a main effect and for interactions terms. The interaction between weld time and hold time was significant ($F = 9.54$, $p = 0.003$), indicating that a proper balance between heat input and post-weld pressure was essential for stabilizing the molten nugget during cooling and solidification [1, 156, 158, 159].

Although, cooling time didn't have significant as main effect ($p = 0.214$), its interaction with electrode force was highly significant ($F = 15.76$, $p < 0.001$). At higher electrode forces with shorter interpulse cooling times helped maintain contact, suppressed voids formation and promoted uniform nugget growth. In contrast, lower forces with longer interpulse cooling times facilitated more gradual heat dissipation and controlled solidification, which tended to slow the rate of nugget through-thickness growth but reduced the risk of excessive nugget expansion or defect formation. These findings underscored the importance of synchronized thermal and mechanical control, especially in HSR joints where heat dissipation and contact conditions at the interfaces varied [162].

The number of pulses was also found to be statistical significance ($p = 0.005$), though its significance was modest relative to the influence of current and weld time, indicating that number of pulses was a secondary, yet noteworthy, influence on nugget growth. In HSR joints, multi-pulse schedules were proved beneficial as they address the thermal imbalance between thick and thin sheets by reintroducing heat after cooling intervals, thus facilitating upward nugget growth. The influence of pulse count was found to be conditional rather than absolute, as indicated by its significant interaction effects, including force × pulses, weld time × pulses, and hold time × pulses, all of which were statistically significant in the ANOVA results. The interactions indicated that the number of pulses used significantly influenced the evolution of heat and pressure throughout the weld cycle. Higher number of pulses may cause increased electrode wear, grain coarsening, or localized thermal fatigue [4]. These findings are consistent with previous studies [17, 118, 160], which associated multi-pulse welding with improved toughness and grain refinement in AHSS joints.

Overall, nugget growth was not driven by single factor in RSW process, but rather by a complex interplay of process variables and their interactions. Primary factors like current, force, weld time, hold time, and number of pulses exerted strong effects, while their impact was further influenced by supporting variables including hold time, cool time, and number of pulses. These findings agree with earlier research [17, 87, 121], highlighting the importance of a balanced process window that integrates heat input, pressure application, and cooling dynamics to ensure optimal weld quality.

4.3 As-welded microstructures

To assess the effect of welding process parameters on nugget formation in high stacking ratio resistance spot welding, four representative cross-sectional welds were examined, each with a different combination of current, electrode force, weld time, hold time, number of pulses, and cooling time. Figure 4.1(a) shows that a low current (7.3 kA), long pulse time (165 ms), moderate force (4.35 kN), and two pulses resulted in insufficient heat input, restricting nugget formation to the thick-thick interface and no penetration into the upper thin sheet. Figure 4.1(b), used a greater current (8.5 kA), three pulses, and a higher force (5.4 kN), resulting in larger nugget. However, the nugget did not penetrate the thin–thick, likely due to reduced contact resistance from the excessive force. In Figure 4(c), four pulses, moderate current (8.02 kA), force (4.05 kN), extended weld time (200 ms), and medium interpulse cooling time produced a well-formed, symmetric nugget with 31% penetration into the top thin sheet. Finally, in Figure 4.1(d), although five pulses and the highest current (9.25 kA) promoted broad nugget growth, the lowest force (3.3 kN) and shortest cooling time led to an asymmetric and irregular nugget boundary, likely due to excessive thermal input combined with limited mechanical restraint. These results highlight how fine-tuning the six parameters optimized heat distribution, interfacial melting, and nugget morphology in multi-material joints.

The four-pulse weld illustrated in Figure 4.1(c) referred to as NP, was chosen for further microstructural examination as shown in Figure 4.2 which include an optical macrograph of the welded joint along with high-magnification micrographs of selected regions. The FZ, HAZ, and BM is distinctly visible. The weld nugget had a symmetric, elliptical profile and a well-defined fusion boundary, as indicated by the white dashed lines in Figure 4.2(a), and it had no observable cracks or voids signifying a sound weld formation. Metallographic observations of the weld cross-section confirmed that the weld nugget penetrated approximately 31% into the upper thin sheet, surpassing the minimum requirement of 20% as specified by AWS D8.1 [70]. Nugget penetration was measured relative to the thin–thick interface, with the interface width determined to be 4.56 mm. The maximum nugget width was observed near the thick–thick interface, measuring 7.75 mm, which also exceeds the dimensional criteria typically associated with sound welds in three-sheet stack-ups. These results indicate that the applied multi-pulse welding schedule was effective in promoting uniform heat distribution and balanced nugget growth across all interfaces.

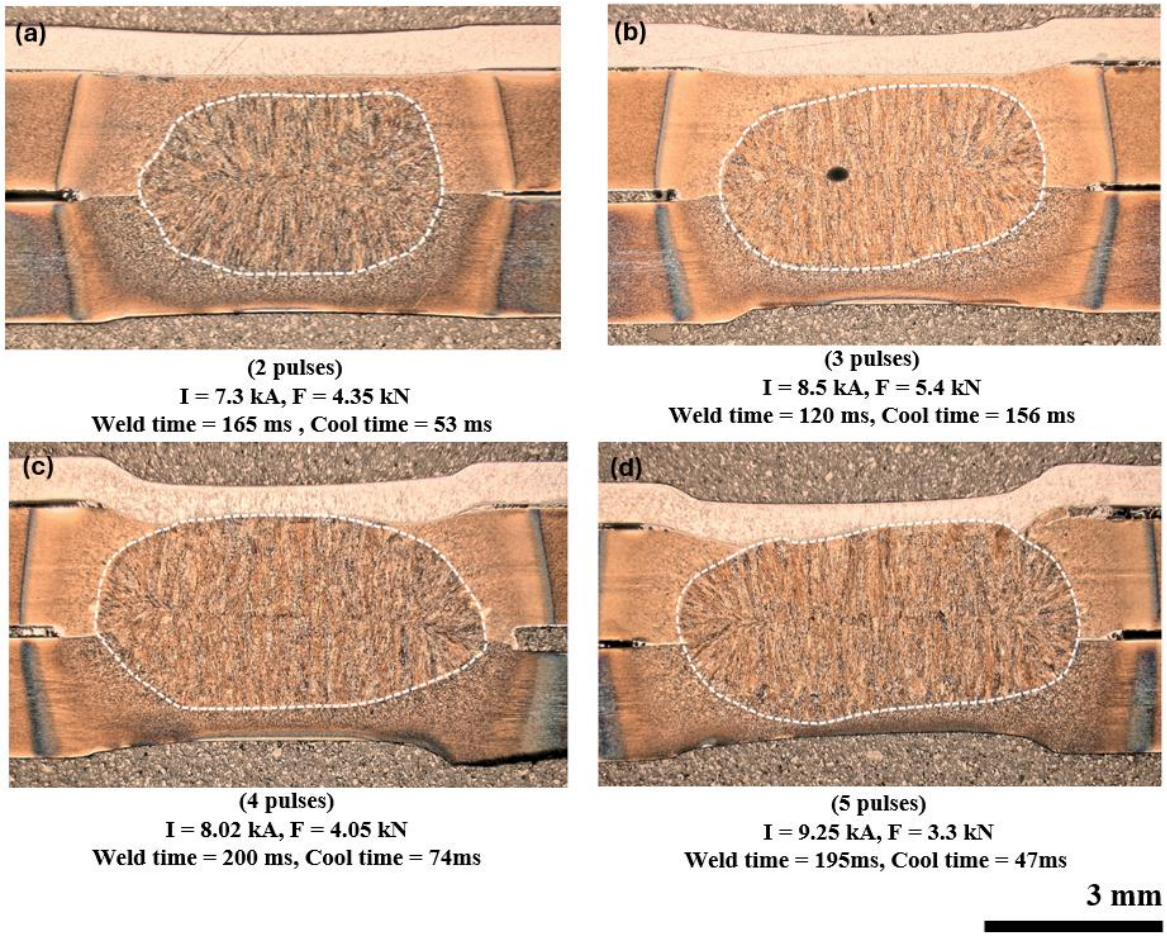


Figure 4.1. Cross-sections of weld nuggets under varying RSW conditions. Each condition involved changes in current, force, weld time, hold time, pulses, and cooling time. Nugget growth progressively increased from (a) to (d) with higher thermal input, with optimal morphology observed in (c). White dashed lines indicate fusion zone boundaries

Based on the OM and SEM images from Figure 4.2(a) and (c), the FZ is consists of fully martensitic coarse-grained microstructure. Multi-pulse welding facilitated by rapid heating and cooling cycles promotes dendritic martensitic transformation in FZ as this region experienced the highest peak temperature. The resulting microstructure predominantly comprises lath martensite with varying lath widths and orientations due to localized changes in alloy composition and temperature gradients during solidification. The SEM micrographs in Figure 4.2(b), (d), and (e) represent the HAZ of each material in a welded dissimilar joint, marked with red dashed boxes in Figure 4.2(a).

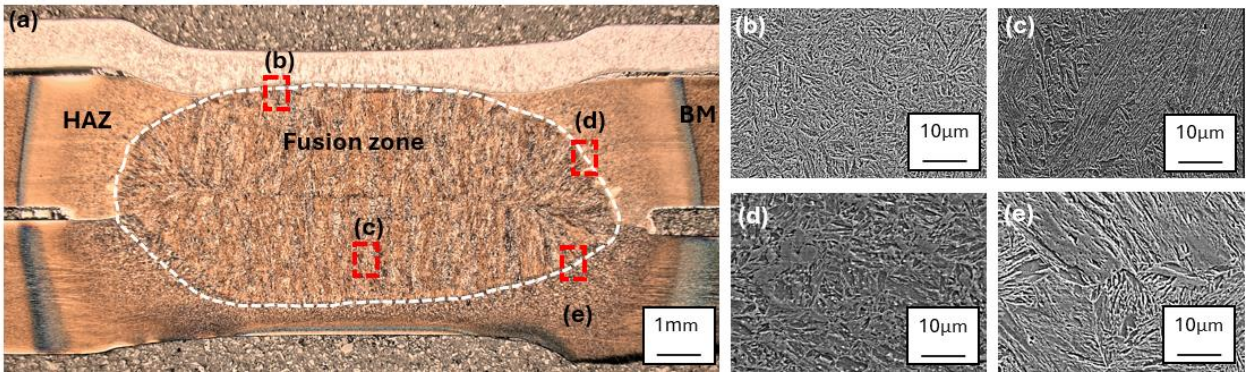


Figure 4.2. a) Optical macrograph of the welded cross-section of weld condition NP with nugget growth into top thin sheet - showing FZ, HAZ, and BM. Optical macrograph and corresponding microstructural analysis of the weld nugget region. (b–e) SEM micrographs at 1000× magnification highlighting the microstructural evolution in the HAZ of the top, middle, and bottom sheets, respectively

Surrounding the FZ is HAZ, where the maximum temperature during welding was just below the melting temperature. The heat in this area was sufficient to alter the microstructure without causing melting and HAZ can be further divided into fine grain HAZ (FGHAZ), coarse grain HAZ (CGHAZ), Intercritical HAZ (ICHAZ) and sub-critical HAZ (SCHAZ). In the SCHAZ, tempering can occur, leading to localized softening. These changes may slightly weaken the joint strength below that of the base material [36]. The base material stayed unchanged because it was not exposed to sufficient heat during welding.

Figure 4.2(b) depicts the HAZ of the top thin sheet shows the ferrite grain coarsening consistent with exposure below the Ac_1 temperature (subcritical heating) is observed. In this region, no transformation to austenite occurred because the water-cooled electrode rapidly extracted heat, resulting in a high cooling rate and limiting thermal exposure. In contrast, the HAZ exhibited a tempered martensitic microstructure, formed due to peak temperatures during welding ranging from Ac_1 temperature to <200°C. Because the middle sheet was not in direct contact with either electrode and had higher electrical resistance, it retained heat for a longer period, promoting tempering of martensite and carbide precipitation. In the bottom sheet, the HAZ consisted of tempered martensite, and the direct contact with the lower electrode accelerated cooling compared to the middle sheet.

Changes in microstructure across various subregions of the welded joint directly contributed to the observed differences in local hardness. Figure 4.3 shows the Vickers microhardness distribution of condition NP welded cross section, covering all regions shows in Figure 5(a-e). The profile captures a diagonal traverse from the top sheet to the bottom sheet, as indicated by the inset macrograph. The average hardness of BM was 125 $\pm$ 2.7 HV, 525 $\pm$ 11.0 HV, and 350 $\pm$ 14.4 HV for DDQ270, PHS2000 and 1G-1180, respectively where FZ showed 525 $\pm$ 11.0 HV. From the top sheet to the FZ, hardness increased sharply from approximately 150 HV, characteristic of the ferritic–bainitic microstructure in the DDQ270 sheet's CGHAZ, to about 500 HV at the FZ boundary, reflecting the transition to a fully martensitic microstructure formed by rapid cooling. Moving from the FZ into the HAZ regions of the PHS2000 and 1G-1180 sheets, hardness in the upper critical HAZ (UCHAZ) was also elevated compared to their respective base metals, primarily due to phase transformations induced by the welding thermal cycle and the high cooling rates inherent to resistance spot welding.

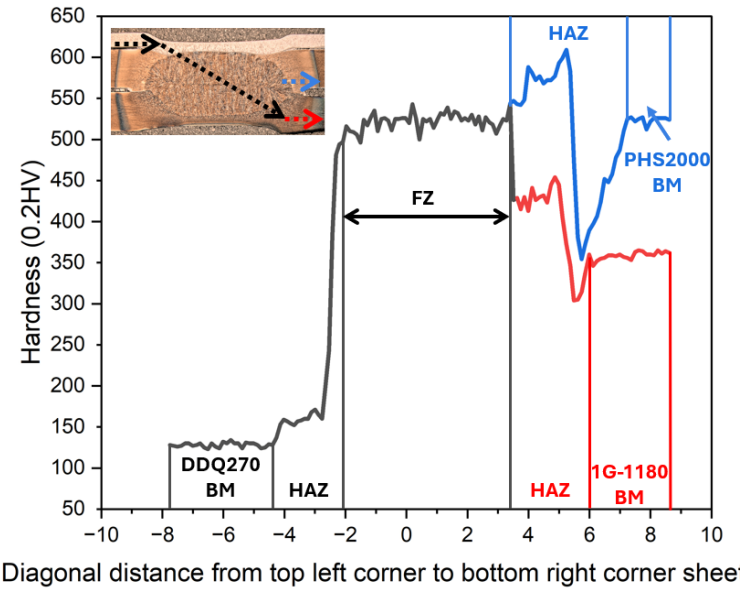


Figure 4.3. Microhardness profile measured from the top sheet through the middle and bottom sheets along the weld cross-section. The inset shows the approximate hardness measurement path across the nugget and HAZ for each sheet

Following the UCHAZ region, the hardness of the PHS2000 and 1G-1180 dropped significantly, highlighting the SCHAZ region. In this region, the martensite within the BM was tempered during welding, reducing local hardness, often referred to as HAZ softening. However, the magnitude of

softening differs between the two materials due to their distinct initial microstructures. With an approximate 33% decrease in hardness within the SCHAZ, softening is more noticeable in the PHS2000. This is because of martensite tempering and potential carbide precipitation. In contrast, the 1G-1180 showed a less noticeable drop in hardness of about 6%.

4.4 Interrupted Welds

In HSR joints, heat loss occurred more rapidly from the thin sheet material, whereas heat retention was greater within the regions containing thicker sheet materials [161]. A single welding pulse often cannot generate sufficient, uniform fusion across all interfaces without risking expulsion or inadequate penetration [17]. To address this, multipulse welding schedules were used to enable sequential and controlled heat input, allowing for more uniform nugget growth through all interfaces. Both NNP and NP conditions were evaluated using a 4-pulse schedule as shown in Table 3.4: NP achieved penetration into the top sheet, while NNP did not, enabling a direct comparison of nugget evolution and bonding mechanisms.

For interrupted testing, welding experiments made using progressively longer weld times so that several welds were made using increasing number of pulses, increasing weld time by 200 ms in this case. Cross-sections of these welds, which may be seen in in Figure 4.4. In both NNP and NP the first pulse resulted in melting formation at the thick–thick interface; a small weld nugget was observed near the center of the interface, shown in Figures Figure 4.4(a–b). At this stage, no nugget penetrated the top sheet. After two pulses (400 ms total weld time), the nugget diameter increased in both conditions at thick-thick interface as shown in Figure 4.4(c-d). In NP, the fusion zone expanded symmetrically with early signs of metallurgical bonding extending to the top thin sheet interface. However, in NNP the nugget mostly developed in the center or thick-thick interface. After three pulses (totaling 600 ms of weld time), the NP condition showed evident nugget penetration into the top sheet, achieving complete fusion across all three sheets, as illustrated in Figure 4.4(f). The NNP condition demonstrated nugget growth limited to the middle and bottom sheets, with no visible penetration into the top sheet (Figure 4.4(e)). After the completion of four pulses (800 ms total weld time), NP continued to show complete nugget penetration into the top sheet as shown in Figure 4.4(h). This progressive nugget growth indicates that incremental heat accumulation across pulses enables fusion at the upper interface, overcoming the resistance of the

coated outer sheet. In contrast, Condition NNP through Figure 4.4(h) continued to show no evidence of nugget penetration into the top sheet despite the equivalent total weld time.

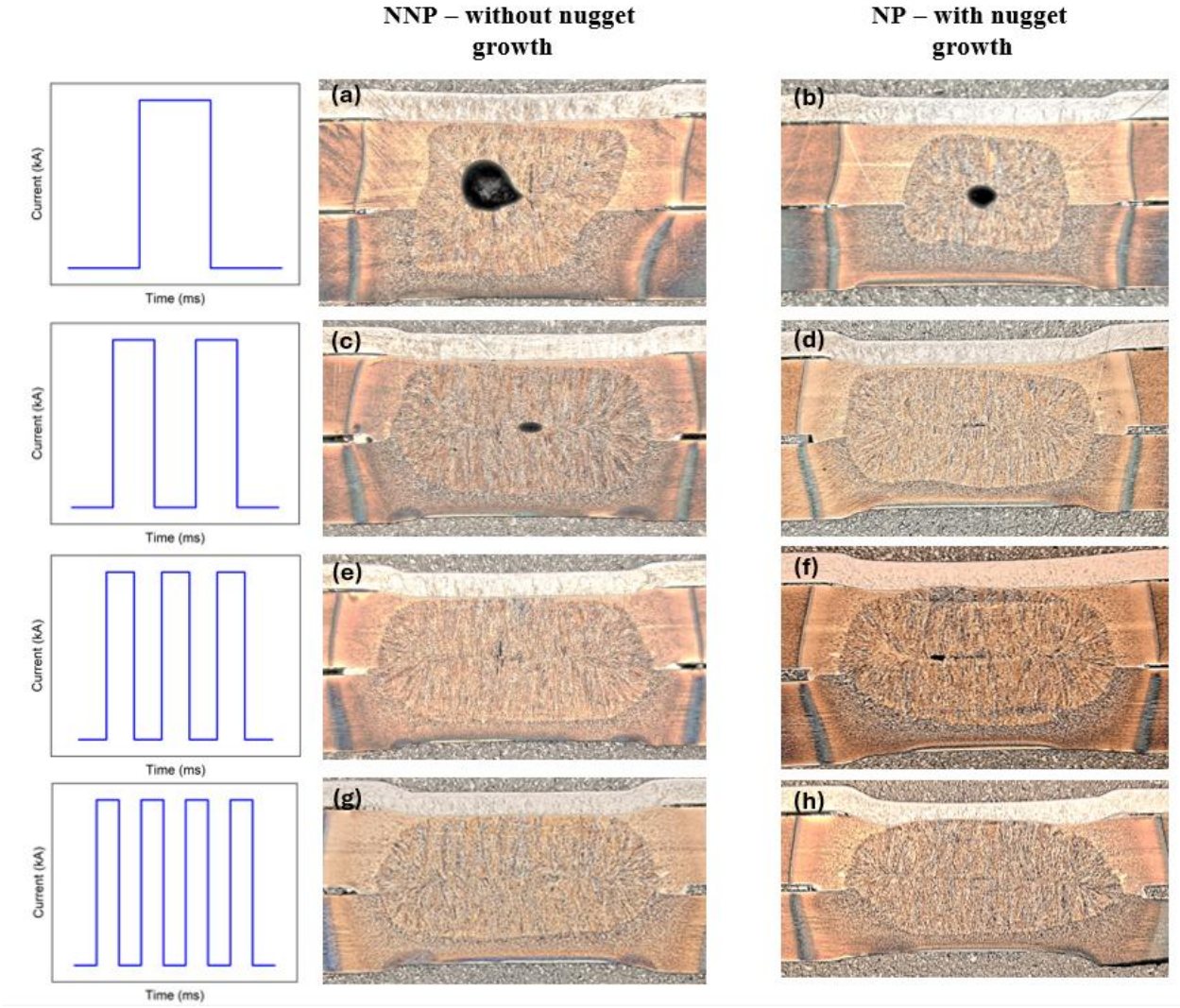


Figure 4.4. Cross-sections of interrupted welds comparing weld nugget formation using multipulse schedules for NNP (a, c, e, g – without nugget growth into thin sheet) and NP (b, d, f, h – with nugget growth into thin sheet). Corresponding pulses weld schedule are shown to the left of each row. Nugget penetration into the top sheet is observed in NP, demonstrating the effect of pulse configuration on weld development in three-sheet stack-ups

The maximum nugget width (thick-thick interface) and nugget height for both conditions NNP and NP were measured after each interrupted test, which are shown in Figure 4.5. For both NNP and NP, a rapid increase in nugget width occurred during the first and second pulses. However, at a

total weld time of 600 ms (after three pulses) there are observable differences in the growth trends. For NP, the maximum nugget width sharply increases until it reaches approximately 6.5 mm after 600 ms, then it continued to increase gradually up to 7.2 mm close to 1600 ms (final weld). NNP also followed the same trend and experienced the maximum nugget width after 600 ms, and then gradually increased later. Both conditions had very similar diametric nugget grow, due to the same heat input over a 4-pulse weld schedule. Nugget height (measured in the through-thickness direction) followed a distinctly slower growth for both conditions compared to horizontal growth. Initially NNP showed good nugget height but after the 3rd pulse, the NP weld had a marginally greater nugget height of 3.5 mm at the end of the welding sequence compared to 3.0 mm for NNP. The NNP welds restricted vertical growth suggests that there was not enough heat input to accomplish full fusion through the joint's thickness. The welding conditions for NNP led to overall restricted nugget formation in both lateral and vertical directions and this could be due to faster heat extraction by the water-cooled electrodes and the lower current, the nugget was unable to grow through the thin sheet.

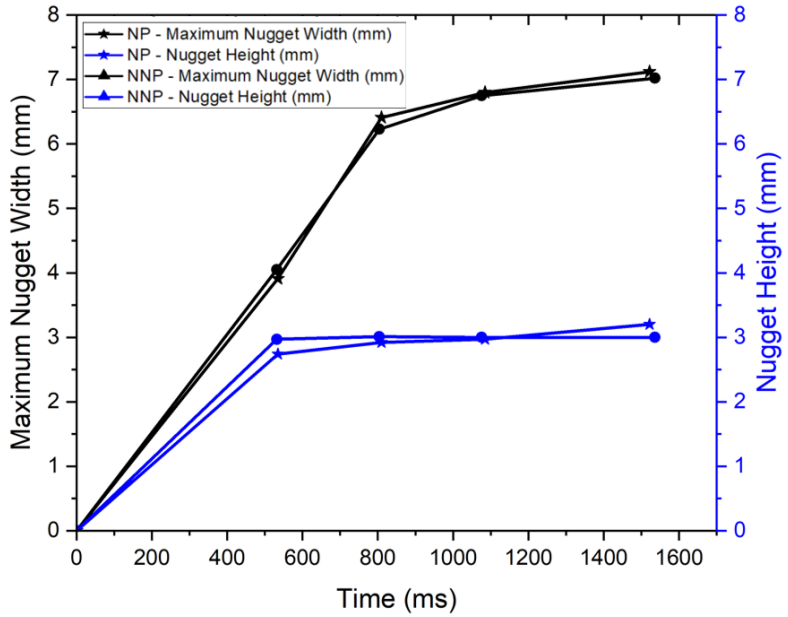


Figure 4.5. Showing maximum nugget width and nugget height as a function of weld time for NNP and NP weld conditions

4.5 Mechanical Strength Analysis

Welds in the NP and NNP conditions were tested in TSS and CTS configurations. The TSS and CTS load–displacement curves are shown in Figure 4.6(a) and (b), respectively, and the average peak load values are shown in Figure 4.6(c). In Figure 4.6(a–b) a red dashed line was added to indicate the minimum required joint strength specified by ISO 14373:2024 [162].

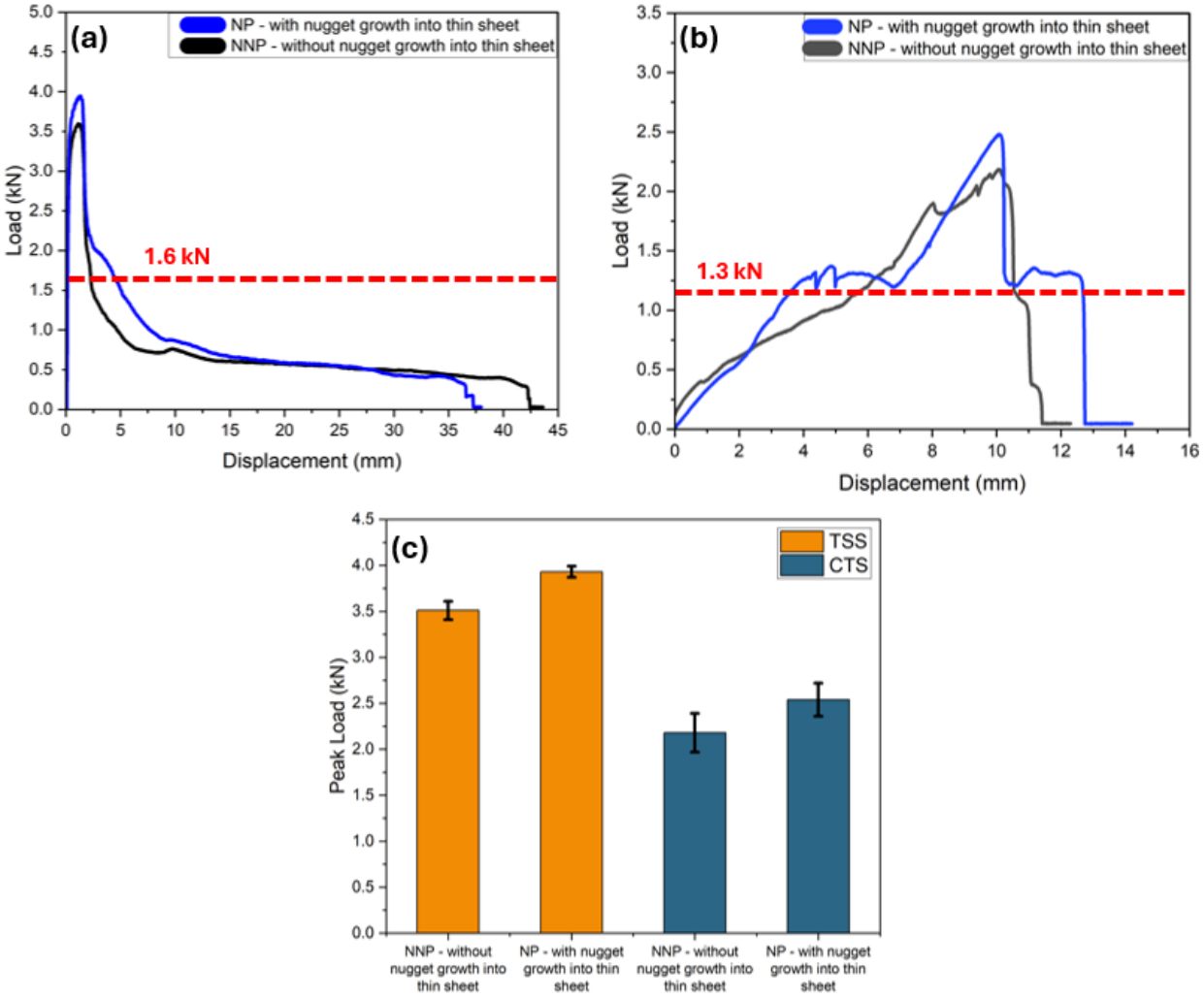


Figure 4.6. Mechanical performance evaluation of four weld conditions (a) TSS load displacement curves, (b) CTT load displacement curves, and (c) bar chart summarizing the peak loads of TSS and CTS. The red dashed line indicates the minimum load threshold

When loaded, both NNP and NP showed an initial elastic response followed by yield at peak load in the TSS, whereas in CTS loading was accompanied by pronounced plastic deformation prior to

reaching peak load. In both test types, fracture was preceded by a progressive load drop following peak load, as illustrated in Figure 4.6(a-b). In TSS, Condition NP showed the higher peak load (4.0 kN) and was capable greater displacement (42.0 mm) at fracture, indicating both significant strength and ductility. The high ductility was attributed to the top sheet's (DDQ270) soft and highly formable nature. During shear loading, the joint failed by tearing through the base metal of the top sheet, exhibiting extensive plastic deformation in the HAZ. This resulted in a tailing effect that allowed for greater displacement and enhanced energy absorption. The NNP welds exhibited lower strength than the NP weld in TSS, having a peak strength of 3.6 kN. The lower strength was attributed to lack off penetration at thin-thick interface. However, it should be noted that regardless of top sheet penetration, both conditions surpassed the minimum required peak load threshold for TSS strength.

As shown in Figure 4.6(b), during CTS loading, both weld conditions demonstrated sudden drops in the load-displacement curve at various points throughout the test. These abrupt decreases may be attributed to localized failure at regions with insufficient nugget penetration or microstructural variations around the weld, both of which can lead to inconsistent bonding strength at the interface [39–41]. As the applied load increased, these weaker areas failed preferentially, resulting in fluctuations in the force–displacement response. The NP condition outperformed the NNP condition, with a higher peak load (2.5 kN) and displacement (12.8 mm) before PPO failure, whereas NNP failed at approximately 2.09 kN. NP's higher CTS performance is primarily owing to increased nugget penetration into the top sheet, resulting in a bigger fused area and stronger metallurgical bonding across the interface. This larger bonded area improves load transfer and promotes more uniform stress distribution, lowering the risk of interfacial separation or failure under applied loads.

As illustrated in Figure 4.6(c), both NNP and NP exceeded all minimum strength requirements under tensile load bearing conditions; however, the NP welds demonstrated superior performance, with a peak tensile shear load of 4 kN, compared to 3.6 kN for NNP. This 11% increase in TSS of NP is due to nugget continuity which provided a larger effective load-bearing area and enhanced metallurgical bonding at the interfaces, resulting in greater joint strength. The CTS results for NP outperformed those of NNP, with a peak load of 2.4 kN compared to 1.9 kN for NNP, representing a 14% increase. It was seen that, in conditions without nugget penetration into top thin sheet NNP,

acceptable joint strength under TSS and CTS was achieved, indicating that nugget penetration is not singularly responsible for joint mechanical strength. Although nugget penetration into the top sheet was not seen for welds made in the NPP condition, it is suspected that their conforming joint strength was due to other bonding mechanisms, such as solid-state diffusion bonding or localized brazing [13, 17]. The conforming performance of the NPP welds highlights that that if only quality criteria in AWS D8.9 are used, welds with conforming mechanical properties may be rejected.

4.6 Failure Behaviour

To better understand the failure behavior and interfacial bonding of the selected weld conditions NNP and NP, 90% interrupted TSS and CTS tests were performed. The fractured cross-sections are illustrated in Figure 4.7; the blue arrows indicate the force application directions when testing. Figure 4.7(b) and (d) depict the cross-sectional view of interrupted specimen for both TSS and CTS tests for condition NP, where previous metallographic analysis confirmed that the nugget penetrated the top thin sheet during welding. Necking and local thinning were observed in the top base metal (IF steel) during tensile loading, which is most pronounced during TSS loading of NP, as shown in Figure 4.7(b). The appearance of a neck indicates that ductile failure occurred [68, 163]. It is commonly reported that ductile (PO/PPO) failure modes absorb more energy and are preferred over IF [52, 81, 154, 156]. The soft, ductile DDQ270 steel base allows for significant plastic deformation under shear stresses before final failure, as shown by the long unloading region of the welds in Figure 4.6(a-b). This behavior plays a significant role in the energy absorption capacity and ductility seen during testing.

Figure 4.7(a) and (c) show the fracture cross-sections for condition NNP, and the results showed that the top thin sheet never experienced nugget penetration. Instead, the top interface exhibits partial bonding, as indicated by localized adhesion and possibly diffusion bonding between the top and middle sheets. To understand the bonding mechanism, two sites along the top sheet interface, marked by the red dashed boxes in Figure 4.7(a), were analyzed using SEM. Figure 4.8 shows the SEM micrograph and accompanying EDS elemental maps for regions y and z from Figure 10(a). In region y, the thin-thick interface was consistent and uniform, as can be seen from Figure 4.8(a). There is no indication that a secondary phase or intermetallic layer developed. Fe, Al, Si, Zn, Mn, and O do not show abrupt elemental changes at the interface, indicating that bonds were created through solid-state diffusion process. This was also evident from the EDS profiles in Figure 4.8(c),

where no elemental gradients were identified over the scanned distance. The dominant Fe levels remain consistent, while the Al presence is uniform, suggesting that elemental interdiffusion rather than localized melting and solidification occurred. These characteristics align with diffusion bonding [116]. In comparison, region z shows strong evidence of localized brazing. The SEM image in Figure 4.8(d) shows a discrete interfacial layer, highlighted by two white dashed lines. The EDS maps reveal an area rich in Al at the interface, with a composition that is clearly different from that of its surrounding matrix, as shown in Figure 4.8(e). The intensity profiles clearly show a peak in Al concentration coupled with a minor drop in Fe intensity at the interface, consistent with a thin brazed layer illustrated in Figure 4.8(f). The localized presence of Al and minor Si and Zn segregation suggest a low-melting-point phase (formed from the coating elements or interfacial reactions) that aided partial melting and solidification, yielding a brazed joint between the sheets.

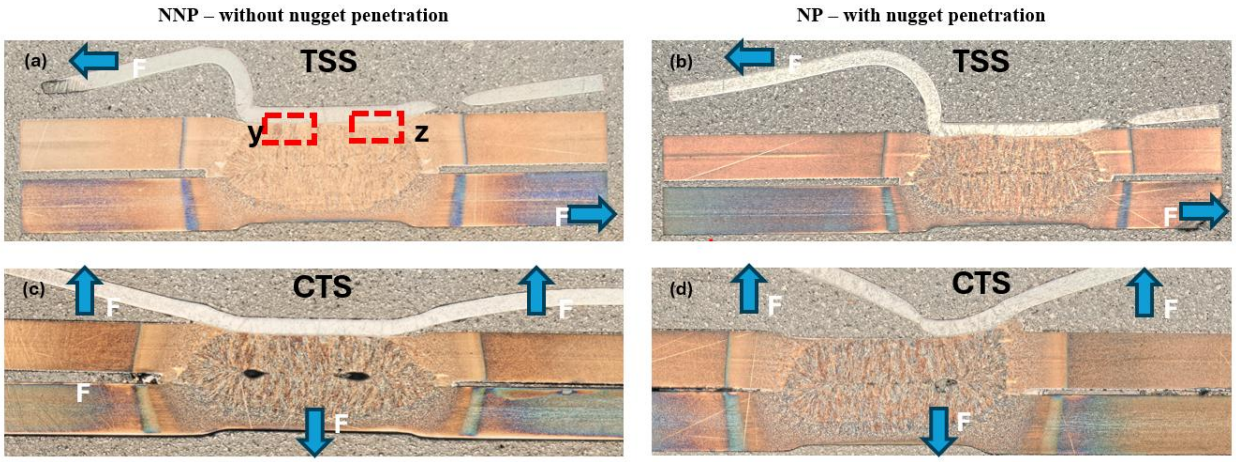


Figure 4.7. Fracture cross-sections of (a, c) condition NNP without nugget penetration, displaying partial bonding in the top sheet. (b,d) NP exhibiting nugget penetration into the top sheet, showing continuous partial fusion into top thin sheet. Red dashed boxes highlight regions along the faying interface selected for further investigation of potential diffusion bonding, brazing or incomplete fusion. Force directions (F) are indicated with blue arrows for both loading configurations

Welds made in the NNP condition had areas exhibiting diffusion bonding and localized brazing at the top sheet interface, in lieu of nugget penetration into the top sheet. Both the diffusion bonding and brazing mechanisms provided sufficient mechanical strength and crack resistance across the interface. These findings show that depending on nugget penetration as an indication of joint

quality is a conservative metric for determining conforming joints, although this metric has been the primary metric to determine weld quality for multi-sheet joints. Allowing interfacial bonding produced by diffusion, brazing, or some combination of these with nugget penetration would drastically widen the welding operational window for joints where it is difficult to grow the weld nugget into the top sheet. These observations indicate that current acceptance criteria should be re-evaluated so that the joint acceptance is based on performance metrics and the mechanisms that lead to joint strength. This would widen manufacturing lobes, increasing process robustness and allow for a wider variation of joint designs to be used in future automobiles.

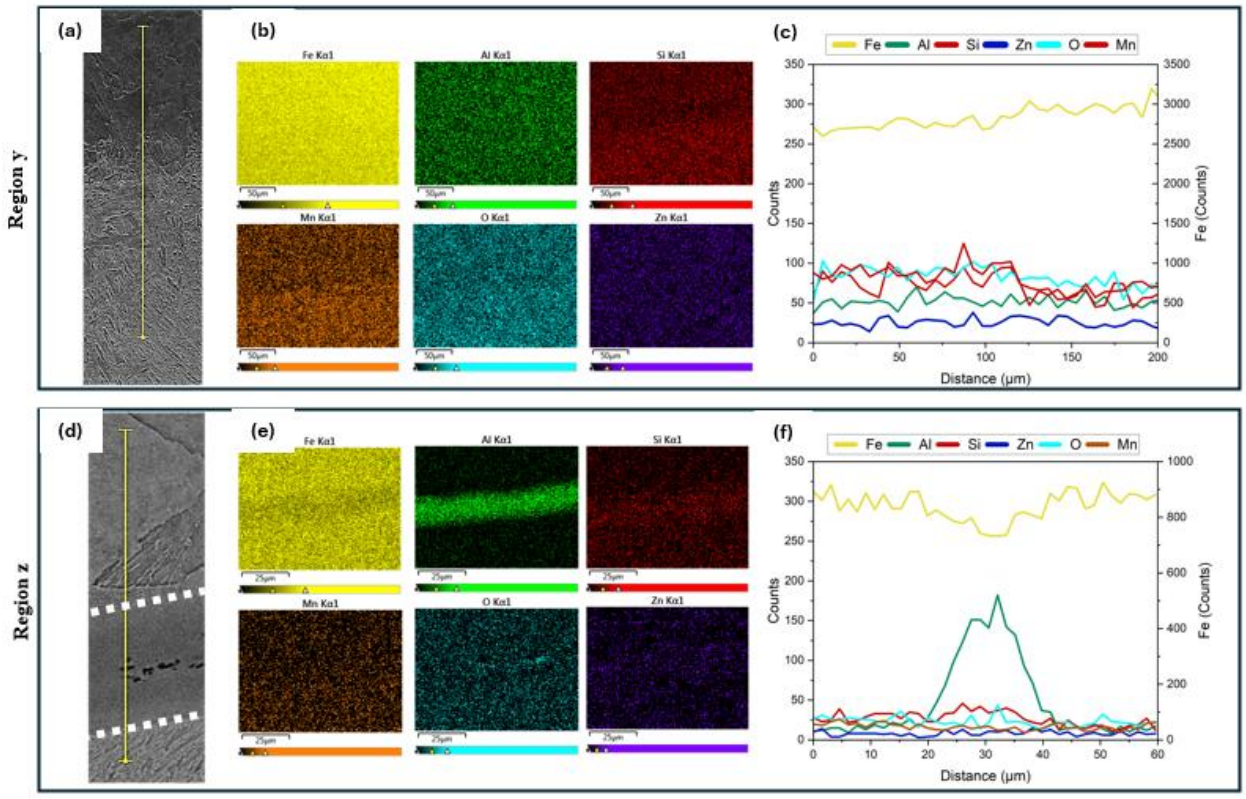


Figure 4.8. EDS line scan and elemental mapping of the joint interface at regions highlighted earlier by red boxes. (a-c) correspond to a region indicating solid state diffusion bonding, characterized by a uniform elemental distribution and absence of discrete intermetallic layers. The smoother profiles in (f) suggest stronger metallurgical continuity across the interface. (d-f) represent a region showing evidence of localized brazing, where a concentrated Al peak and sharp elemental gradients indicate limited interdiffusion and the presence of a thin interfacial or intermetallic layer

4.7 Summary

This chapter challenges the applicability of conventional AWS D8.1 guidelines for nugget penetration in RSW of HSR joints made of AHSS. The findings of systematic investigation demonstrated that joints with no visible nugget penetration into thin sheets produced mechanical performance that is equivalent to fully penetrated joints. The ANOVA analyses revealed that welding current, (F = 8.93), weld time (F = 10.61), and hold time (F = 10.84) were the influential parameters for nugget penetration into thin sheet. It also confirmed that electrode force was statistically significant (p = 0.019), highlighting the dual role in facilitating effective heat dissipation and maintaining proper alignment of the welded materials during the process.

Both NNP and NP exceeded all minimum strength requirements under TSS; however, the NP welds demonstrated superior performance, with a peak tensile shear load of 4 kN, compared to 3.6 kN for NNP. This 11% increase in TSS of NP is due to nugget continuity which provided a larger effective load-bearing area and enhanced metallurgical bonding at the interfaces, resulting in greater joint strength. The CTS results for NP outperformed those of NNP, with a peak load of 2.4 kN compared to 1.9 kN for NNP, representing a 14% increase. NP's higher CTS performance is primarily owing to increased nugget penetration into the top sheet, resulting in a bigger fused area and stronger metallurgical bonding across the interface. This larger bonded area improves load transfer and promotes more uniform stress distribution, lowering the risk of interfacial separation or failure under applied loads. Welds made in the NNP condition had areas exhibiting diffusion bonding and localized brazing at the top sheet interface, in lieu of nugget penetration into the top sheet as confirmed by SEM and EDS analysis. Both the diffusion bonding and brazing mechanisms provided sufficient mechanical strength and crack resistance across the interface. These results show that nugget penetration alone is too restrictive as a quality standard for multi-sheet joints. Acceptance criteria should instead reflect joint performance and the bonding mechanisms that provide strength, which would expand process windows and support more flexible, robust designs in future automotive applications.

5. Experimental Validation of Minitab and Machine Learning Models Inverse Predictions for RSW Weld Quality

This chapter covers the development and validation of six different supervised ML models used to predict nugget dimensions for dissimilar AHSS HSR welds, enabling accurate process optimization. It begins with data quality screening and feature correlation analysis to address multicollinearity and ensure reliability. The ML models are compared for predicting nugget width and penetration, with ensemble methods, and among all Gradient Boosting showed superior performance. SHAP analysis identified welding current and its interactions as key influences. The chapter concludes with experimental validation of inverse modeling to show that advanced ML approaches outperform traditional statistical methods in capturing, analyzing and predicting process parameters.

5.1 Normality and Outlier Assessment of Weld Nugget Measurements

The normal probability plots as shown in Figure 5.1(a-b) indicates that the maximum nugget width and nugget penetration data are normally distributed, as most of the points closely aligned to the reference diagonal line. This was verified by the results of the Anderson-Darling (AD) test, which yielded p-values of 0.262 for maximum nugget width and 0.581 for nugget penetration, both above the common cutoff of 0.05 for significance, thus failing to reject the null hypothesis of normality, indicating no significant evidence of non-normality in the data.

Minor deviations from the reference line were observed in the probability plots, especially in the tails of the distributions, due to measurement error and systematic parameter variation across the experimental design space. The normality assumption is based on the central limit theorem, where the measurement errors are assumed to be normally distributed. However, because data were taken across the entire parameter space, there are two effects comprising the overall distribution: (1) random measurement error (which can be assumed to be normally distributed) and (2) systematic response variations due to controlled parameter changes (which may not follow a normal distribution individually but are expected to be normally distributed across the design space).

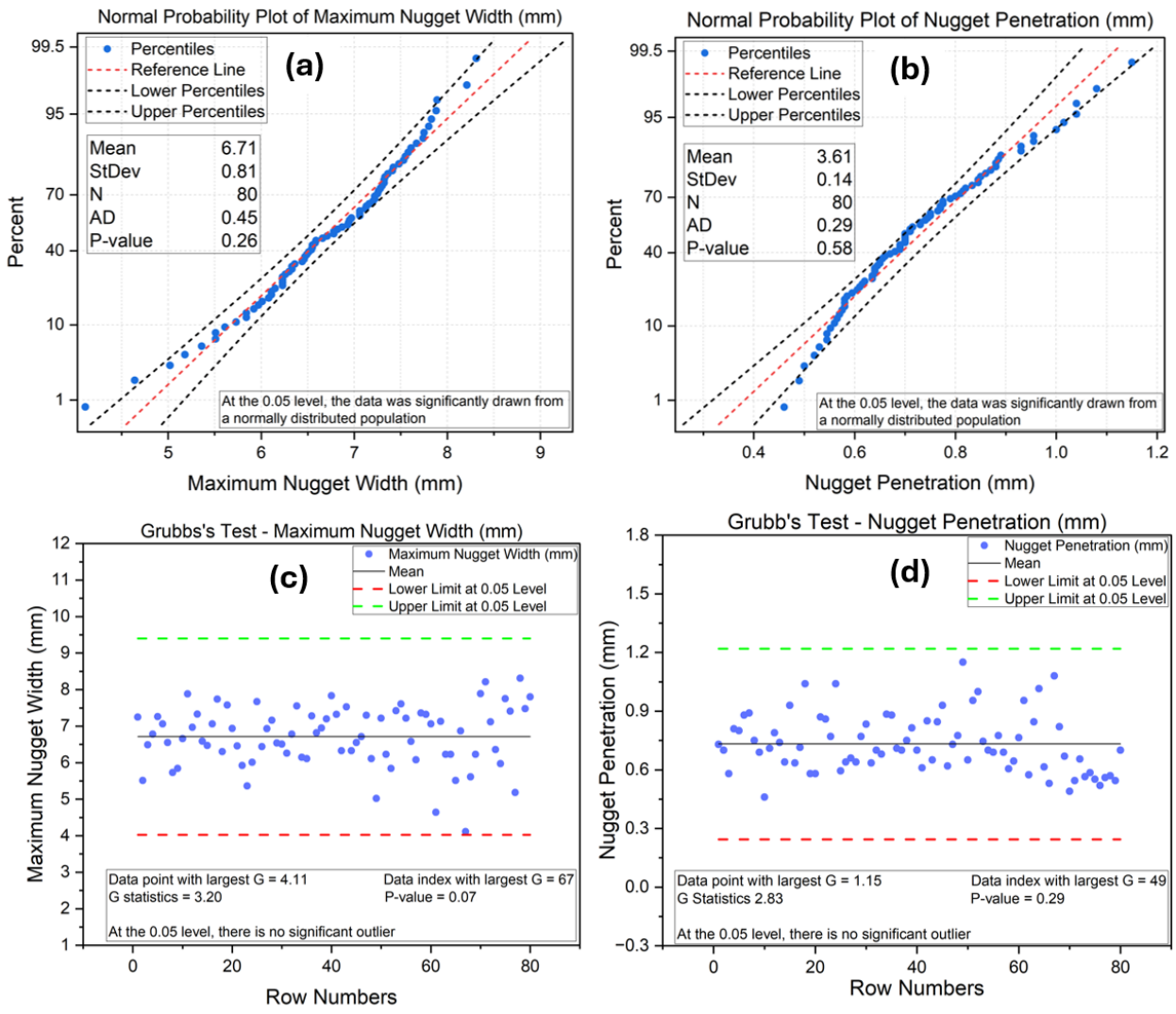


Figure 5.1. Summary of data quality for maximum nugget width and nugget penetration: (a, b) probability plots confirm near-normality, while (c, d) outlier plots reveal only a few atypical measurements across the dataset

Additionally, outlier detection using Grubbs' test as shown in Figure 5.1(c-d) revealed one or two possible outliers for maximum nugget width and nugget penetration. For the maximum nugget width, the Grubbs' test produced a p-value of 0.076 and for nugget penetration a p-value of 0.299, which were above the 0.05 threshold, indicating no statistically significant evidence of outliers in the datasets. However, the data points approaching the significance threshold suggest potential process variations that could be investigated further, such as electrode wear [65] or process instability, to ensure consistent welding performance. The overall data quality for maximum nugget width and nugget penetration was considered robust and appropriate for subsequent quality

control analysis. This method of characterizing and verifying data quality aligned with suggestions made in the advanced monitoring literature [141] where process data undergoes rigorous statistical verification prior to being used to develop predictive models and quality monitoring pipelines. Additionally, Chen *et al.* [164] and He *et al.* [135] emphasized that the use of robust assessment methods, with data-driven or ML models, added value in detecting atypical behavior and establishing appropriate process data quality for quality predictions in downstream applications.

5.2 Feature Correlation Analysis for Resistance Spot Welding Parameters

Understanding parameter correlations is important for ML model development because high correlation between parameters can produce multicollinearity, which could make models unstable and reduced interpretability. However, the decision to retain or remove correlated features must balance statistical concerns against predictive performance in practical applications. The correlation heatmap (Figure 5.2) revealed how various welding process variables and engineered features varied in relation to each other during RSW. Notably, each variable demonstrated perfect correlation with its squared term such as Current and Current², or Force and Force² ($r = 1.00$). This was expected and helped confirm the consistency of the data. The correlation analysis identified several parameters with strong interdependencies that could affect model interpretation. Force exhibited strong negative correlations with multiple timing parameters: Hold Time ($r = –0.80$), Cool Time ($r = –0.70$), and Weld Time ($r = –0.52$). This pattern indicates that the effects of force and timing parameters may be confounded in predictive models, as force variations are systematically linked to temporal welding parameters. From a practical perspective, higher electrode force enables more efficient heat transfer, allowing shorter welding cycles. For modeling purposes, this systematic relationship complicates the isolation of individual parameter effects, requiring careful interpretation of model outputs [73, 165].

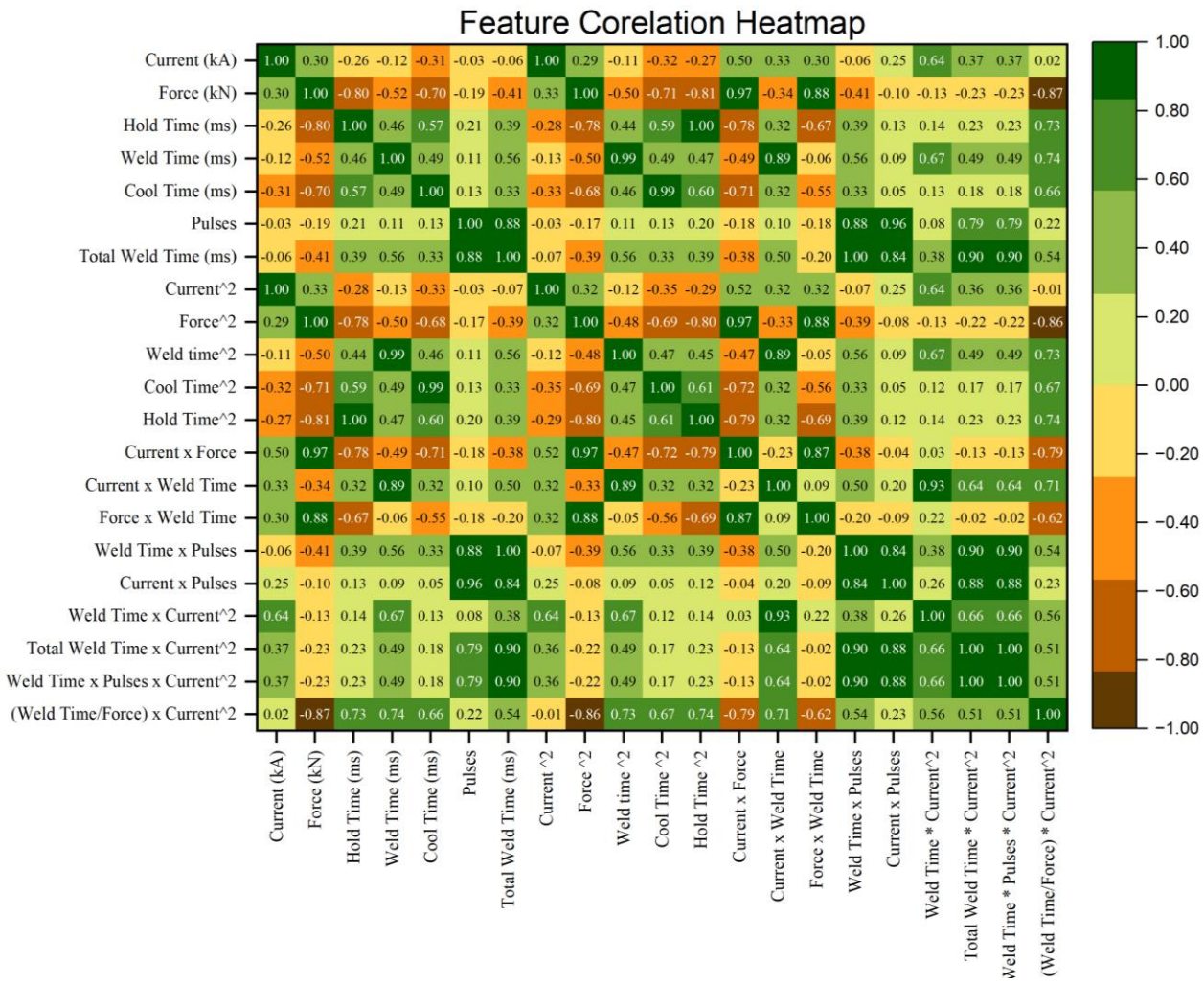


Figure 5.2. Correlation heatmap illustrating the relationships among process parameters and engineered features. Strong positive and negative correlations highlight key interactions and potential redundancies within the welding parameter set

Timing variables also demonstrated strong intercorrelations, with Pulses showing high correlation with Total Weld Time (r = 0.88) and moderate correlation with individual Weld Time (r = 0.56). These relationships arise because resistance welding controllers use predetermined schedules where pulse count, individual pulse duration, and total weld time are programmatically linked to maintain consistent energy input while enabling thermal management through controlled interpulse cooling intervals. This systematic programming creates inherent correlations that reflect real welding practice rather than random statistical relationships [135].

In contrast to the timing and force correlations, which demonstrated systematic welding practices, the interaction term Force×Current exhibited a different pattern of correlation. The interaction term was highly correlated with Force (r = 0.97) and weakly with current (r = 0.5), suggesting that the interaction term largely captured the effects of force alone rather than the true interaction between the two factors. Thus, at one time if Force×Current was to use for ML model as a predictor a careful attention was warranted regarding redundancy with Force, but less with Current. This redundancy, known as multicollinearity, posed an issue in modeling when predictors were too similar especially in pairs of squared terms and their originals, or closely related timing features [121, 133]. The moderate correlation between Current and Force (r = 0.30) represents the design of the experiment where these parameters were varied largely independently, in contrast to standard welding practice where the one could be adjusted to offset other operator would increase the force to offset the lower current.

Overall, the heatmap showed that many engineered features overlapped with their original variables, particularly among timing and force parameters. The presence of highly correlated variables had the potential to destabilize ML algorithms and impact their interpretability. In this study, a preliminary feature reduction approach showed substantial decreases in model R^2 values when correlated features were removed. Therefore, all features were retained to maximize predictive performance. The ensemble methods employed were inherently robust to multicollinearity through their tree-based architectures and feature sampling, making them suitable for handling correlated feature sets without significant performance degradation [121, 135].

5.3 Comparative Performance Evaluation of Regression Models for Nugget Width Prediction

The comparative analysis of ML models as highlighted in Table 5.1 for predicting maximum nugget width showed substantial variation in predictive performance between algorithms. Gradient Boosting emerged as the most effective model with an R^2 of 0.9480 and RMSE of 0.1841. The MBD of <0.001also showed that the gradient boosting prediction were not biased. Random Forest (RF) model also performed very well, with an R^2 of 0.8337, an RMSE of 0.3294, with a MBD of 0.0024. Decision Tree regression yielded slightly lower performance (R^2 = 0.8083, RMSE = 0.3536, MAE = 0.2382, MAPE = 3.58%, MBD = 0.0000) but remained acceptable for predictive

purposes as the R^2 value exceeded 0.80, indicating the model explained over 80% of the variance in nugget width measurements.

Support Vector Regression (SVR) predicted moderate results with an R^2 of 0.6373. The MBD of 0.1139 indicated minimal systematic bias, statistical testing revealed this bias was not significant given the model's overall error magnitude. The linear models including Ridge Regression and Lasso Regression achieved R^2 values of 0.5845 and 0.4779 respectively, with correspondingly higher error metrics (MAPE exceeding 6%), indicating limited capability to capture the complex relationships governing nugget width formation.

Table 5.1. Performance metrics of various machine learning models for predicting maximum nugget width, showing R^2, RMSE, MAE, MAPE, and MBD for each method

Model	**Performance metrics**				
	R^2	**RMSE**	**MAE**	**MAPE**	**MBD**
Ridge Regression	0.5845	0.5206	0.4451	6.89%	<0.001
Lasso Regression	0.4779	0.5836	0.4811	7.58%	<0.001
Decision Tree	0.8083	0.3536	0.2382	3.58%	<0.001
Random Forest	0.8337	0.3294	0.2657	4.11%	0.0024
SVR	0.6373	0.4864	0.3545	5.72%	0.1139
Gradient Boosting	0.9480	0.1841	0.1156	1.75%	<0.001

This result confirmed the superiority of Gradient Boosting and Random Forest over linear and single tree approaches reflected their architectural advantages for this welding prediction task. The iterative error correction method behind Gradient Boosting allowed it to learn progressively complicated non-linear relationships between the process parameters and features. RF strength lay in its ensemble of decision trees with random feature sampling, which provided robustness against overfitting while capturing parameter interactions through multiple decision pathways. These ensemble architectures were found to be better than linear methods for RSW applications as welding processes are inherently non-linear.

5.4 Comparative Performance Evaluation of Regression Models for Nugget Penetration Prediction

Evaluation of ML models for predicting nugget penetration, shown in Table 5.2, reveal notable contrasts in predictive performance, underscoring the complexity of nonlinear penetration behavior in RSW. Among all ML models, Gradient Boosting clearly outperformed all other algorithms with an R^2 of 0.9025, explaining over 90% of the variation in nugget penetration. RF yielded strong results as well, achieving an R^2 of 0.7343, MAPE of 8.40% and negligible bias (MBD = 0.0013). The decision tree model achieved an R^2 of 0.6833. While decision trees were not as robust as ensemble methods, it was still capable of reasonable prediction accuracy and interpretability for exploratory or interpretable modeling [16].

SVR achieved moderate performance, with R^2 of 0.5020 and MBD of 0.0066, indicating limited suitability for highly non-linear prediction compared to ensemble approaches [16]. Linear models including Ridge Regression (R^2 = 0.3960) and Lasso Regression (R^2 = 0.3607) performed the weakest with elevated error rates (RMSE > 0.11, MAPE > 12%) and a limited capacity to account for the complex relationships in the data. However, both linear models exhibited statistical calibration with MBD <0.001, retaining potential utility for initial parameter screening despite poor overall predictive fit.

In comparison to nugget width prediction, all ML models exhibited slightly lower R^2 and higher error in predicting nugget penetration, indicating that penetration behavior is more challenging to predict due to the complex physics governing nugget growth through dissimilar material interfaces. The superior performance of ensemble methods, particularly Gradient Boosting, stemmed from their ability to model the non-linear threshold effects and parameter interactions that characterized nugget penetration in high stacking ratio joints. These findings demonstrated that advanced ensemble models were essential for effective nugget penetration prediction, while Random Forest and Decision Tree approaches served as valuable alternatives when interpretability and computational efficiency were prioritized over maximum accuracy, particularly in exploratory analysis or real-time manufacturing applications where understanding parameter influences was as important as prediction precision

Table 5.2. Performance metrics of various machine learning models for nugget penetration, showing R^2, RMSE, MAE, MAPE, and MBD for each method

Model	Performance metrics				
	R^2	**RMSE**	**MAE**	**MAPE**	**MBD**
Ridge Regression	0.3960	0.1152	0.0903	12.50%	<0.001
Lasso Regression	0.3607	0.1482	0.1192	16.72%	<0.001
Decision Tree	0.6833	0.0834	0.0569	7.94%	<0.001
Random Forest	0.7343	0.0764	0.0610	8.40%	0.0013
SVR	0.5020	0.1046	0.0898	12.75%	0.0066
Gradient Boosting	0.9025	0.0463	0.0324	4.56%	<0.001

5.5 Model Prediction Accuracy and Residual Analysis for Maximum Nugget Width

The comparison of Ridge Regression and Gradient Boosting models demonstrated the importance of algorithm selection for nugget width prediction, with Ridge Regression serving as a baseline to highlight the performance gains achievable through advanced ensemble methods for predicting maximum nugget width yielded clear differences in model competence, with crucial insights derived from both actual versus predicted plots and residual analyses as shown in Figure 5.3.

Ridge Regression, as shown in Figure 5.3(a) the actual versus predicted scatter plot, exhibited substantial scatter around the ideal diagonal, particularly in the mid-range of nugget widths (6.0–7.0 mm). The predictions clustered loosely, and many points deviated noticeably from the diagonal line, with several errors exceeding 0.5 mm as shown by the RMSE of 0.5206. This outcome indicated that the linear approach of Ridge Regression was inadequate for capturing the relationships governing nugget width formation. The spread and systematic deviation in predictions, especially in regions critical for quality control, where nugget widths between 6.0-7.5 mm represent the target range for automotive applications and deviations can compromise joint strength and crashworthiness requirements, confirmed the limitations of the model for precise manufacturing applications.

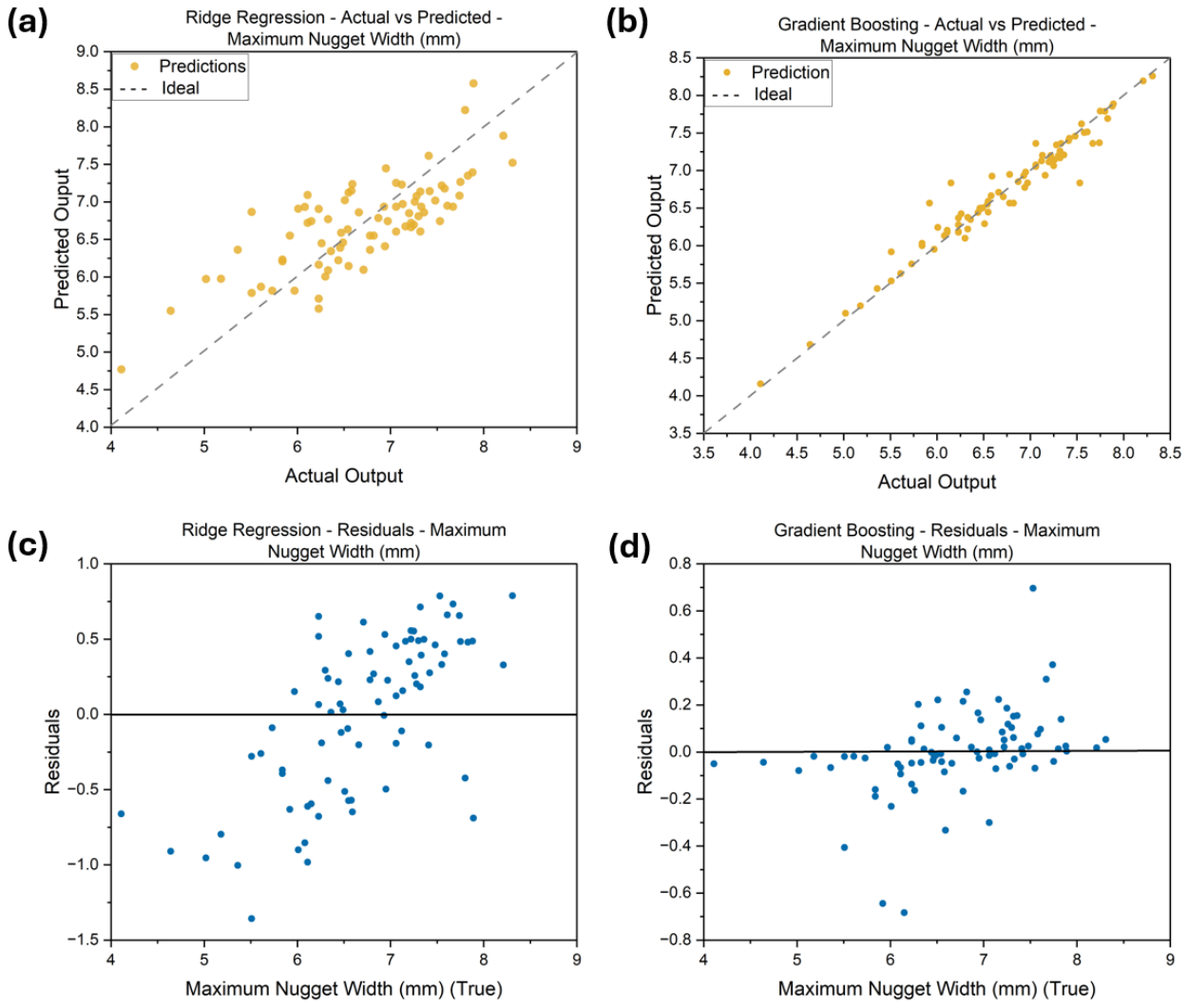


Figure 5.3. Comparison of Ridge Regression and Gradient Boosting models for maximum nugget width prediction: (a, b) Actual vs. predicted plots; (c, d) corresponding residual distributions.

In comparison to Pidge Regression performance, as shown in Figure 5.3(b) Gradient Boosting exhibited strong alignment between true and predicted values. Points densely overlapped the diagonal and exhibited minimal scatter across the entire range of measurement. This pattern indicated that the ensemble method successfully modeled the non-linearities and interaction effects inherent in resistance spot welding processes.

Residual analysis provided further evidence for these findings. Ridge Regression residuals (Figure 5.3(c)) exhibited specific pattern, with noticeable increase in variance at measured diameters greater than 6.5 mm, as well as systematic bias that ranged from approximately -0.2 mm at 6.0

mm diameter to +0.3 mm at 7.8 mm diameter. This heteroscedasticity violated the assumption of constant error variance and indicated that prediction errors were not consistent over the range of fitted values. Additionally, the residuals had a linear trend structure, which indicated that a non-linear relationship exist, which was not represented in the model. These systematic patterns suggested that the linear approach caused a model misspecification and obscured important relationships from the data. In contrast, the Gradient Boosting residuals (Figure 5.3(d)) revealed a randomly scattered distribution around zero with approximately equal variance for the complete range of nugget width values. There were no apparent systematic patterns or trends, which indicated that the model specification was satisfactory and key assumptions of regression were satisfied. However, the residual values for a limited number of points (4) went beyond ±0.5, suggesting the presence of outliers or infrequent process anomalies (e.g., weld expulsion or electrode wear). These outliers underscored the necessity of process knowledge and ongoing monitoring, even with high-performing models.

The experimental data appeared concentrated within the 4.5–8.5 mm nugget width range, indicating that predictions beyond this interval might suffer from reduced reliability due to limited training data coverage. This constraint warranted caution if the models were to be deployed in scenarios with different material combinations or process parameters that could produce nugget dimensions outside the validated range.

5.6 Model Prediction Accuracy and Residual Analysis for Nugget Penetration

The performance evaluation of Ridge Regression and Gradient Boosting models for nugget penetration prediction revealed substantial contrasts in predictive capability, with residual analysis exposing fundamental model limitations that could influence welding quality control as illustrated in Figure 5.4. This comparison demonstrated the critical importance of selecting appropriate algorithms for capturing the complex physics governing nugget penetration behavior in HSR joints.

Ridge Regression (Figure 5.4(a)) exhibited considerable scatter around the diagonal line, especially at lower (0.5–0.7 mm) and higher (0.9–1.1 mm) penetration values. Predictions clustered around 0.6–0.8 mm penetration depth, regardless of actual value, which indicated that the linear model failed to capture the full variability in penetration and often produced errors greater than 0.1 mm. In comparison, Gradient Boosting as shown in Figure 5.4(b) was able to

generate predictions that were positioned closer to the diagonal, with improved alignment across most of the penetration range. While some scattering was evident, particularly with a slight excess in the 0.7–1.1 mm penetration range, the deviations were markedly reduced compared to Ridge Regression, indicating better modeling of the non-linear relationships inherent in penetration formation.

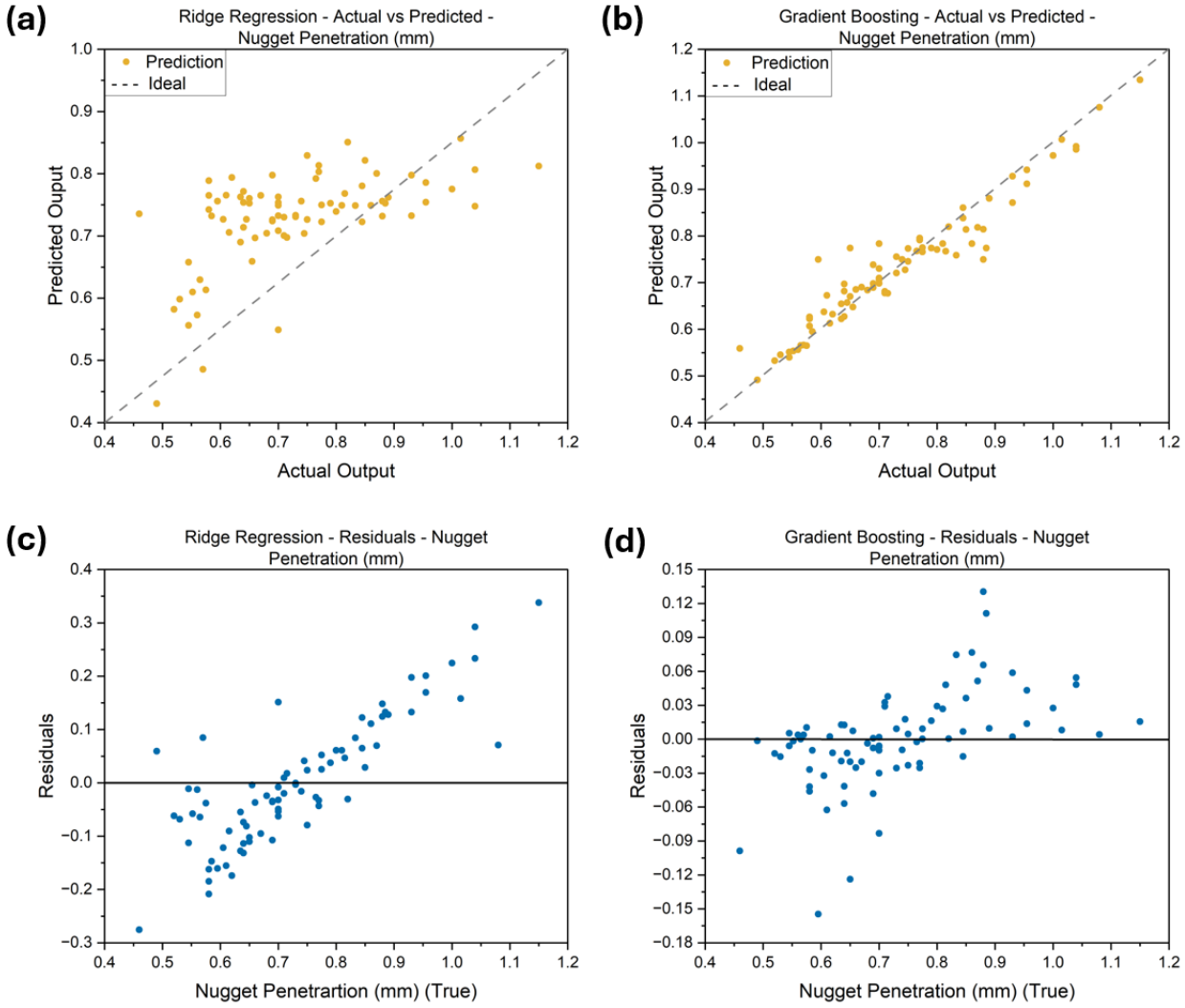


Figure 5.4. Comparison of Ridge Regression and Gradient Boosting models for nugget penetration prediction: (a, b) Actual vs. predicted plots; (c, d) corresponding residual distributions.

Residual analysis also identified issues with Ridge Regression mode capability. The Ridge Regression residuals (Figure 5.4(c)) showed a pattern of heteroscedasticity with residual variance increasing significantly after 0.8 mm, demonstrating a fan-shaped distribution. At lower penetration values, residuals were largely negative while they were larger and mostly positive at higher penetration values suggesting systematic under-prediction and over-prediction respectively. The bias and homoscedastic trend of the residuals also suggested that key non-linearities were not accurately captured by the model and therefore errors in prediction would be considerably large and unacceptable in welding if precision were needed. Residuals for the Gradient Boosting model, shown in Figure 5.4(d), displayed a preferable random clustering pattern centered around zero, with less variability (or spread) throughout most of the fitted range, which implied a better model specification. However, some mild heteroscedasticity was still present at the higher end of the penetration scales, as well as some residuals were > ±0.10 mm. These outliers indicated an influential data point or process variability (e.g. unusual welding conditions or measurement noise).

Both models functioned in a relatively narrow and sparsely populated penetration range (0.5–1.1 mm), with data gaps particularly noticeable between 0.6–0.7 mm and 0.9–1.0 mm. The gaps in the training data and low density of measurements raised concerns with the ability of either model to generalize and reliably interpolate outside of the training dataset, especially in scenarios with new combinations of materials or parameter regimes not fully represented in the training datasets. This limitation highlighted the need for expanded experimental datasets to improve model robustness across broader parameter ranges.

5.7 SHAP Feature Importance in Nugget Width and Penetration Prediction

SHAP (SHapley Additive exPlanations) was used to interpret the model by showing how each feature contributed to predictions. It helped identify the influence of individual process parameters and their interactions, making it valuable for validating model behavior and ensuring safe application in manufacturing. Unlike traditional importance measures, SHAP provided both local explanations for single predictions and global rankings of feature importance, offering a clearer understanding of model decisions. The SHAP analysis identified visually distinct differences in the importance of the features between the Ridge regression model and the Gradient boosting models for predicting welding parameters. In the Ridge regression model for maximum nugget

width as shown in Figure 5.5(a), current and weld time appeared to be the most significant parameters with both positive and negative SHAP values that suggested increasing any of these parameters generally increased nugget diameter [1, 68]. Features related to current showed considerable variability in their impact; for example, the Current × Pulses and Total Weld Time × Current² features had both positive and negative impacts depending on the combination of parameters. The Force parameter displayed predominantly negative SHAP values, suggesting that increased force generally reduced nugget width predictions in this linear mode.

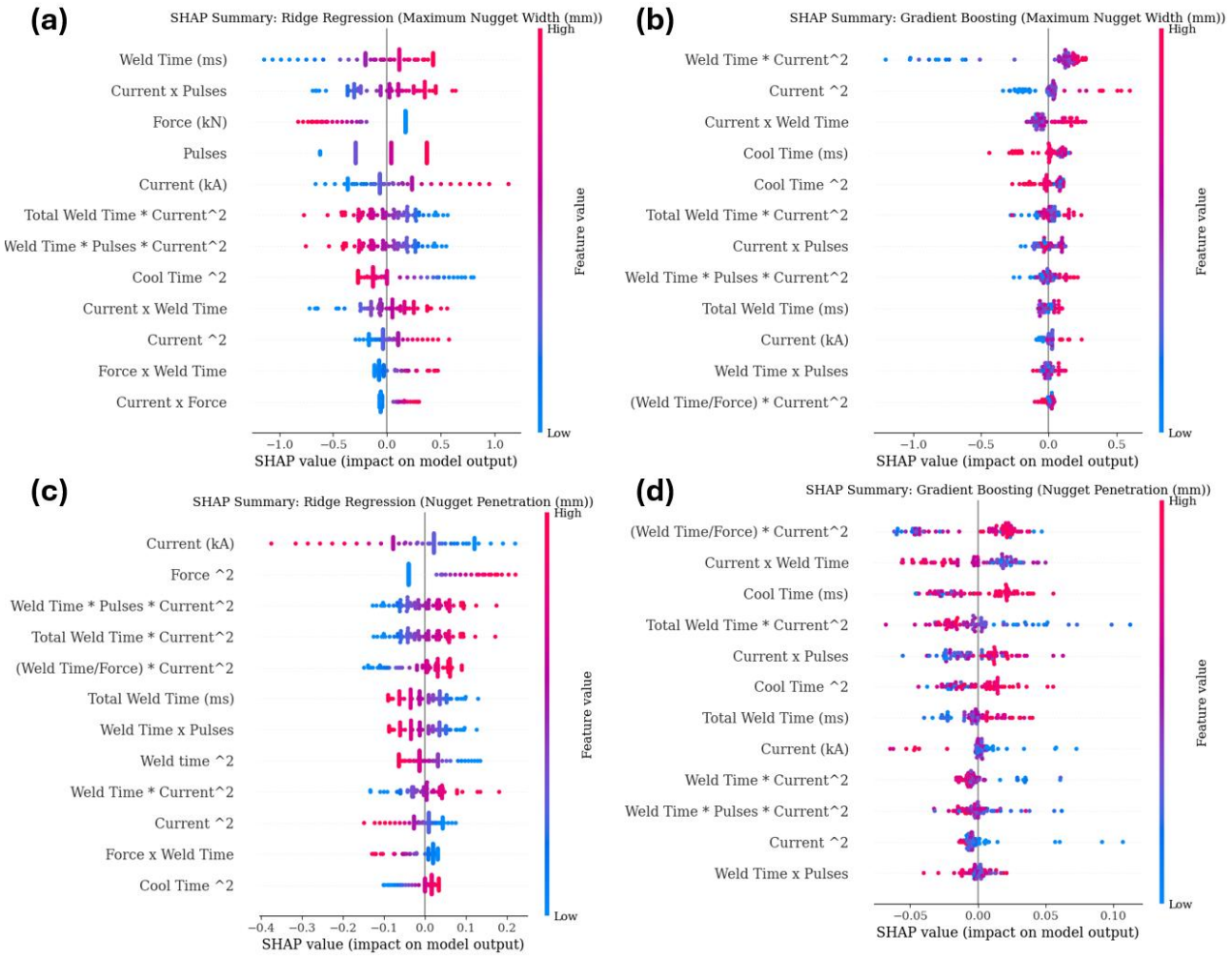


Figure 5.5. SHAP summary plots are shown for both Ridge Regression (a, c) and Gradient Boosting (b, d), highlighting differences in feature importance and model interpretability for maximum nugget width and nugget penetration respectively

The gradient boosting model for maximum nugget width (Figure 5.5(b)) showed quite different results regarding feature importance as compared to Ridge regression, demonstrating that the algorithm could capture and modelling complex non-linear relationships. Current emerged as a highly influential parameter with variable impacts, showing both strong positive and negative SHAP values that depended on the specific parameter context. Weld Time × Current interaction terms had significant influence with mixed directional effects, illustrating complex non-linear relationships that the boosting algorithm could consider better than the linear methods.

For the prediction of nugget penetration, using Ridge regression (as shown in Figure 5.5(c)), Current became the most significant feature showcasing the largest positive SHAP values, demonstrating the importance of this parameter in generating the necessary heat for the nugget to grow through all sheets in joint [1, 16, 68]. Force × Weld Time displayed strong negative contributions, indicating an interaction effect where the combination of these parameters reduced penetration depth. Weld Time^2 had a moderate positive contribution, suggesting that there is a non-linear relationship between weld time and penetration which the Ridge model was attempting to model through polynomial terms. In the gradient boosting penetration model (Figure 5.5(d)), surprisingly Cool Time appeared as a notable contributor with positive SHAP values, indicating its importance in final nugget formation and solidification processes. Current × Weld Time interactions maintained strong influence, while individual current-related parameters showed more concentrated positive contributions compared to the Ridge model. The model demonstrated greater sensitivity to parameter combinations and threshold effects, as evidenced by the wider SHAP value distributions and more complex interaction patterns.

The results of the SHAP analysis reiterated that welding current was the most important process parameter for both nugget diameter and penetration control, while the force parameters typically promoted restraining effects on the nugget formation process [1, 6, 166]. Notably, the presence of meaningful interaction terms across both models suggested that selecting the optimal welding parameter would always require combinations of parameters rather than individual optimization. Moreover, the differences in Ridge vs. Gradient Boosting behavior suggested the presence of some non-linear relationship in the welding process requiring a more sophisticated modeling approach to capture it in its entirety. These findings supported the implementation of multi-parameter

optimization strategies in welding process control, with particular attention to current-force and current-time interaction effects for achieving desired nugget characteristics [16].

5.8 Inverse Modeling Accuracy and Experimental Validation

The objective of this section was to evaluate the practical accuracy and reliability of the developed ML models through inverse parameter prediction, testing how well the models understood the underlying relationships in the experimental data. where optimal process settings had to be identified to achieve desired nugget dimensions. Inverse modeling represented a shift from traditional forward prediction by enabling engineers to define target outputs and determine the required input parameters. This approach was particularly valued in manufacturing, where optimization depended on meeting performance criteria rather than predicting outcomes from preset conditions.

The inverse analysis followed a two-stage validation process. First, the trained Gradient Boosting model established the forward relationship between process parameters and nugget dimensions using the experimental dataset. Second, an optimization algorithm searched the parameter space to identify combinations that achieved target nugget dimensions. For comparison, traditional statistical optimization with Minitab's response surface methodology (RSM) was also applied, which represented conventional approaches that were widely used in industry despite limitations with non-linear systems. The objective function minimized the squared difference between predicted and target nugget dimensions, with constraints set to keep parameter values within realistic ranges.

The cross-sectional images of welded joints based on the predicted process parameters from Gradient Boosting ML model and Minitab statistical analysis are show in Figure 5.6 where white dashed lines marked the nugget boundaries. Images (a), (c), and (e) corresponded to Gradient Boosting results, while (b), (d), and (f) represented Minitab predictions. The micrographs highlighted distinct nugget shapes and penetration characteristics for each method, allowing direct visual comparison between the modeling outcomes. The numerical data in Table 5.3 revealed considerable differences in prediction accuracy between the two approaches.

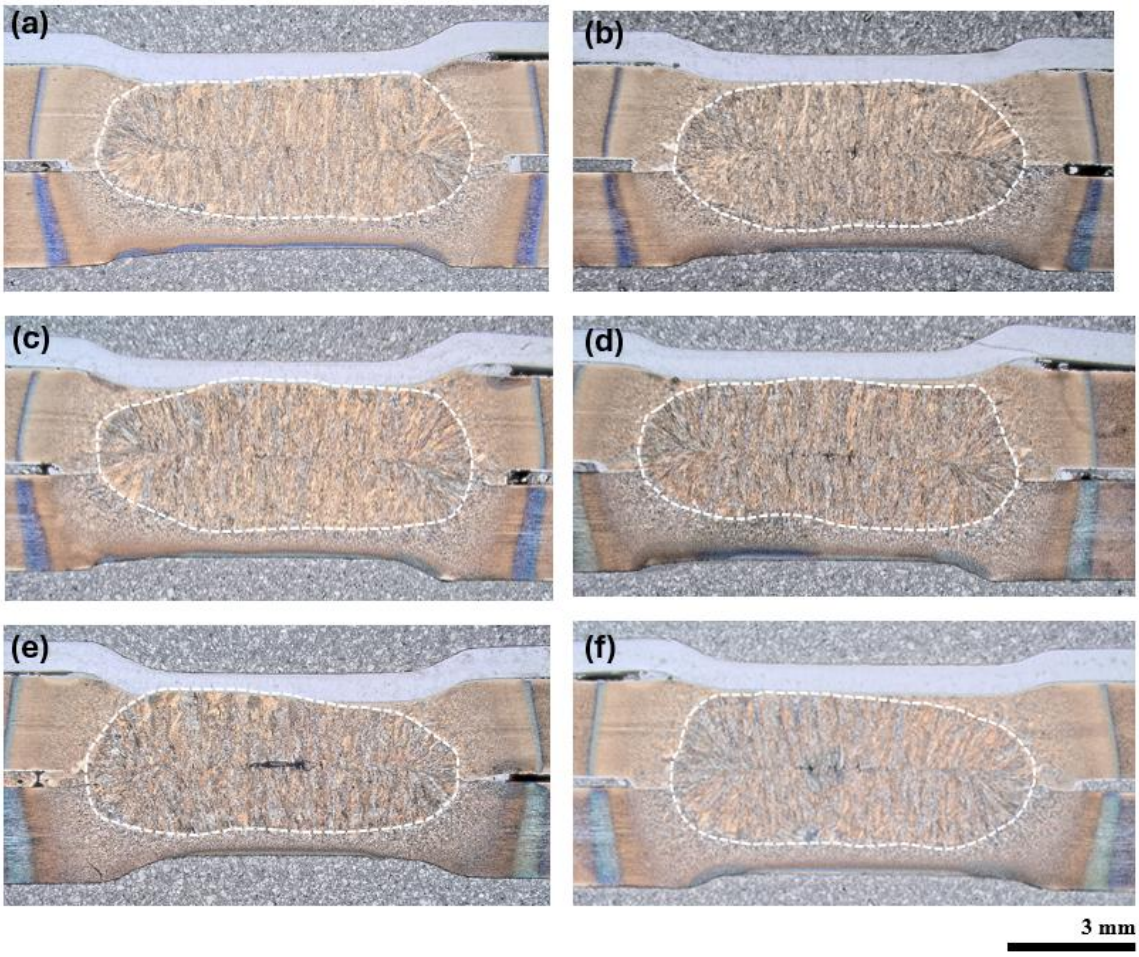


Figure 5.6. Comparison of nugget cross-sections predicted by Gradient Boosting model (a, c, e) and Minitab statistical analysis (b, d, f)

The experimental results from Gradient Boosting model reported a maximum nugget width of 7.60 ± 0.27 mm and nugget penetration of 0.17 ± 0.08 mm, with prediction error of 1.33% and 13.34% respectively. Conversely, Minitab based experimental results predicted a maximum nugget width of 7.02 ± 0.16 mm and penetration of 0.07 ± 0.04 mm with errors of 8.10% and 30.00%, respectively, which are considerably higher than those from the Gradient Boosting model, particularly for nugget penetration. Although the ML model reduced the prediction error for nugget penetration compared to Minitab, a 13.34% error remained significant. This magnitude of error could be attributed human error, systematic error and procedural errors or limitations especially as well as the limited dataset, which constrained both the ML and Minitab models in fully capturing and analyzing key features. As mentioned in Chapter 2, The fundamental physics of the welding process, where small variations in process parameters can cause large changes in nugget

penetration especially at thin-thick interface further contributed to prediction challenges. Non-linear heat generation, heat transfer processes in RSW, and metallurgical interactions between dissimilar sheets resulted in a highly complex system, difficult even for advanced predictive models to learn patterns from the small data set.

Table 5.3. Comparison of machine learning and Minitab inverse prediction results for maximum nugget width and nugget penetration, including measured values with 95% confidence intervals and corresponding percentage errors

	Target		**Measured**		**%Error**	
Method	Max Nugget Width (mm)	Nugget Penetration (mm)	Max Nugget Width (mm)	Nugget Penetration (mm)	Max Nugget Width	Nugget Penetration
Gradient Boosting	7.50	0.15	7.60 ± 0.27	0.17 ± 0.08	1.33	13.34
Minitab	6.50	0.10	7.02 ± 0.16	0.07 ± 0.04	8.10	30.00

Apart from the limited data set, variance in the data was also important to consider. The better performance of the ML model in predicting maximum nugget width was mainly due to the high variance in width measurements, which allowed sufficient variability for the algorithm to develop robust relationships. In contrast, the nugget penetration measurements were consistently confined to a narrow range of approximately ±0.1 mm; making difficult for ML model and Minitab to understand the relation between input process parameters and output in broader range and showed poor results.

5.9 Summary

This chapter presented the comprehensive development and validation of ML models for predicting nugget dimensions in dissimilar AHSS HSR welded joints, establishing a robust framework for process parameter optimization. Data quality evaluation verified statistical normality by Anderson-Darling tests (p-values of 0.262 for width and 0.581 for penetration), and no substantial outliers identified using standard Grubbs' tests. The feature correlations heatmap revealed complex dependencies amongst the welding parameters, with strong negative correlations found between the force and timing parameters (r = -0.52 to -0.80). Amongst the six supervised

ML algorithms, Gradient Boosting achieved superior accuracy for both maximum nugget width (R^2 of 0.95) and nugget penetration (R^2 of 0.90). The ensemble methods' success stemmed from their ability to capture non-linear threshold effects and parameter interactions inherent in welding physics, while linear models failed to represent the complex thermal-mechanical relationships governing nugget formation.

The residual analysis provided strong support for model competence, Gradient Boosting residuals were randomly distributed, while Ridge Regression indicated systematic heteroscedasticity and bias patterns indicating fundamental model inadequacy for welding applications. The SHAP analysis indicated that welding current was the dominant parameter in nugget width and penetration prediction and the interaction effects between current, time, and force. The experimental verification of inverse modeling showed the practical advantages of utilizing ML methods, with Gradient Boosting predicted nugget width and penetration errors of 1.33% and 13.34% respectively, compared to 8.10% and 30.00% for traditional Minitab statistics. The 13.34% penetration error was mainly due to limited experimental dataset of 80 conditions constraining the algorithms ability to learn complex input-output relationships and narrow measurement range of nugget penetration.

6. Conclusion and Future Recommendations

6.1 Conclusion

The automotive industry's adoption of AHSS in HSR assemblies has created critical challenges for RSW quality assessment, where conventional AWS D8.1 nugget penetration criteria prove inadequate for ensuring joint reliability under mechanical strength analysis. This research successfully demonstrated that HSR joints can achieve required mechanical strength through alternative bonding mechanisms, even when they did not meet the minimum 20% penetration requirement specified by AWS D8.1 guidelines. Welding current was identified as most significant process parameters influencing both nugget through-thickness and diametric growth. ML models were developed that achieved higher R^2 values than Minitab statistical tool, confirming the effectiveness of models architecture in capturing input-output nonlinear relations. Inverse modeling framework were also validated, reducing parameter prediction significantly compared with traditional statistical methods. Importantly, these results were achieved using a relatively small experimental dataset (80 runs), showing that carefully designed models and inverse analysis could deliver high accuracy without relying on the large datasets typically assumed necessary for ML models to train in engineering domain.

The integration of BBD and LHS methodologies established a robust analytical framework that was used to investigate the complex interactions between resistance spot welding RSW process parameters and nugget formation in HSR dissimilar AHSS joints across 80 experimental conditions. Welding current ($p = 0.004$) was found as the most influential parameter, driving heat generation per Joule’s law, and substantially enhancing nugget diametric growth in both interfaces and penetration into thin sheet. Weld time per pulse precisely regulated heat input duration, directly affecting nugget consistency and reliability. Electrode force was pivotal, critically modulating interfacial contact resistance, heat distribution, and subsequent nugget morphology. Interpulse cooling time alone showed minimal direct impact; however, it became notably significant through interactions with electrode force and weld time, playing a vital role in thermal dissipation and nugget stability. Although the number of pulses exhibited a more subtle direct influence on nugget penetration, it importantly contributed to microstructural refinement and overall nugget homogeneity.

Experimental validation revealed that brazing and diffusion bonding mechanisms significantly contributed to joint strength when nugget penetration is limited in HSR joints. Interrupted welding experiments indicated that penetration into the thin sheet occurred only beyond critical parameter thresholds (≥8.5 kA current, ≥200 ms weld time, ≤4.5 kN force), with lateral nugget expansion predominantly driven by rapid heat dissipation through electrode contact points. Systematic characterization demonstrated that joints lacking observable nugget penetration into the thin top sheet can still attain mechanical strengths sufficient for PPO/PO failure modes. Detailed bondline analyses via EDS mapping elucidated two distinct non-fusion bonding mechanisms: solid-state diffusion, characterized by uniform elemental distributions (Fe, Mn, Si), indicative of metallurgical continuity like conventional fusion; and localized brazing, marked by sharp compositional gradients and aluminum-rich interlayers resulting from partial melting and rapid solidification of Zn-Al-Si coatings. Mechanical tests consistently demonstrated failure initiation within the thin top sheet's base material, irrespective of nugget penetration, validating observations from interrupted tensile tests that revealed fracture propagation predominantly within the IF steel base metal.

Developed ML models achieved exceptional accuracy. The comparison of six supervised ML algorithms showed distinct performance hierarchy. Gradient Boosting achieved optimal results with R^2 values of 0.948 for maximum nugget width and 0.903 for nugget penetration. These results substantially outperformed traditional linear approaches, with Ridge and Lasso regression achieving R^2 values below 0.60 for both parameters. SHAP analysis also showed welding current as dominant process parameter while identifying critical interaction effects between current, time, and force that simple optimization approaches would miss.

Finally, this work also established and experimentally validated an inverse modeling framework capable of proposing optimal process parameters for desired nugget dimensions. Gradient Boosting achieved prediction errors of 1.33% for maximum nugget width and 13.34% for nugget penetration, compared to 8.10% and 30.00% for Minitab linear regression-based optimization. The better performance of the ML model in predicting maximum nugget width was mainly due to the high variance in width measurements, which allowed sufficient variability for the algorithm to develop robust relationships. In contrast, the nugget penetration measurements were consistently confined to a narrow range of approximately ±0.1 mm; making difficult for ML model and for

Minitab to capture the complex nonlinear relation between input process parameters and output in broader range and showed poor results.

The findings of this research challenge the conventional reliance on visible nugget penetration into the thin sheet, often interpreted as a key indicator of weld quality in practice and call for updated acceptance criteria that emphasize interfacial bonding quality, especially in HSR AHSS assemblies. The validated ML framework, particularly Gradient Boosting algorithms, provides automotive manufacturers with quantifiable improvements in process control accuracy, offering significant reduction in prediction error compared to simple statistical analysis regression-based approaches. This improvement in overall prediction reliability translates directly to enhanced manufacturing quality assurance, reduced weld rejection rates, and potential cost savings of approximately in quality control operations through elimination of unnecessary rewelding of structurally sound joints that fail conventional penetration criteria. The integration of systematic DOE with ensemble machine learning methods establishes a scalable framework for intelligent welding process optimization that can be extended across diverse AHSS material combinations and joint configurations, providing the automotive industry with data-driven quality evaluation protocols that surpass traditional penetration-based assessment limitations and support the continued adoption of lightweight, high-strength materials essential for fuel efficiency and safety standards compliance.

6.2 Future Recommendations

Recognizing the limitations of supervised learning ML methods, future work should aim towards a hybrid method combining physics based modeling and advanced data-driven modeling strategies. While gradient boosting was successful at predicting results, the limited number of experimental runs highlighted issues of overfitting and underfitting. With multipulse welding schedules of up to five pulses with fixed magnitudes, we can improve prediction by observing changes in resistance signals and incorporating them explicitly into the ML framework. Recent work from Xia *et al.* [79] has revealed that DR signals during resistance spot welding (RSW) primarily reflect changes in the average sheet temperature and electrode-sheet contact conditions, rather than nugget size alone. This point underscores the need to extract physical features from multipulse data. For example, cumulative heat inputs across pulses, effective cooling times, thermal gradients from resistance evolution, and indices of the heating and cooling phases can be

integrated as meaningful parameters. These parameters inherently capture the thermal history of the weld, which directly affects the microstructural evolution of the nugget and HAZ [80, 165, 167, 168]. In addition, an advanced feature-extraction approach should be employed on the DR curves from multipulse welding. For each pulse in the schedule, features such as the peak resistance values, resistance rise rates, time reaching peak resistance, resistance decay curves, and baseline shifts between pulses should all be analyzed quantitively [132, 167]. These features are based on the underlying physical phenomena in the welding process and offer significant insight into how each individual pulse and the cumulative effect of multipulse welding influence nugget penetration and growth behavior, especially in HSR joints. Additionally, conducting FEA and numerical simulations alongside the implementation of these ML strategies will help define and clarify the dynamic resistance features derived from the multipulse and the resultant nugget characteristics. This can help explain why some multipulse schedules create a significantly deeper nugget penetration into thin sheet in HSR joints while other schedules result in an overly wide nugget formation without sufficient nugget depth. This will allow for the development of predictive models that are more interpretable and reliable by connecting experimental validation with numerical models and simulations. Overall, the incorporation of physics-informed features from the multipulse DR signal and advanced ML capabilities represents a promising and innovative path forward.

References

1. Pouranvari M, Marashi SPH (2010) Factors affecting mechanical properties of resistance spot welds. Mater Sci Technol 26:1137–1144. https://doi.org/10.1179/174328409X459301

2. Soomro IA, Pedapati SR (2019) Application of in situ post weld heat treatment using double pulse technology and its effect on microstructure and mechanical performance of resistance spot welded HSLA350 steel. Int J Adv Manuf Technol 105:3249–3260. https://doi.org/10.1007/s00170-019-04569-2

3. Tisza M (2021) Three Generations of Advanced High Strength Steels in the Automotive Industry. In: Lecture Notes in Mechanical Engineering. Springer Science and Business Media Deutschland GmbH, pp 81–94

4. Zhang H, Senkara J (2011) Resistance Welding : Fundamentals and Applications, Second Edition. CRC Press

5. Kimchi M, Phillips DH (2017) Resistance Spot Welding: Fundamentals and Applications for the Automotive Industry. Synth Lect Mech Eng 1:i–115. https://doi.org/10.2200/s00792ed1v01y201707mec005

6. Lu Y, Peer A, Kimchi M, et al (2019) Haz Softening of Resistance Spot Welded 3T Dissimilar Steel Stack-up. Weld J 98:328S-336S. https://doi.org/10.29391/2019.98.027

7. Eizadi H, Marash SPH (2016) On the resistance spot welding of four-sheet stack of unequal sheet thickness. Sci Technol Weld Join 21:632–637. https://doi.org/10.1080/13621718.2016.1149933

8. Harlin N, Jones TB, Parker JD (2002) Weld growth mechanisms during resistance spot welding of two and three thickness lap joints. Sci Technol Weld Join 7:35–41. https://doi.org/10.1179/136217102225001494

9. American Welding Society (2021) D8.1M:2021 Specification For Automotive Weld Quality-Resistance Spot Welding Of Steel

10. Gould J, Peterson W, Cruz J (2013) An examination of electric servo-guns for the resistance spot welding of complex stack-ups. Weld World 57:243–256. https://doi.org/10.1007/s40194-012-0019-x

11. Brechelt S, Wiche H, Wesling V (2019) Influence of pre-pulse in spot weld bonding of three-sheet steel stack-up. Weld World 63:771–782. https://doi.org/10.1007/s40194-019-00706-3

12. Manladan SM, Hamza M, Ramesh S, Luo Z (2023) Lap-shear performance of weld-bonded Mg alloy and austenitic stainless steel in three-sheet stack-up. https://doi.org/10.21203/rs.3.rs-2550855/v1

13. Zhou L, Zheng W, Li T, et al (2020) A material stack-up combination identification method for resistance spot welding based on dynamic resistance. J Manuf Process 56:796–805. https://doi.org/10.1016/j.jmapro.2020.04.051

14. Zhang W (2002) SORPAS-The Professional Software for Simulation of Resistance Welding. APA

15. Xia YJ, Song Q, Yi BG, et al (2025) Improving out-of-distribution generalization for online weld expulsion inspection using physics-informed neural networks. Weld World 69:1309–1322. https://doi.org/10.1007/s40194-025-01950-6

16. Mezher MT, Pereira A, Trzepieciński T (2024) Predicting the Effect of RSW Parameters on the Shear Force and Nugget Diameter of Similar and Dissimilar Joints Using Machine Learning Algorithms and Multilayer Perceptron. Materials (Basel) 17:. https://doi.org/10.3390/ma17246250

17. Wang Y, Rao Z, Wang F Heat evolution and nugget formation of resistance spot welding under multi-pulsed current waveforms. https://doi.org/10.1007/s00170-020-06337-z/Published

18. Crippa M, Guizzardi D, Pagani F, et al (2024) GHG emissions of all world countries 2024. Publications Office of the European Union

19. Epa U, of Transportation O, Quality A, Division S (2023) Revised 2023 and Later Model Year Light-Duty Vehicle Greenhouse Gas Emissions Standards – Regulatory Update (EPA-420-F-21-060, August 2021)

20. Epa U, of Transportation O, Quality A, Division S (1990) Fast Facts: U.S. Transportation Sector Greenhouse Gas Emissions, 1990-2022 (EPA-420-F-24-022, May 2024)

21. Ducker Worldwide - Critical thinking for critical decesions

22. Keeler,S., M. Kimchi and PJM (2017) Advanced High-Strength Steels Apllication Guidelines Version 6.0. WorldAutoSteel

23. Soomro IA, Rao Pedapati S, Awang M A review of advances in resistance spot welding of automotive sheet steels: emerging methods to improve joint mechanical performance. https://doi.org/10.1007/s00170-021-08002-5/Published

24. Sah SK, Bawase MA, Saraf MR (2014) Light-weight materials and their automotive applications. In: SAE Technical Papers. SAE International

25. Demeri MY. (2013) Advanced high-strength steels : science, technology, and applications. ASM International

26. Hilditch TB, de Souza T, Hodgson PD (2015) Properties and automotive applications of advanced high-strength steels (AHSS). In: Welding and Joining of Advanced High Strength Steels (AHSS). Elsevier Inc., pp 9–28

27. Perdahcıoğlu ES, Geijselaers HJM (2022) Mechanical Behavior of Multi-Phase Steels Comprising Retained Austenite. Materials (Basel) 15:. https://doi.org/10.3390/ma15020498

28. Pouranvari M, Marashi SPH (2013) Critical review of automotive steels spot welding: Process, structure and properties. Sci. Technol. Weld. Join. 18:361–403

29. Kalhor A, Soleimani M, Mirzadeh H, Uthaisangsuk V (2020) A review of recent progress in mechanical and corrosion properties of dual phase steels. Arch. Civ. Mech. Eng. 20

30. Schell KG, Lemke F, Bucharsky EC, et al (2017) Microstructure and mechanical properties of Li0.33La0.567TiO3. J Mater Sci 52:2232–2240. https://doi.org/10.1007/s10853-016-0516-1

31. Matlock DK, Speer JG (2009) Third Generation of AHSS: Microstructure Design Concepts. Microstruct Texture Steels 185–205. https://doi.org/10.1007/978-1-84882-454-6_11

32. Raid Fekhreddine M, Tisza M (2021) Third generation of advanced high strength sheet steels for the automotive sector : A literature review. Multidiszcip tudományok 11:241–247.

https://doi.org/10.35925/j.multi.2021.4.28

33. Noder J, Gutierrez JE, Zhumagulov A, et al (2021) A comparative evaluation of third-generation advanced high-strength steels for automotive forming and crash applications. Materials (Basel) 14:. https://doi.org/10.3390/ma14174970

34. Bleck W, Brühl F, Ma Y, Sasse C (2019) Materials and Processes for the Third-generation Advanced High-strength Steels. BHM Berg- und Hüttenmännische Monatshefte 164:466–474. https://doi.org/10.1007/s00501-019-00904-y

35. Mehrabi A (2024) Phase Transformation Kinetics in Medium-Mn Third-Generation Advanced High Strength Steels. 184

36. Deardo A (1999) Recent Developments in Interstitial-Free Steels and Ferritic Stainless Steels in North America

37. Hoile S Literature review Processing and properties of mild interstitial free steels

38. (2020) Cold-rolled steel sheet and strip for automobile use

39. Osman TM, Garcia I NIOBIUM-BEARING INTERSTITIAL-FREE STEELS: PROCESSING, STRUCTURE AND PROPERTIES

40. Federal U, Preto DO, Preto O (2021) ( ) (1) (2). 24:1–10

41. Matlock DK, Speer JG (2010) Processing opportunities for new advanced high-strength sheet steels. Mater Manuf Process 25:7–13. https://doi.org/10.1080/10426910903158272

42. Wei ST, Lv D, Liu RD, Lin L (2017) Similar and dissimilar resistance spot weldability of galvanised DP1000 and TWIP980 steels. Sci Technol Weld Join 22:278–286. https://doi.org/10.1080/13621718.2016.1226569

43. Cherepanova GI, Kal'ner VD (1963) Thermomechanical treatment of steel

44. Rajarajan C, Sivaraj P, Sonar T, et al (2022) Resistance spot welding of advanced high strength steel for fabrication of thin-walled automotive structural frames. Forces Mech 7:. https://doi.org/10.1016/j.finmec.2022.100084

45. Market S AHSS 101 THE EVOLVING USE OF ADVANCED HIGH-STRENGTH STEELS FOR AUTOMOTIVE APPLICATIONS

46. Zhao J, Jiang Z (2018) Thermomechanical processing of advanced high strength steels. Prog Mater Sci 94:174–242. https://doi.org/10.1016/j.pmatsci.2018.01.006

47. Kimchi M, Phillips DH Fundamentals and Applications for the Automotive Industry Resistance Spot Welding Synthesis Lectures on Welding Engineering Second Edition

48. (2019) Hot Stamping of Ultra High-Strength Steels. Springer International Publishing

49. Fan DW, De Cooman BC (2012) State-of-the-knowledge on coating systems for hot stamped parts. Steel Res. Int. 83:412–433

50. Hu P, Liang ·, Bin He Y Hot Stamping Advanced Manufacturing Technology of Lightweight Car Body

51. Taylor T, Clough A (2018) Critical review of automotive hot-stamped sheet steel from an industrial perspective. Mater. Sci. Technol. (United Kingdom) 34:809–861

52. Afzal A, Hamedi M, Nielsen CV (2021) Numerical and experimental study of alsi coating effect on nugget size growth in resistance spot welding of hot-stamped boron steels. J Manuf Mater Process 5:. https://doi.org/10.3390/jmmp5010010

53. Karbasian H, Tekkaya AE (2010) A review on hot stamping. J Mater Process Technol 210:2103–2118. https://doi.org/10.1016/j.jmatprotec.2010.07.019

54. Amirudin A, Thierry D (1996) Corrosion mechanisms of phosphated zinc layers on steel as substrates for automotive coatings. Prog Org Coatings 28:59–75. https://doi.org/10.1016/0300-9440(95)00554-4

55. ARNOLD JO (1912) The Metallurgy of Steel. Nature 89:315–316. https://doi.org/10.1038/089315a0

56. Harlin N, Jones TB, Parker JD (2003) Weld growth mechanism of resistance spot welds in zinc coated steel. In: Journal of Materials Processing Technology. pp 448–453

57. Khan MS, Razmpoosh MH, Biro E, Zhou Y (2020) A review on the laser welding of coated 22MnB5 press-hardened steel and its impact on the production of tailor-welded blanks. Sci. Technol. Weld. Join. 25:447–467

58. Society EE, Bode H, Brodd TRJ, Kordesch K V (2011) Uhlig's Corrosion Handbook

59. Marder AR (2000) The metallurgy of zinc-coated steel. 45:

60. Aslam I, Li B, Martens RL, et al (2016) Transmission electron microscopy characterization of the interfacial structure of a galvanized dual-phase steel. Mater Charact 120:63–68. https://doi.org/10.1016/j.matchar.2016.08.014

61. Windmann M, Röttger A, Theisen W (2013) Phase formation at the interface between a boron alloyed steel substrate and an Al-rich coating. Surf Coatings Technol 226:130–139. https://doi.org/10.1016/j.surfcoat.2013.03.045

62. Al-Mukhtar AM (2016) Review of Resistance Spot Welding Sheets: Processes and Failure Mode. Adv Eng Forum 17:31–57. https://doi.org/10.4028/www.scientific.net/aef.17.31

63. He L Investigation of Liquid Metal Embrittlement in Advanced High Strength Steels

64. Murugan SP, Kim JW (2018) Optimized resistance spot welding conditions for complex combinations

65. Panza L, Bruno G, Antal G, et al (2024) Machine learning tool for the prediction of electrode wear effect on the quality of resistance spot welds. Int J Interact Des Manuf. https://doi.org/10.1007/s12008-023-01733-7

66. Kas Z, Das M (2019) Adaptive Control of Resistance Spot Welding Based on a Dynamic Resistance Model. Math Comput Appl 24:86. https://doi.org/10.3390/mca24040086

67. (2024) Mechanical Properties and Failure Behavior of Resistance Spot Welded Third-Generation Advanced High Strength Steels by Mohammad Shojaee A thesis presented to the University of Waterloo in fulfillment of the thesis requirement for the degree of Doctor of P

68. Shojaee M, Midawi ARH, Barber B, et al (2021) Mechanical properties and failure behavior of resistance spot welded third-generation advanced high strength steels. J Manuf Process 65:364–372. https://doi.org/10.1016/j.jmapro.2021.03.047

69. Zhao D, Wang Y, Zhang P, Liang D (2019) Modeling and experimental research on resistance spot welded joints for dual-phase steel. Materials (Basel) 12:. https://doi.org/10.3390/ma12071108

70. AWS_D8_1_2007

71. Kim EW, Eagar TW (1988) Parametric analysis of resistance spot welding lobe curve. SAE Tech Pap. https://doi.org/10.4271/880278

72. Valaee-Tale M, Sheikhi M, Mazaheri Y, et al (2020) Criterion for predicting expulsion in resistance spot welding of steel sheets. J Mater Process Technol 275:116329. https://doi.org/10.1016/j.jmatprotec.2019.116329

73. Chen S, Wu N, Xiao J, et al (2019) Expulsion identification in resistance spot welding by electrode force sensing based on wavelet decomposition with multi-indexes and BP neural networks. Appl Sci 9:. https://doi.org/10.3390/app9194028

74. Zhou K, Cai L (2014) On the development of nugget growth model for resistance spot welding. J Appl Phys 115:. https://doi.org/10.1063/1.4872247

75. Ramachandran DC, Figueredo B, Sherepenko O, et al (2022) A study on improving the mechanical performance by controlling the halo ring in the Q&P 980 steel resistance spot welds. J Manuf Process 75:320–330. https://doi.org/10.1016/j.jmapro.2022.01.019

76. Ighodaro O (2017) Effects of Metallic Coatings on Resistance Spot Weldability of Hot Stamping Steel. Thesis 1–110

77. Zhou K, Shi T, Cai L (2017) Online measuring the electrical resistivity of molten nugget of stainless steel in resistance spot welding. J Manuf Process 28:109–115. https://doi.org/10.1016/j.jmapro.2017.05.026

78. Yu J (2018) Adaptive resistance spot welding process that reduces the shunting effect for automotive high-strength steels. Metals (Basel) 8:. https://doi.org/10.3390/met8100775

79. Xing B, Xiao Y, Qin QH, Cui H (2018) Quality assessment of resistance spot welding process based on dynamic resistance signal and random forest based. Int J Adv Manuf Technol 94:327–339. https://doi.org/10.1007/s00170-017-0889-6

80. Xia YJ, Lv TL, Ghassemi-Armaki H, et al (2023) Quantitative Interpretation of Dynamic Resistance Signal in Resistance Spot Welding. Weld J 102:69–87. https://doi.org/10.29391/2023.102.006

81. Dickinson DW, Franklin JE, Stanya A (1980) Characterization of Spot Welding Behavior By Dynamic Electrical Parameter Monitoring. Weld J (Miami, Fla) 59:

82. Xia YJ, Su ZW, Li YB, et al (2019) Online quantitative evaluation of expulsion in resistance spot welding. J Manuf Process 46:34–43. https://doi.org/10.1016/j.jmapro.2019.08.004

83. Wintjes E, DiGiovanni C, He L, et al (2019) Effect of Multiple Pulse Resistance Spot Welding Schedules on Liquid Metal Embrittlement Severity. J Manuf Sci Eng 141:1–9. https://doi.org/10.1115/1.4044099

84. Study P, Mode F (2021) Double Pulse Resistance Spot Welding of Dual Phase Steel :

85. Stavropoulos P, Sabatakakis K (2024) Quality Assurance in Resistance Spot Welding: State of Practice, State of the Art, and Prospects. Metals (Basel). 14

86. AWS D8.9M-2012 Test methods for evaluating the resistance spot welding behavior of automotive shet steel materials

87. Chang BH, Zhou Y (2003) Numerical study on the effect of electrode force in small-scale resistance spot welding. J Mater Process Technol 139:635–641. https://doi.org/10.1016/S0924-0136(03)00613-7

88. Reducing surface marking on resistance spot welded joints - TWI. https://www.twi-global.com/technical-knowledge/faqs/faq-how-can-i-minimise-the-surface-marking-on-resistance-spot-welded-joints. Accessed 23 Jul 2025

89. Francis JA, Bhadeshia HKDH, Withers PJ (2007) Welding residual stresses in ferritic power plant steels. Mater Sci Technol 23:1009–1020. https://doi.org/10.1179/174328407X213116

90. Yu J (2017) Effect of cover sheet on dissimilar three-steel sheets resistance spot welding. Int J Adv Manuf Technol 89:483–491. https://doi.org/10.1007/s00170-016-9098-y

91. Huda N, Nam D-G, Park Y-D (2019) Study on the Mechanism of Nugget Growth Behavior in Three Sheets Stack Resistance Spot Welding. J Weld Join 37:564–571. https://doi.org/10.5781/jwj.2019.37.6.5

92. AWS D8_9-2012 full

93. Pouranvari M, Marashi SPH (2010) Key factors influencing mechanical performance of

dual phase steel resistance spot welds. Sci Technol Weld Join 15:149–155. https://doi.org/10.1179/136217109X12590746472535

94. Ma Y, Takikawa A, Nakanishi J, et al (2021) Measurement of local material properties and failure analysis of resistance spot welds of advanced high-strength steel sheets. Mater Des 201:109505. https://doi.org/10.1016/j.matdes.2021.109505

95. Sun X, Stephens E, Khaleel M (2006) Effects of fusion zone size on failure modes and performance of advanced high strength steel spot welds. SAE Tech Pap. https://doi.org/10.4271/2006-01-0531

96. Version D (2019) Resistance spot welding of advanced high strength steels Publisher ' s PDF , also known as Version of record Publication date :

97. Pouranvari M, Ranjbarnoodeh E (2011) Resistance spot welding characteristic of ferrite-martensite DP600 dual phase advanced high strength steel-part III: Mechanical properties. World Appl Sci J 15:1521–1526

98. Pouranvari M, Marashi SPH, Jaber HL (2015) Dp780 dual-phase-steel spot welds: Critical fusion-zone size ensuring the pull-out failure mode. Mater Tehnol 49:579–585. https://doi.org/10.17222/mit.2014.184

99. Peer AJ (2017) Performance Testing and Modeling of Ultra-High Strength Steel and Complex Stack-Up Resistance Spot Welds. 1–175

100. Wei ST, Liu RD, Lv D, et al (2016) Effect of joint configuration on resistance spot weldability of galvanised DP780 steel sheets. Sci Technol Weld Join 21:178–185. https://doi.org/10.1179/1362171815Y.0000000081

101. Huda N, Park Y-D (2012) Weldability Evaluation and Nugget Formation Mechanism in Three Sheets Spot Welding of High Strength Steels

102. Ariyanto, Sukardin MS, Renreng I, et al (2023) OPTIMIZATION OF RESISTANCE SPOT WELDING WITH SURFACE ROUGHNESS DISSIMILAR MILD STEEL WITH STAINLESS STEEL. Eastern-European J Enterp Technol 5:63–71. https://doi.org/10.15587/1729-4061.2023.285711

103. Wei S, Li Y, Lu S (2022) Similar and dissimilar resistance spot weldability of Q&P980 and

TWIP1180 steels. Sci Technol Weld Join 27:77–83. https://doi.org/10.1080/13621718.2021.1953941

104. Patel M (2022) Liquid metal embrittlement cracking in dissimilar resistance spot welding of 3rd Gen-Advanced high strength steel: mitigation methods and associated mechanisms

105. Nielsen, Chris Valentin ; Friis, Kasper Storgaard ; Zhang, W. ; Bay N (2011) Three-Sheet Spot Welding of Advanced High-Strength Steels. Weld J (Miami, Fla) 90:32–40

106. Baluch N, Mohamed Udin Z, Sobry Abdullah C (2014) Advanced High Strength Steel in Auto Industry: an Overview

107. Selova L, Tunçel O, Aydin H, et al (2019) Mechanical Properties of Resistance Spot Welded Three-Sheet Stack Joints of Dissimilar Steels in Different Welding Time

108. Lu Y (2018) Resistance and Ultrasonic Spot Welding of Light-Weight Metals. Dissertation

109. Ikeda R, Okita Y, Ono M, et al (2014) Development of advanced resistance spot welding process using control of electrode force and welding current during welding. Weld Int 28:13–20. https://doi.org/10.1080/09507116.2012.715880

110. Kim D, Yu J, Rhee S (2016) Effect of a conically shaped hollow electrode on advanced high strength steel in three-sheet resistance spot welding. Int J Precis Eng Manuf 17:331–336. https://doi.org/10.1007/s12541-016-0041-9

111. Company FM, Coon T, Elliott A, et al (2007) Resistance spot weldability of three metal stack dual phase 600 hot-dipped galvanized steel. SAE Tech Pap 2007:. https://doi.org/10.4271/2007-01-1363

112. Lei Z, Liu J, Changxiang W (2016) Comparative Fatigue Life Study on the Indentation Levels of Resistance Spot Welds with Dual Phase Steel

113. Ren J, Dong W, Zhang Y, Yu Z (2019) Failure Analysis of Three-Sheet Stackup Structure Made of Dissimilar High-Strength Steel. J Mater Eng Perform 28:3438–3445. https://doi.org/10.1007/s11665-019-04140-w

114. Wei ST, Liu RD, Lv D, et al (2015) Weldability and mechanical properties of similar and dissimilar resistance spot welds of three-layer advanced high strength steels. Sci Technol

Weld Join 20:20–26. https://doi.org/10.1179/1362171814Y.0000000250

115. Zhao Y, Zhang Y, Lai X (2018) Effect of epoxy adhesive on nugget formation in resistance welding of SAE1004/DP600/DP780 steel sheets. Materials (Basel) 11:. https://doi.org/10.3390/ma11101828

116. C. V. NIELSEN, K. S. FRIIS, W. ZHANG ANBA (2011) Three-Sheet Spot Welding of Advanced High-Strength Steels The. Weld Int 90:32–40

117. Ma N, Murakawa H (2010) Numerical and experimental study on nugget formation in resistance spot welding for three pieces of high strength steel sheets. J Mater Process Technol 210:2045–2052. https://doi.org/10.1016/j.jmatprotec.2010.07.025

118. Shen J, Zhang Y, Lai X, Wang PC (2011) Modeling of resistance spot welding of multiple stacks of steel sheets. Mater Des 32:550–560. https://doi.org/10.1016/j.matdes.2010.08.023

119. Xia YJ, Lv T Le, Ghassemi-Armaki H, et al (2023) Collaborative Simulation of Nugget Growth and Process Signals for Resistance Spot Welding. Weld World 67:1377–1392. https://doi.org/10.1007/s40194-023-01489-4

120. Chen F, Wang Y, Sun S, et al (2019) Multi-objective optimization of mechanical quality and stability during micro resistance spot welding. Int J Adv Manuf Technol 101:1903–1913. https://doi.org/10.1007/s00170-018-3055-x

121. Zhu Q, Shen H, Zhu X, Wang Y (2024) Prediction of Nugget Diameter and Analysis of Process Parameters of RSW with Machine Learning Based on Feature Fusion. Electron 13:. https://doi.org/10.3390/electronics13132484

122. Zhu XK, Zhu JB, Zhang W (2022) Data-driven models of dynamic strength of resistance spot welds in high strength steels by regression and machine learning. Multiscale Multidiscip Model Exp Des 5:337–350. https://doi.org/10.1007/s41939-022-00123-y

123. Lövenborn D (2016) 3D FE Simulations of Resistance Spot Welding. 54

124. Moshayedi H, Sattari-Far I (2014) Resistance spot welding and the effects of welding time and current on residual stresses. J Mater Process Technol 214:2545–2552. https://doi.org/10.1016/j.jmatprotec.2014.05.008

125. Pandya KS, Grolleau V, Roth CC, Mohr D (2020) Fracture response of resistance spot welded dual phase steel sheets: Experiments and modeling. Int J Mech Sci 187:. https://doi.org/10.1016/j.ijmecsci.2020.105869

126. Nielsen C V., Zhang W, Perret W, et al (2015) Three-dimensional simulations of resistance spot welding. Proc Inst Mech Eng Part D J Automob Eng 229:885–897. https://doi.org/10.1177/0954407014548740

127. Andersson O, Melander A (2015) Prediction and Verification of Resistance Spot Welding Results of Ultra-High Strength Steels through FE Simulations. Model Numer Simul Mater Sci 05:26–37. https://doi.org/10.4236/mnsms.2015.51003

128. Ernst AW, Galler M, Vallant R, Enzinger N (2002) Modification of Coupling Parameters for a more accurate numerically coupled Simulation of the Resistance Spot Welding Process. 1–14

129. Venkatesh K (2018) Finite element simulation of resistance spot welding of advanced high strength steels A Project Report submitted by

130. Liu J, Jiang F, Tashiro S, et al (2025) A physics-informed and data-driven framework for robotic welding in manufacturing. Nat Commun 16:. https://doi.org/10.1038/s41467-025-60164-y

131. Ariyanto, Arsyad H, Syahid M, Renreng I (2022) Optimization of Welding Parameters for Resistance Spot Welding with Variations in the Roughness of the Surface of the AISI 304 Stainless Steel Joint to Increase Joint Quality. Int J Mech Eng Robot Res 11:877–883. https://doi.org/10.18178/ijmerr.11.11.877-883

132. Ternane F, Benachour M, Sebaa F, Benachour N (2022) www.etasr.com Ternane et al.: Regression Modeling and Process Analysis of Resistance Spot Welding on Dissimilar …

133. Zhao D, Ivanov M, Wang Y, et al (2021) Multi-objective optimization of the resistance spot welding process using a hybrid approach. J Intell Manuf 32:2219–2234. https://doi.org/10.1007/s10845-020-01638-2

134. Kitano H, Sato A, Iyota M, Nakamura T (2019) Investigation of relationship between resistance spot welding condition and nugget shape by utilizing machine learning based

technique. Weld Int 33:223–230. https://doi.org/10.1080/09507116.2020.1866902

135. He Y, Yang K, Wang X, et al (2022) Quality Prediction and Parameter Optimisation of Resistance Spot Welding Using Machine Learning. Appl Sci 12:. https://doi.org/10.3390/app12199625

136. Sim J, Kim KY (2018) Hybrid Nugget Diameter Prediction for Resistance Spot Welding. In: Procedia Manufacturing. Elsevier B.V., pp 395–402

137. Yue ZJ, Chen QR, Bao ZG, et al (2024) Improving RSW nugget diameter prediction method: unleashing the power of multi-fidelity neural networks and transfer learning. Adv Manuf 12:409–427. https://doi.org/10.1007/s40436-024-00503-2

138. Lee J, Noh I, Jeong SI, et al (2020) Development of real-time diagnosis framework for angular misalignment of robot spot-welding system based on machine learning. Elsevier B.V., pp 1009–1019

139. Prof MLB Bias-Variance-Tradeoff :

140. Chuenmee N, Phothi N, Chamniprasart K, et al (2025) Machine learning for predicting resistance spot weld quality in automotive manufacturing. Results Eng 25:. https://doi.org/10.1016/j.rineng.2024.103570

141. Zhou B, Pychynski T, Reischl M, et al (2022) Machine learning with domain knowledge for predictive quality monitoring in resistance spot welding. J Intell Manuf 33:1139–1163. https://doi.org/10.1007/s10845-021-01892-y

142. Zamanzad Gavidel S, Lu S, Rickli JL (2019) Performance analysis and comparison of machine learning algorithms for predicting nugget width of resistance spot welding joints. Int J Adv Manuf Technol 105:3779–3796. https://doi.org/10.1007/s00170-019-03821-z

143. Geng C, Buyun S, Gaocai F, et al (2024) A GAN-based method for diagnosing bodywork spot welding defects in response to small sample condition. Appl Soft Comput 157:. https://doi.org/10.1016/j.asoc.2024.111544

144. Rawal MR, Varane V, Kolhapure RR (2018) Process Parameter Optimization for Resistance Spot Welding Using Response Surface Methodology. Asian Rev Mech Eng 7:33–37. https://doi.org/10.51983/arme-2018.7.1.2839

145. Gandhi AH, Solanki PH (2024) Process Parameter Optimization of Resistance Spot Welding for AMS 4902 Titanium Grade 2 Sheet Metal. SSRG Int J Mech Eng 11:61–73. https://doi.org/10.14445/23488360/IJME-V11I10P106

146. ÇEKİÇ İ, ÇAVDAR K (2021) Building Up Mathematical Modeling Using Spot Welding Parameters and Prediction Weld Nugget by Minitab. Eur Mech Sci 5:71–79. https://doi.org/10.26701/ems.837829

147. Maculotti G, Genta G, Galetto M (2024) Optimisation of laser welding of deep drawing steel for automotive applications by Machine Learning: A comparison of different techniques. Qual Reliab Eng Int 40:202–219. https://doi.org/10.1002/qre.3377

148. Aktepe A, Ersöz S, Lüy M (2014) Welding process optimization with artificial neural network applications. Neural Netw World 24:655–670. https://doi.org/10.14311/NNW.2014.24.037

149. Meng Y, Rajagopal M, Kuntumalla G, et al (2020) Multi-objective optimization of peel and shear strengths in ultrasonic metal welding using machine learning-based response surface methodology. Math Biosci Eng 17:7411–7427. https://doi.org/10.3934/mbe.2020379

150. Yurioka N, Suzuki H, Ohshita S, Saito S (1983) (!® Determination of Necessary Preheating Temperature in Steel Welding Findings include a new carbon equivalent to assess the susceptibility of steel to cold cracking more satisfactorily

151. (2024) Test Methods for Tension Testing of Metallic Materials

152. AWS D8.9M-2012

153. Method ST (2002) ASTM, E384-99. Standard Test Method for Microindentation Hardness of Materials. Identity 14:1–24

154. Mezher MT, Carou D, Pereira A (2024) Exploring Resistance Spot Welding for Grade 2 Titanium Alloy: Experimental Investigation and Artificial Neural Network Modeling. Metals (Basel) 14:. https://doi.org/10.3390/met14030308

155. Srivastava V, Basu B, Prabhu N (2024) Application of Machine Learning (ML)-based multi-classifications to identify corrosion fatigue cracking phenomena in Naval steel weldments. Mater Today Commun 39:. https://doi.org/10.1016/j.mtcomm.2024.108591

156. Hayazi NF, Jaraman P, Che Halin DS, et al (2025) Analysis of Process Parameters for Resistance Spot Welding on Galvanized Steel using Taguchi Method. Arch Metall Mater 70:39–46. https://doi.org/10.24425/amm.2025.152504

157. Pouranvari M, Marashi SPH (2011) Critical sheet thickness for weld nugget growth during resistance spot welding of three-steel sheets. Sci Technol Weld Join 16:162–165. https://doi.org/10.1179/1362171810Y.0000000016

158. Rezaei Ashtiani HR, Zarandooz R (2015) The Influence of Welding Parameters on the Nugget Formation of Resistance Spot Welding of Inconel 625 Sheets. Metall Mater Trans A Phys Metall Mater Sci 46:4095–4105. https://doi.org/10.1007/s11661-015-3030-1

159. Akkas N, Ferik E, Ilhan E, Aslanlar S (2016) The effect of welding current on nugget sizes in resistance spot welding of SPA-C steel sheets used in railway vehicles. In: Acta Physica Polonica A. Polish Academy of Sciences, pp 142–144

160. Betiku OT, Shojaee M, Sherepenko O, et al (2022) Optimizing post-weld performance of press-hardened steel resistance spot welds by controlling fusion zone porosity. Weld World 66:1733–1746. https://doi.org/10.1007/s40194-022-01332-2

161. Pouranvari M, Marashi SPH (2012) Weld nugget formation and mechanical properties of three-sheet resistance spot welded low carbon steel. Can Metall Q 51:105–109. https://doi.org/10.1179/1879139511Y.0000000028

162. (2024) International Ogranization of Standards 14373:2024 Resistance welding — Procedure for spot welding of uncoated and coated low-carbon steels. 2024:

163. Shojaee M, Tolton C, Midawi ARH, et al (2022) Influence of loading orientation on mechanical properties of spot welds. Int J Mech Sci 224:. https://doi.org/10.1016/j.ijmecsci.2022.107327

164. Chen S, Sun T, Jiang X, et al (2016) Online monitoring and evaluation of the weld quality of resistance spot welded titanium alloy. J Manuf Process 23:183–191. https://doi.org/10.1016/j.jmapro.2016.06.003

165. Zhou L, Zhang T, Zhang Z, et al (2022) Monitoring of resistance spot welding expulsion based on machine learning. Sci Technol Weld Join 27:292–300.

https://doi.org/10.1080/13621718.2022.2051408

166. Taufiqurrahman I, Ahmad A, Mustapha M, et al (2021) The effect of welding current and electrode force on the heat input, weld diameter, and physical and mechanical properties of SS316l/Ti6Al4V dissimilar resistance spot welding with aluminum interlayer. Materials (Basel) 14:1–20. https://doi.org/10.3390/ma14051129

167. Midawi ARH, Sherepenko O, Ramachandran DC, et al (2023) Prediction of Mechanical Properties in the Sub-Critical Heat Affected Zone of AHSS Spot Welds Using Gleeble Thermal Simulator and Hollomon-Jaffe Model. Metals (Basel) 13:. https://doi.org/10.3390/met13111822

168. Bogaerts L, Dejans A, Faes MGR, Moens D (2023) A machine learning approach for efficient and robust resistance spot welding monitoring. Weld World 67:1923–1935. https://doi.org/10.1007/s40194-023-01519-1

169. Zhao D, Vdonin N, Slobodyan M, et al (2024) Dynamic resistance signal–based wear monitoring of resistance spot welding electrodes. Int J Adv Manuf Technol 133:3267–3281. https://doi.org/10.1007/s00170-024-13993-y